Passive Enhancement of Air Flow at Pedestrian Level in Built Environments

by

Lup Wai Chew

B. Eng. Mechanical Engineering
National University of Singapore, Singapore, 2011

SUBMITTED TO THE DEPARTMENT OF MECHANICAL ENGINEERING IN PARTIAL
FULFILLMENT OF THE REQUIREMENTS FOR THE DEGREE OF

MASTER OF SCIENCE IN MECHANICAL ENGINEERING
AT THE
MASSACHUSETTS INSTITUTE OF TECHNOLOGY

JUNE 2017

Signature redacted

Signature of Author: _____
Department of Mechanical Engineering
May 10, 2017

Signature redacted

Certified by: _____
Leslie K. Norford
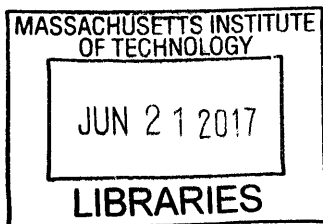Professor of Building Technology
Thesis Supervisor

Signature redacted

Certified by: ___
John G. Brisson
Associate Department Head for Education
Thesis Reader in Mechanical Engineering Department

Signature redacted

Accepted by: _____
Rohan C. Abeyaratne
Professor of Mechanical Engineering
Chairman, Committee for Graduate Theses

1

Passive Enhancement of Air Flow at Pedestrian Level in Built Environments

by

Lup Wai Chew

Submitted to the Department of Mechanical Engineering on May 10, 2017
in Partial Fulfillment of the Requirements for the Degree of
Master of Science in Mechanical Engineering

ABSTRACT

A densely built environment has low wind speed at the pedestrian level due to flow obstruction induced by buildings. Urban street canyons, the outdoor spaces formed between buildings, often have much lower wind speed than the atmospheric wind above the roof level. In tropical regions, wind plays an important role to improve outdoor thermal comfort of urban inhabitants by increasing the convective heat transfer from body surfaces. This thesis explores four types of passive architectural interventions to boost pedestrian-level wind speed in urban street canyons, namely void decks (open ground level), the wind catcher, the reversed wind catcher, and step-up/step-down canyons.

The proposed interventions were first studied experimentally in a recirculating water channel, where an atmospheric flow across an array of two-dimensional canyons was simulated with reduced-scale models of buildings. The velocity profiles in the third to sixth canyons were measured with Acoustic Doppler Velocimetry. Compared with the reference case, void decks enhance near-ground flows in all measured canyons by up to a factor of two, but the enhancement effect weakens in downstream canyons. The wind catcher enhances the flow in the target canyon by 2.5 times with no significant effect in other canyons. The reversed wind catcher and the step-up/step-down canyons reduce flows in the downstream canyons. The experimental data was used to validate computational fluid dynamics (CFD) models. CFD simulation results agree well with the experimental results for all cases. The validated CFD models were then used to study the void decks and the wind catcher in three-dimensional canyons. Void decks double near-ground flows in all canyons. The wind catcher increases near-ground flow in the target canyon by only 50% due to leakage at the sides. An improved wind catcher with sidewalls (to prevent leakage) triples near-ground flow in the target canyon. These findings prove the potential of void decks and the wind catchers as effective architectural interventions to enhance pedestrian-level wind speed and serve as a benchmark for future work to optimize the design of void decks and wind catchers.

Thesis Supervisor: Leslie K. Norford
Title: Professor of Building Technology, Department of Architecture

Reader in Mechanical Engineering Department: John G. Brisson
Title: Associate Department Head for Education

3

Acknowledgments

I would like to thank my advisor, Professor Leslie Norford, for his mentorship and guidance throughout these two years. When I started my journey at MIT, the research realm of built environments was relatively new to me, so I needed more time to review the literature. Furthermore, since I worked in the industry for a few years before coming to MIT, coursework became a heavy burden for me, as I had to put in extra efforts to review undergraduate materials. Professor Norford remained kind and patient and was always there to advise. With his generous guidance and support, I coped well, and even spent a productive summer in Singapore to conduct experiments, which contributed to a major part of this thesis. I look forward to continuing my work with him for my PhD.

I would also like to thank Professor John Brisson for being my thesis reader. His feedback and comments greatly helped me to improve this thesis. I am thankful to my colleagues, who have helped me along my journey here in the Building Technology Lab. Special thanks to Professor Leon Glicksman and Professor John Ochsendorf for their advice, from technical aspects such as pitfalls to watch out for in modelling, to non-technical aspects such as how to cope with stress. I am indebted to Professor Pierre Lermusiaux and Professor Amir A. Aliabadi for their guidance on computational fluid dynamics modelling. I also want to acknowledge the assistance from Kathleen Ross and Leslie Regan, who have made my research here enjoyable.

Thanks to my parents and my siblings for their unconditional love and support. They are my source of motivation. I would also like to thank my friends who have supported me and are always ready to lend me their helping hands.

Table of Contents

Chapter 1 Introduction

1.1 Introduction to Urban Street Canyons

The beginning of meteorological data collection in the 1850s allows for access global temperature trends over the past 150 years. While the topic of whether human activities have caused global warming remains hotly debated, it is undeniable that temperatures in urban areas have increased over the past centuries. For example, the mean annual temperature in Tokyo increased from 14 °C in the 1880s to 17 °C in the 2000s. Tropical regions suffer the same magnitude of temperature rise, as the mean temperature in cities such as Bangkok and Manila has increased by 2 °C to 29 °C between 1950 and 2000 (Kataoka et al., 2009). Recently, concentration of carbon dioxide, a greenhouse gas, has surpassed the 400 parts per million milestone ("NASA scientists react to 400 ppm carbon milestone," 2013) and continues to rise, despite the fact that 350 parts per million carbon dioxide is regarded as the critical limit for sustainability (Rockström et al., 2009). An urban area is usually warmer than its surrounding rural area, which is termed the "urban heat island" effect, analogous to a warm island (urban area) amid an area of a cooler sea (rural area). Higher levels of anthropogenic heat generation and reduced evapotranspiration heat transfer due to lack of vegetation are some factors contributing to higher temperatures in urban areas. High temperatures not only reduce thermal comfort and induce heat waves, but also can be fatal and cause severe economic impacts (Lau & Kim, 2012). Furthermore, more people are migrating to cities, so there is an immediate need to mitigate temperature rise especially in urban areas.

Although an urban area, or a built environment, is complex with different types and geometries of buildings, we can often simplify a specific area of study (Li et al., 2006; Stewart & Oke, 2012). For example, the space formed between two buildings is called an "urban street canyon." For brevity, the word "canyon" refers to an urban street canyon. A canyon is usually bounded by the ground and open at the roof level. The aspect ratio of a canyon is defined as H/W, where H is the canyon height and W the canyon width, as shown in Fig. 1.1(a). Another important parameter is the span-wise aspect ratio, defined as H/L, where L is the span-wise length of the canyon. When H/W is much larger than H/L, a two-dimensional (2D) canyon is formed, such as the one shown in Fig. 1.1(b). With incoming wind normal to the canyon (e.g., wind from left to right in Fig. 1.1(b)), a 2D flow is expected in a 2D canyon since the span-wise flow is negligible

the stream-wise and vertical flows. An array of canyons, with similar or different aspect ratios (Fig. 1.1), is often studied in a same domain, since the upstream buildings and canyons can affect the flow in downstream canyons.
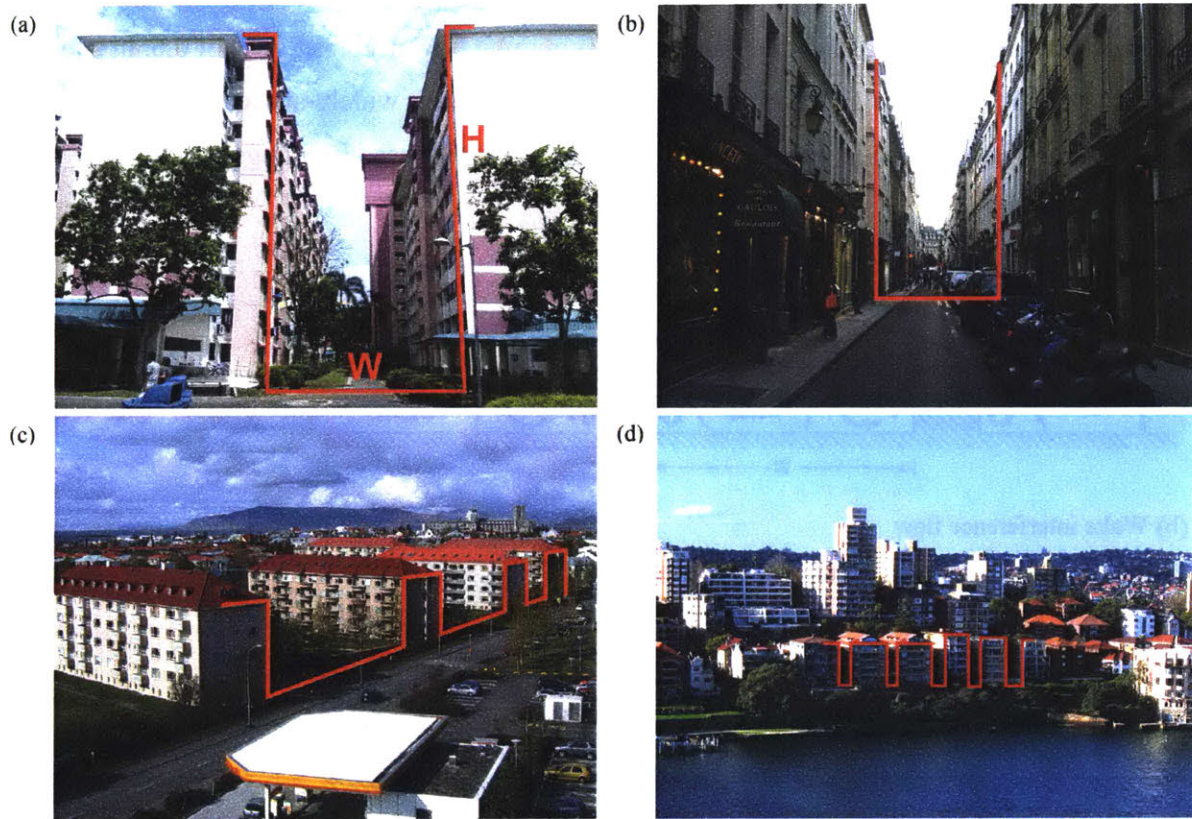

Fig. 1.1. Urban street canyons with height H and width W demarcated by the red lines. (a) A canyon between two flats with aspect ratio 1.8, (b) a canyon between two rows of shop houses with aspect ratio 2, (c) canyons between flats with varying aspect ratios between 0.6 and 2, (d) canyons between apartments with aspect ratio about 3.5.

A canyon possesses its unique microclimate due to various factors such as shielding effects from atmospheric wind and solar irradiance. With the upstream building(s) obstructing incoming wind, the flow in the canyon is induced by the freestream wind above the roof level. Oke (1987) pioneered the categorization of wind flow patterns across canyons into three regimes: isolated roughness flow, wake interference flow, and skimming flow. When two buildings are far apart, a wide canyon with a small aspect ratio, H/W, is formed. For H/W < 0.3, the isolated roughness flow regime is observed, since the flow fields of the upwind and downwind buildings are isolated (Fig. 1.2(a)). For H/W between 0.3 and 0.7, the wake of the upwind building starts to interact with the downwind building (Fig. 1.2(b)). When H/W is increased beyond 0.7, the skimming flow pattern

is observed, with one or multiple circulation vortices formed in the canyon (Fig. 1.2(c)). The H/W for the transition from one regime to another regime is not clearly defined. For example, while Oke (1987) defines such transitions to occur at H/W around 0.3 and 0.65, Sini, Anquetin, & Mestayer (1996) find that the transition from isolated roughness flow to wake interference flow occurs at H/W of about 0.12, and the transition to skimming flow occurs at H/W of 0.6. In general, isolated roughness flow is observed in wide canyons (between widely-spaced buildings) while skimming flow is observed in deep canyons (between closely-spaced buildings).

(a) Isolated roughness flow

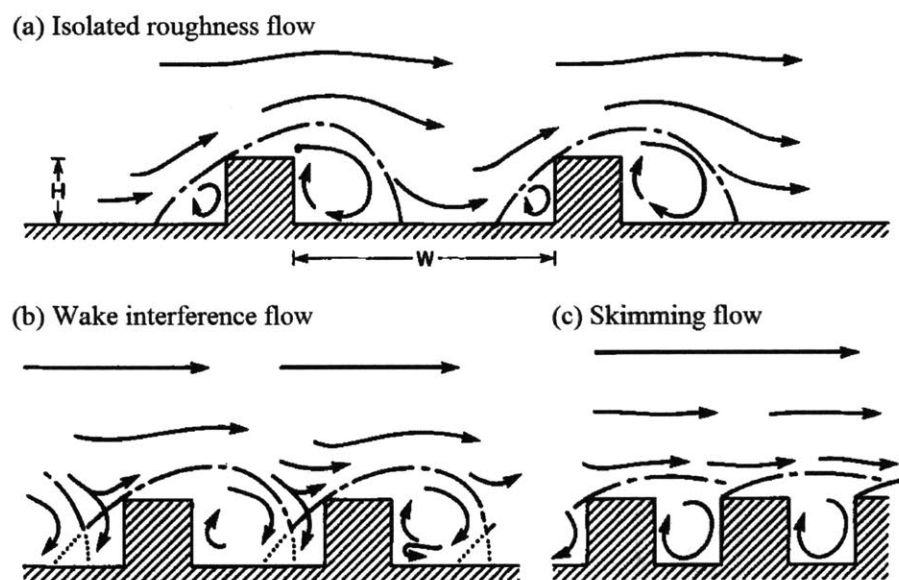(b) Wake interference flow   (c) Skimming flow

Fig. 1.2. Three categories of flow regimes at different canyon aspect ratios. Image from Oke (1987).

Due to high density of buildings in urban areas, most canyons exhibit the skimming flow regime. Therefore, skimming flow is the most studied flow regime in the realm of the built environment (Li et al., 2006). The applications of such studies include pollutant dispersion and pedestrian-level wind field prediction, which are important for urban planning. Due to the blockage effects of buildings, wind speed in a canyon is much lower than the atmospheric wind speed above the roof level. The most severe case of wind speed reduction is expected in 2D canyons with a normal wind direction. Hence, most studies of skimming flow focus on wind flowing normally across 2D canyons. For 2D canyons with H/W = 1, both experimental and numerical studies have confirmed the formation of a large circulation vortex, depicted in Fig. 1.3. Brown et al. (2000) and Meroney et al. (1996) conducted experiments with scaled-down canyons of H/W = 1 in wind tunnels. Both papers report a large circulation vortex in each canyon when the flow has reached a

pseudo-steady state. Baik et al. (2000) and Li et al. (2008) observe a similar flow pattern with a single vortex in water channel experiments. Computational fluid dynamics simulations of canyons with H/W = 1 predict the same flow patterns. In general, Reynolds-averaged Navier-Stokes (RANS) turbulence models produce satisfactory results although such models often assume a steady incoming wind (Baik & Kim, 1999, Jeong & Andrews, 2002, Li, Liu, & Leung, 2005). On the other hand, large eddy simulation (LES) models are more accurate but are much more computationally expensive to run (Salim et al., 2011, Tominaga & Stathopoulos, 2011).
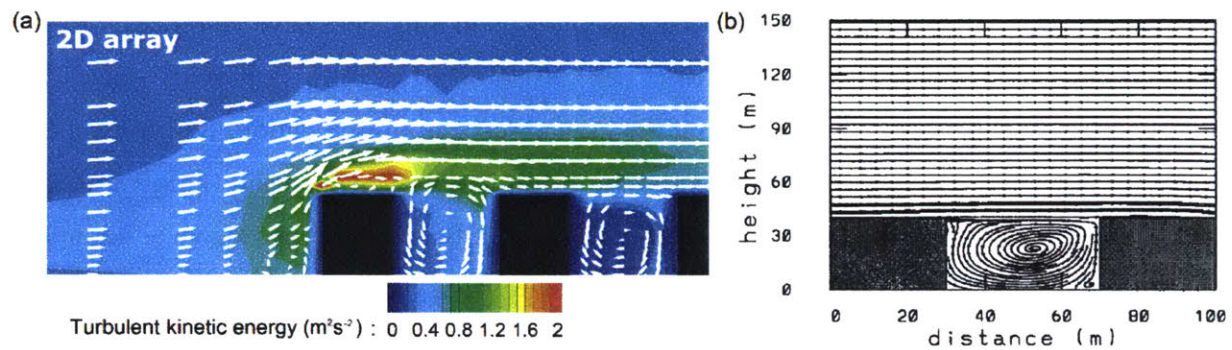

Fig. 1.3. Single vortex observed in canyons with H/W = 1. (a) Mean velocity vectors superimposed on turbulent kinetic energy contour plots measured in a wind tunnel (Brown et al., 2001), (b) Streamline fields from computational fluid dynamics simulation (Baik & Kim, 1999).

1.2 Proposed Architectural Interventions to Enhance Pedestrian-level Wind Speed

Although cities in tropical regions suffer the most with global temperature rise, there is far fewer thermal comfort research conducted in tropical climates than subtropical and moderate climates (Yang, Wong, & Jusuf, 2013). Therefore, we focus on improving the thermal comfort of urban areas in tropical regions. There are six major factors contributing to thermal comfort: air temperature, radiant temperature, wind speed, humidity, metabolic rate, and clothing insulation (de Dear & Spagnolo, 2005; Djongyang, Tchinda, & Njomo, 2010). In tropical regions, air temperature and humidity are relatively constant, and they require high energy input to alter even in an indoor environment (e.g., by using air conditioning), so it is not feasible to reduce outdoor air temperature and humidity. Metabolic rate and clothing insulation are individual-specific so they are not within our consideration of outdoor thermal comfort improvement. Between wind speed and mean radiant temperature, we will study the former in detail, specifically wind speeds at the pedestrian level (i.e. near-ground level). Since thermal discomfort due to low temperatures rarely

9

occurs, higher wind speeds are preferable in tropical regions (de Dear & Kim, 2016; Roth & Chow, 2012). Passive architectural interventions, such as optimizing roof design (Huang, Hu, & Zeng, 2009; Kastner-Klein, Berkowicz, & Britter, 2004) and increasing porosity of buildings (Yuan, Ng, & Norford, 2014), are preferable since they require no energy input. We introduce four types of passive architectural interventions: void decks, the wind catcher, the "reversed wind catcher," and step-up/step-down canyons.

"Void deck" is a term commonly used in Singapore to refer to the open space at the ground floor of a building, as shown in Fig. 1.4. Many public flats in Singapore have void decks, which serve as public spaces for social activities (Yuen, 2011). Void decks also provide spaces for cultural events such as weddings and funeral wakes, and serve as polling stations during elections (Cairns et al., 2014). By intuition, the openings at the ground level allow wind to flow through, thereby increasing pedestrian-level wind speed. Newly built flats in Singapore have either much smaller or no void decks (Koh, 2015). Social aspect aside, we attempt to quantify the near-ground wind speed enhancement of void decks to justify the need of such openings for outdoor thermal comfort improvement.

Fig. 1.4. Void decks, open spaces at the ground floors of public flats in Singapore.

Besides void decks, another plausible method to enhance pedestrian-level wind speed is by installing wind catchers above the roof level to channel atmospheric wind into the canyons. The inlets of wind catchers are above the roof level to capture stronger wind unobstructed by upstream buildings. Fig. 1.5 shows a scaled-down model of a wind catcher being tested in a wind tunnel. Wind catchers in a favorable orientation (facing the incoming wind direction) are effective to channel flows from the atmosphere into enclosed indoor areas (Esfeh et al., 2012; Montazeri & Azizian, 2008). Wind catchers are less effective to channel wind into open spaces and are seldom used in outdoor environments (Saadatian et al., 2012). Nevertheless, we believe that a wind catcher has the potential to enhance pedestrian-level wind speed in a canyon, as a canyon is not fully open (sometimes, an outdoor space with surrounding buildings is considered a "semi-outdoor" space (Hwang & Lin, 2007; Spagnolo & de Dear, 2003)). Fig. 1.6 is an example of an outdoor wind catcher at the Masdar Institute of Science and Technology, Abu Dhabi, United Arab Emirates. Since an urban area has high building density with little space to erect a wind tower, we propose a simplified structure that can be installed above existing buildings. We explore the potential of a wind catcher with its inlet facing the incoming wind. In a reversed wind direction (i.e. the inlet is facing the downwind direction), the wind catcher become a "reversed wind catcher", which may lose its function to channel atmospheric wind into a canyon. Hence, we also study the reversed wind catcher to quantify its effect on flow enhancement.
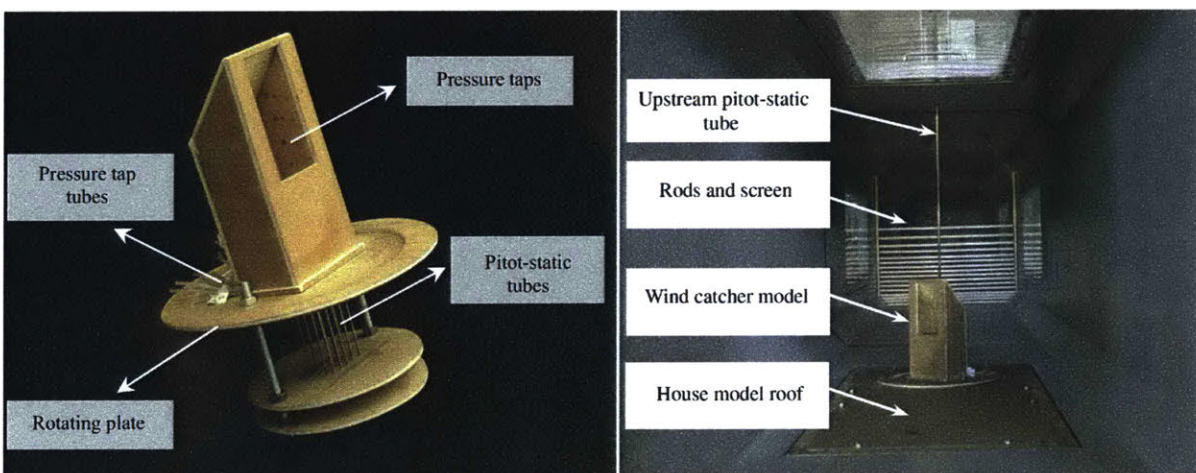

Fig. 1.5. A scaled-down model of a wind catcher on a rotatable plate being tested in a wind tunnel. Images from Montazeri & Azizian (2008).
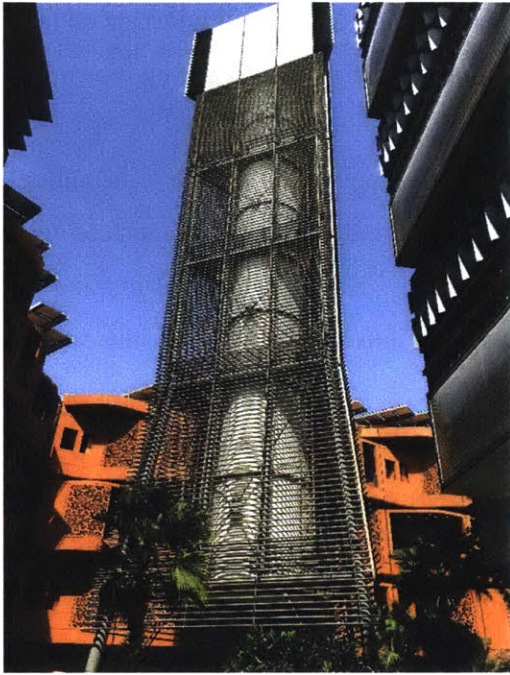
Fig. 1.6. A wind tower to direct atmospheric wind to the pedestrian level (photo courtesy of Amir A. Aliabadi).

Step-up and step-down canyons are formed in an array of buildings with different heights. A step-up canyon is formed between a shorter upwind building and a taller downwind building, while a step-down canyon is formed between a taller upwind building and a shorter downwind building. Step-up/step-down canyons can exhibit very different wind flow patterns than canyons with a regular height (Assimakopoulos, ApSimon, & Moussiopoulos, 2003; Hang, Li, & Sandberg, 2011; Xiaomin, Zhen, & Jiasong, 2006). We will study the pedestrian-level wind speed in a step-up canyon and a step-down canyon formed by having a tall building amid an array of shorter buildings.

There are three major approaches to study wind flow in a built environment: field measurements, reduced-scale experiments, and numerical simulations (Memon, Leung, & Liu, 2008; Mirzaei & Haghighat, 2010). Field measurements are often costly and time consuming. For instance, field data collection spanned 18 months in the urban street canyon studied by Rotach (1995). We thus adopted the reduced-scale experimental and numerical simulation approaches for our study. The experimental study is outlined in Chapter 2, followed by numerical simulation study in Chapter 3. We then extend the numerical study to three-dimensional canyons in Chapter 4. The thesis is concluded in Chapter 5 with recommendations of future work.

Chapter 2 Reduced-scale Experiments

This chapter discusses the experimental studies with reduced-scale models. Section 2.1 outlines the experimental setup. Sections 2.2, 2.3, 2.4, 2.5, and 2.6 discuss the results of the reference case with canyons of aspect ratio 1, canyons with void decks, canyons with a wind catcher, canyons with a reversed wind catcher, and step-up and step-down canyons, respectively. The result comparison is summarized in section 2.7

2.1 Experimental Setup.

A recirculating water channel in the Hydraulic Engineering Laboratory at the Department of Civil and Environmental Engineering, National University of Singapore, was used for all experiments. The water channel is 15 m long, 0.6 m tall and 0.6 m wide. Fig. 2.1 shows a sketch of the side view of the water channel. Flow straighteners made with a combination of plastic tubes, wire mesh and honeycombs were arranged at the inlet to minimize span-wise and vertical velocities. Two layers of ceramic marbles (0.5 inch or 1.27 cm diameter) accelerate the flow development, so the flow profile at the test section is fully developed. Fig. 2.2 shows the dimensions of the ceramic marbles and honeycombs. The test section is at the middle length of the channel. An adjustable floodgate (Fig. 2.3) at the end of the water channel controls the water level. The water is circulated back to the tank with a pump. The flow rate was controlled by turning the valve, up to a maximum flow rate of 50 l/s. A digital flowmeter was used to measure the flow rate.
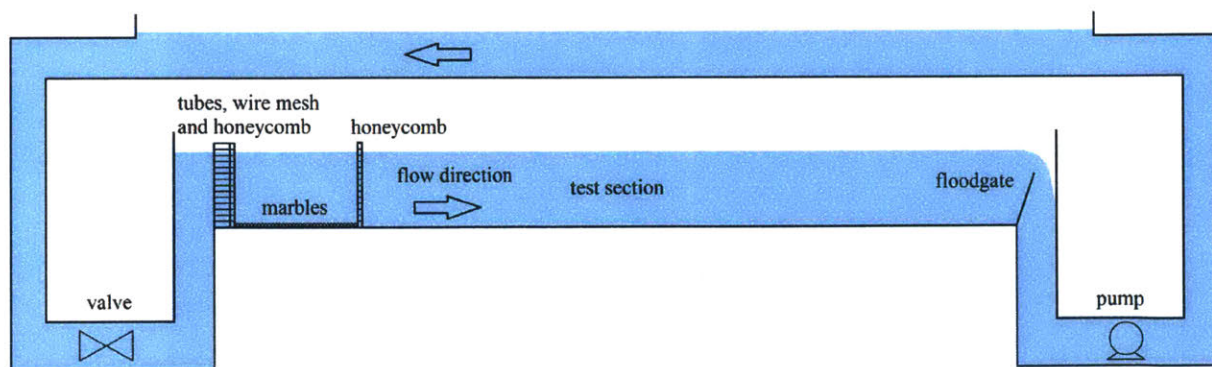
Fig. 2.1. Experimental setup of the recirculating water channel.

The water channel has a maximum flow rate of 50 l/s, corresponds to a maximum velocity of 0.2 m/s at the test section. High velocity flows were needed in some of the experiments, thus

vertical converging-flat-diverging partitions were installed to reduce the effective width from 0.6 m to 0.3 m, as shown in Fig. 2.4. The sloped parts are 1.2 m long, while the flat part is 3.6 m long. These partitions double the stream-wise velocity at the test section (the flat part) under the same flow rate. They are made of 12 mm thick marine plywood waterproofed with epoxy coating. The sides of the partitions are supported by the same type of marine plywood. The gaps between the channel walls and the partitions were filled with water to balance the hydrostatic pressure in the test section during experiments.
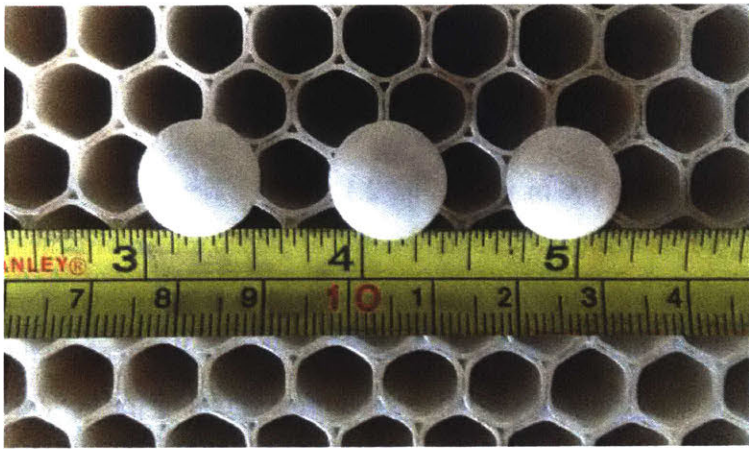

Fig. 2.2. The dimensions of ceramic marbles and honeycomb (top scale in inch, bottom scale in cm).

Fig. 2.3. Adjustable floodgate to vary water depth. Left: viewed from upstream of the floodgate (no water), right: viewed from the end of the channel with water flowing.
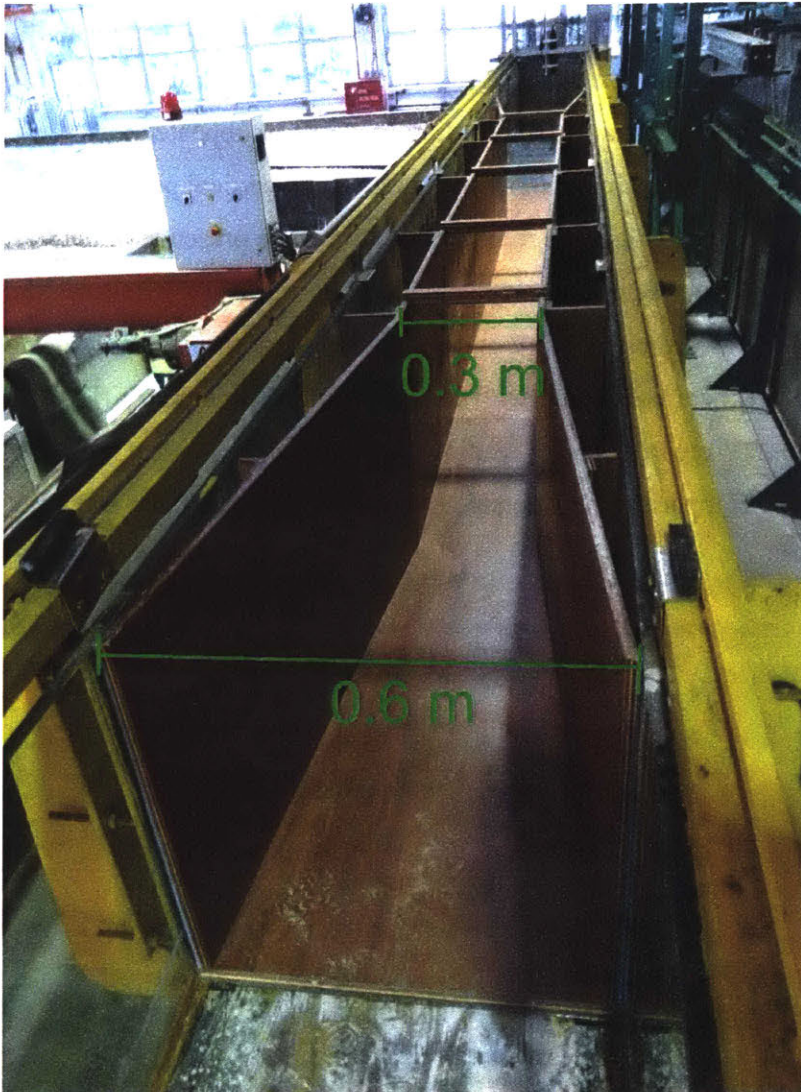
Fig. 2.4. The converging-flat-diverging partitions reduce the effective width of the water channel from 0.6 m to 0.3 m at the test section.

Acoustic Doppler Velocimeters (Vectrino by Nortek AS), or ADV in short, were used throughout the experiments to measure the flow velocity. Fig. 2.5 shows an ADV with four receivers and an operating ADV submerged in water. The ADV measures all three components (stream-wise, vertical and span-wise) of velocity and velocity fluctuations up to 200 Hz. The accuracy is ±0.5 % of the measured value ± 1 mm/s. ADV works by sending an acoustic pulse from the transmitter at the tip. The receivers then record both the direct pulse and the reflected pulse to calculate the Doppler shift. Flow seeding with suspended particulates is required for pulse reflection. Kaolin clay pre-mixed with water was used as seeding material and was introduced near

the floodgate (Fig. 2.6). The flow was then allowed to settle for 30 minutes until the water in the whole channel turned milky. The signal-to-noise ratio (SNR) must exceed 15 to ensure that the flow is sufficiently seeded. If the SNR was below 15, the seeding process was repeated to achieve an SNR above 15. The ADV was mounted on a metal frame with adjustable vertical positions. The diameter of the rod connecting the transmitter and the receivers is 7 mm. The presence of the rod, transmitter and receivers has minimum effect on the measurement, as the ADV measures the velocity 5 cm below the transmitter. Nevertheless, ADV is categorized as an intrusive measuring device. Compared to a similar experiment conducted with Laser Doppler Velocimetry (LDV, a non-intrusive measuring device), ADV records similar readings, thereby justifying that the ADV probes do not obstruct the flow. The comparison between measurements taken by ADV and LDV is discussed in Section 2.2
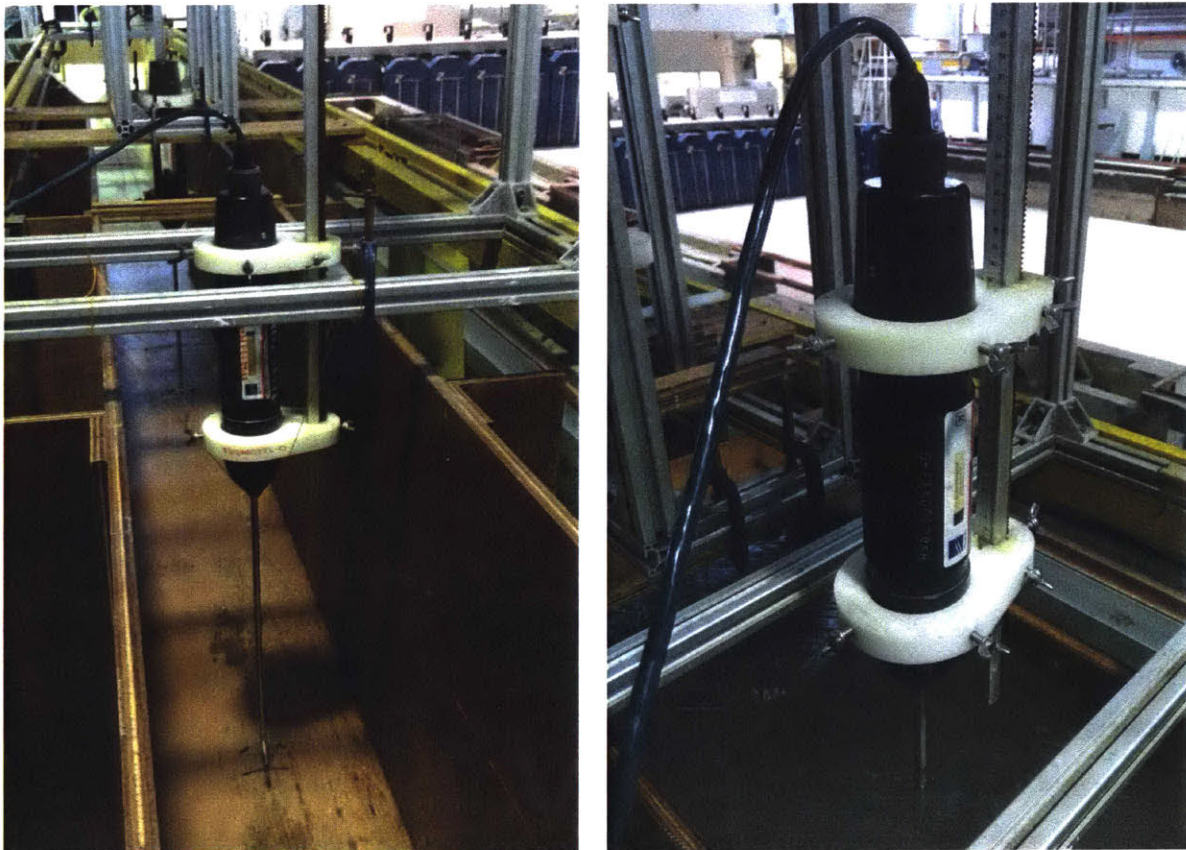

Fig. 2.5. Acoustic Doppler Velocimeters (ADV) for velocity measurements. Left: an ADV mounted on a metal frame, right: an operating ADV submerged in flowing water.
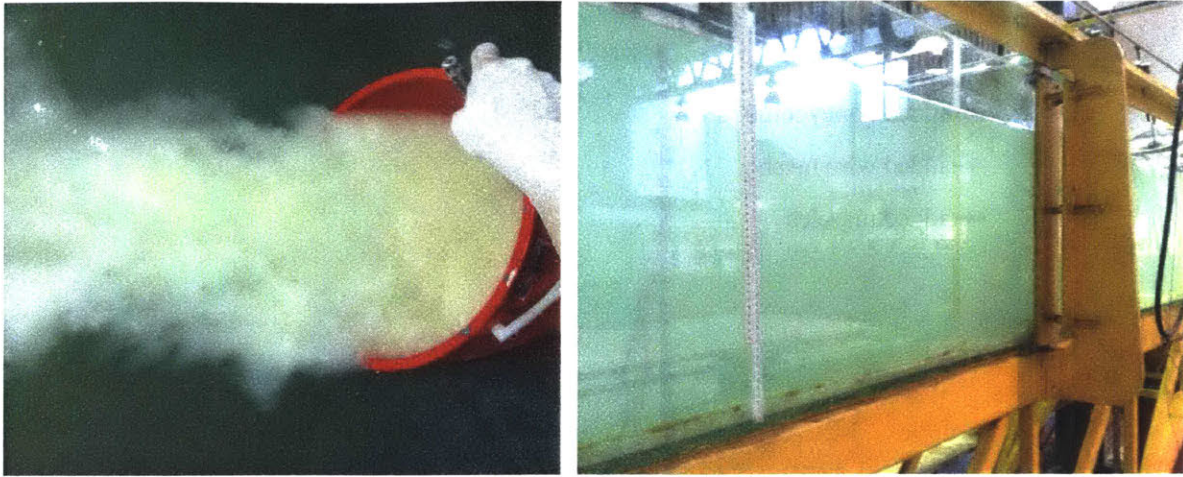
Fig. 2.6. Left: Flow seeding with kaolin clay, right: the water appeared milky after seeding.

Before conducting experiments with model blocks of buildings, the freestream profile was measured at the test section. The flow rate was 20 l/s, corresponded to a freestream velocity of about 0.2 m/s. Fig. 2.7 plots the normalized stream-wise velocity profile, u/Uref, against the vertical distance from the bottom, z. The stream-wise velocity is normalized by a reference velocity Uref, which is the freestream velocity in this case. Both the span-wise and vertical velocities are nearly zero (not shown) so the flow is one-dimensional. There is no apparent length scale in this flow so z is not normalized. The initial setup of the water channel comprised non-uniformly arranged plastic tubes and wire mesh at the channel inlet, which produced an undesirable flow profile. This profile does not resemble a boundary layer flow, as the velocity is higher at the bottom half of the channel (green line). This could be due to the non-uniform layout of wire mesh at the inlet. The flow profile was improved by adding two layers of honeycomb (orange line). Further improvement was achieved by adding more wire mesh and rearranging the wire mesh to have a uniform layout (blue line). The ceramic marbles accelerated flow development (black line), where a log-profile was realized near the bottom. This profile was adopted for all subsequent experiments. The layout of the flow straighteners and ceramic marbles is depicted in Fig. 2.8. At the inlet, plastic tubes, wire mesh and a layer of honeycomb were arranged to align with the flow direction. The flow develops over two layers of ceramic marbles until the end of the converging part of the partitions. The second layer of honeycomb eliminates remaining non-uniformity in the flow before the test section (the flat part of the partitions).
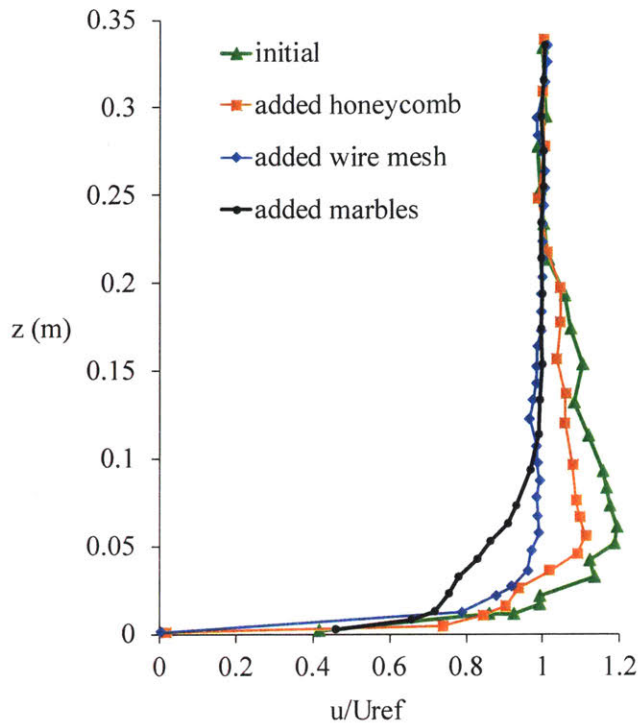
Fig. 2.7. Stream-wise velocity profiles measured at the middle of the test section versus the vertical distance. The best flow profile (black line) is achieved by adding honeycombs, wire mesh and marbles.
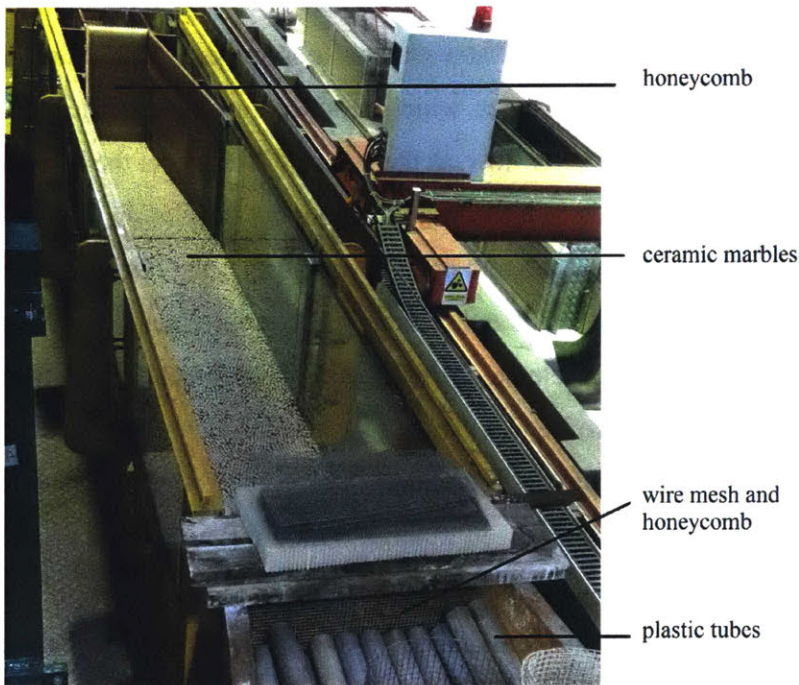

Fig. 2.8. The layout of plastic tubes, wire mesh and honeycombs in the water channel.

To ensure that the flow is fully developed at the test section, another set of data was collected at 1 m downstream of the test section for comparison. The tests were also repeated with different flow rates between 13 l/s and 50 l/s to confirm that the (normalized) profiles remained unchanged at different flow rates. Fig. 2.9 shows the profiles of normalized stream-wise velocity, u/Uref, at two locations: at the test section and 1 m downstream of the test section. All profiles at different flow rates collapse into a single curve. At 1 m downstream of the test section, the flow profiles (Fig. 2.9(b)) remain unchanged compared to the profiles at the test section (Fig. 2.9(a)), verifying that the flows are fully developed at the test section.
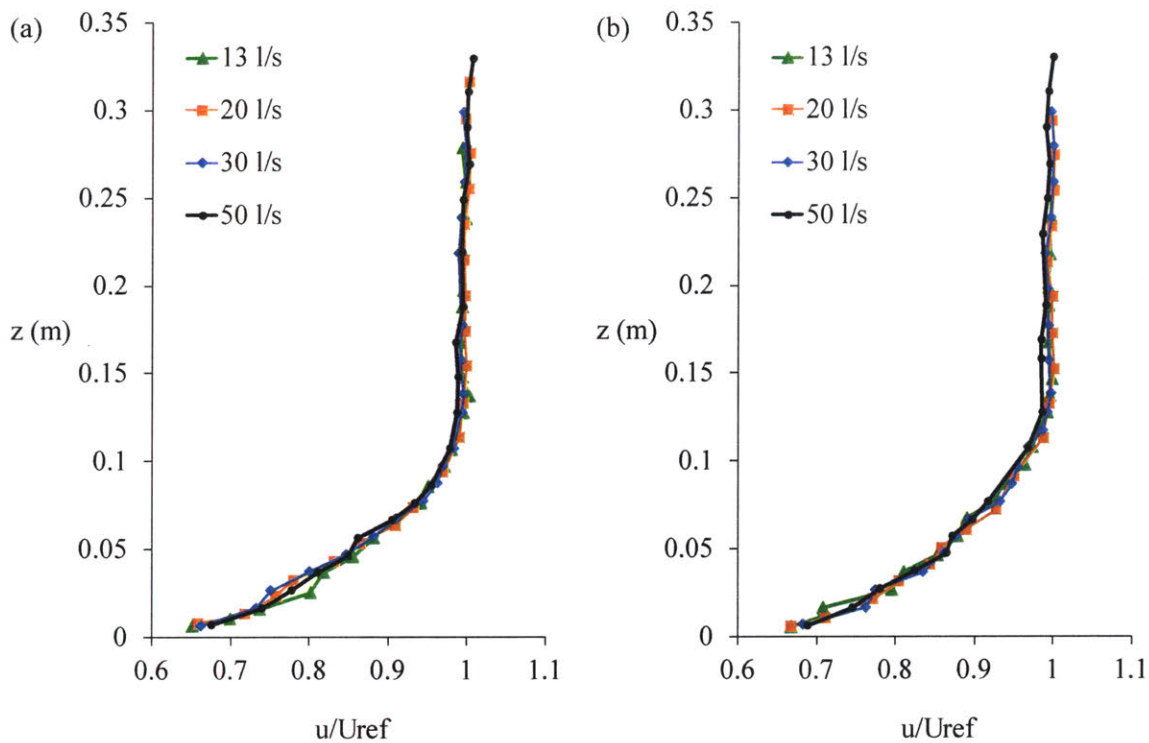
Fig. 2.9. Normalized stream-wise velocity profiles at different flow rates (liter per second). (a) Profiles at the test section, (b) profiles at 1 m downstream of the test section.

2.2 Reference Case with Canyons of Aspect Ratio 1

Fig. 2.10 shows the arrangement of eight model blocks forming seven urban street canyons, which aims to reproduce the water channel experiments in Li et al. (2008). This is important to test the capability of our experimental setup to reproduce results in the literature and to verify the quality of ADV measurements by comparing them with non-intrusive measurements. Eight pieces of

19

12 cm tall × 10 cm wide × 30 cm long wooden blocks were spaced 12 cm apart to simulate an array of 12 cm × 12 cm canyons, as shown in Fig. 2.11. This resembles an array of seven two-dimensional (2D) canyons with an aspect ratio of 1. The middle-line velocity profiles were measured in selected canyons. The flow patterns including the rotational direction of vortices and the velocity magnitudes near the roof level can then be deduced from the velocity profiles.
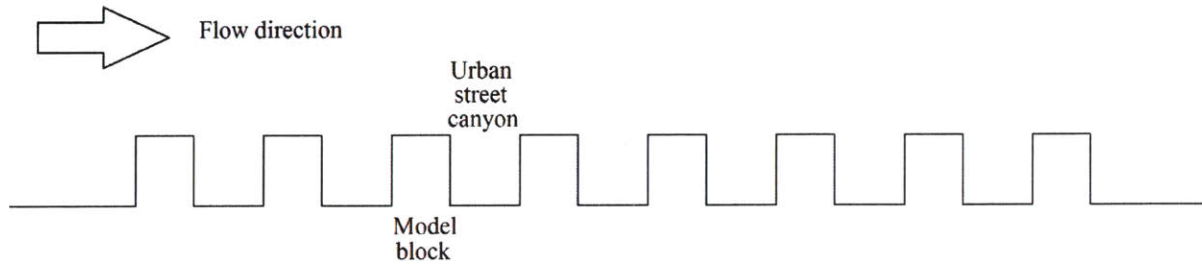

Fig. 2.10. Flow across an array of 2D canyons with aspect ratio 1.

Fig. 2.11. Arrangement of seven 12 cm tall × 12 cm wide canyons with aspect ratio 1 in the test section.
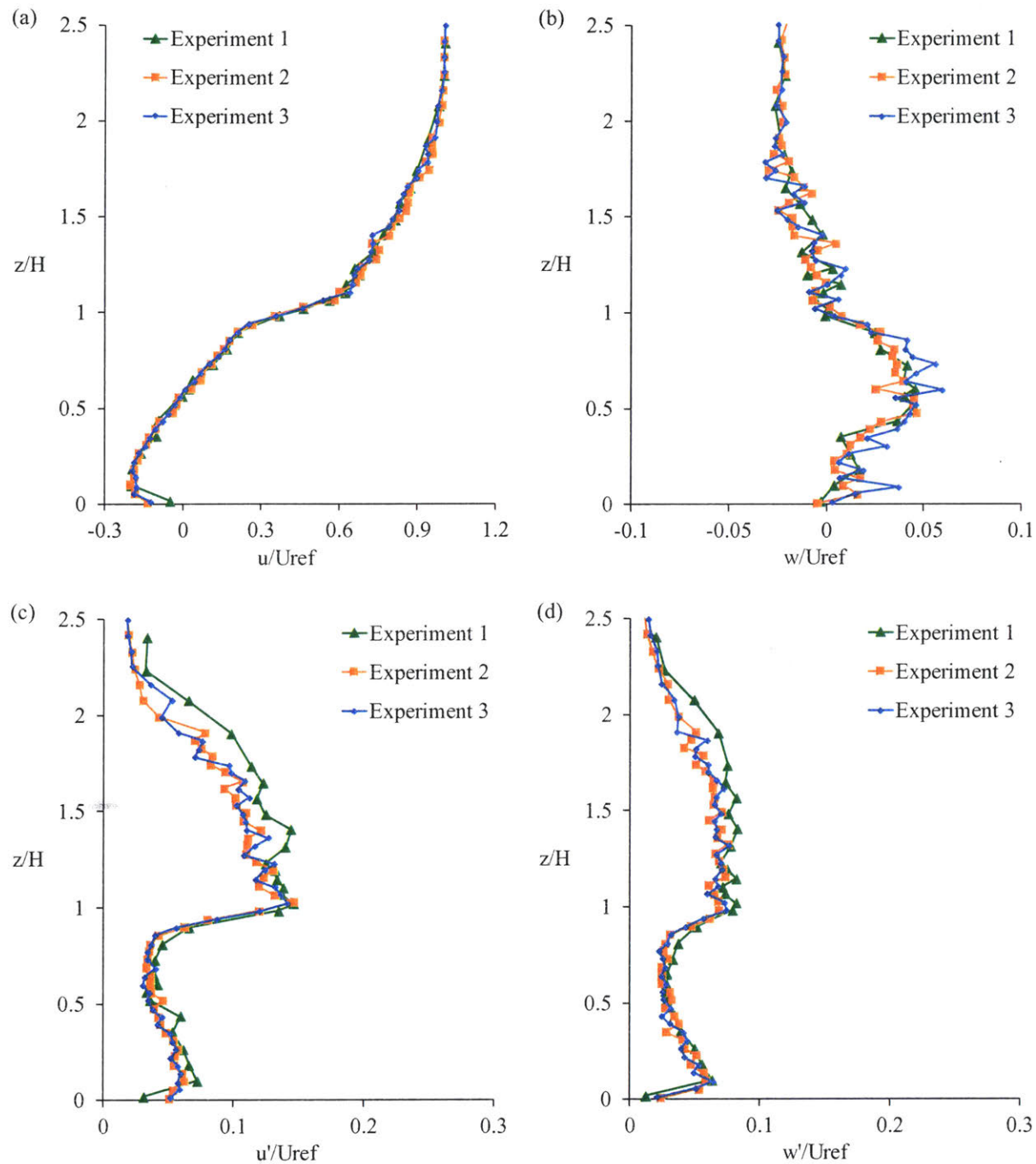
Fig. 2.12. Normalized middle-line velocity profiles at canyon 6 collected on three different days. (a) Mean stream-wise velocity, (b) mean vertical velocity, (c) stream-wise velocity fluctuation, and (d) vertical velocity fluctuation.

First, three sets of readings with a fixed inlet flow rate (12 l/s) were collected on three separate days to confirm the repeatability of the experiments. The valve was closed and the pump was turned off between each experiment, i.e. each experiment was a new start and reached a quasi-steady state before data collection. Fig. 2.12 shows the vertical (in the z-direction) profiles of the

21

normalized velocity components: mean stream-wise velocity, u/Uref; mean vertical velocity, w/Uref; stream-wise velocity fluctuation, u'/Uref (root-mean-squared); and vertical velocity fluctuation, w'/Uref (root-mean-squared). All velocity components are normalized by a reference velocity, Uref, which is the freestream velocity at z/H = 2.5. The vertical distance is normalized by the canyon height, H = 12 cm. Fig. 2.12(a) shows the near-coincidence of u/Uref profiles from all three experiments. The discrepancy of w/Uref appears large in Fig. 2.12(b), but this is due to very small w/Uref (smaller than 5%). Fig. 2.12(c) and Fig. 2.12(d) show that both u'/Uref and w'/Uref are very similar in the three experiments. Overall, Fig. 2.12 confirms that the three sets of measurements are consistent and the results are highly reproducible.
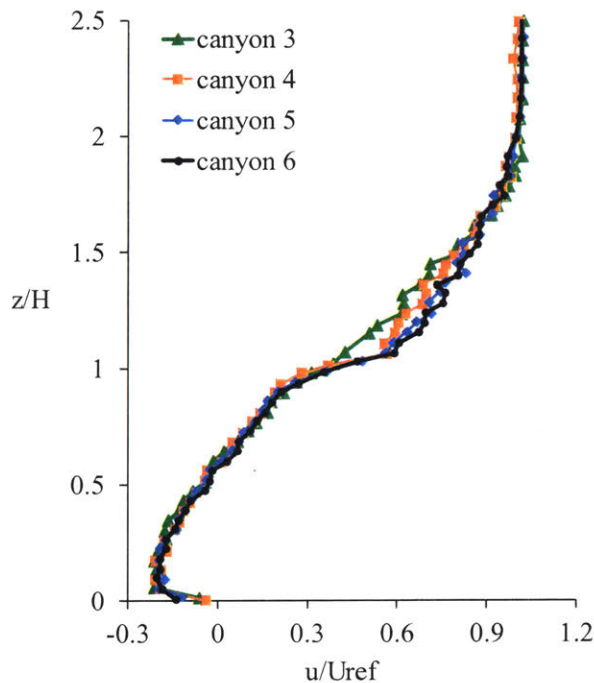
Fig. 2.13. Normalized stream-wise velocity profiles of canyons 3, 4, 5, and 6.

Second, we need to ensure that the flow in the target canyon (the fourth canyon, or canyon 4) has achieved the urban roughness flow regime. Flow across a single building is termed the "isolated flow," whereas flow across an array of buildings is termed the "urban roughness flow." In an array of buildings with no upstream obstacles, the first canyon exhibits the isolated flow, while the transition to urban roughness flow occurs at the third canyon (Brown et al., 2000; Meroney et al., 1996). The second canyon exhibits a flow pattern somewhat between the isolated flow regime and the urban roughness flow regime. We are interested in studying the urban

roughness flow (which is the flow regime in a dense built environment). To ensure that the target canyon 4 is in the urban roughness flow regime, the stream-wise velocity profile in canyon 4 is compared with the profiles at the upstream canyon 3 and the downstream canyons 5 and 6. Fig. 2.13 shows that canyons 3, 4, 5, and 6 have almost identical profiles, confirming that canyon 4 is within the urban roughness flow region. This is in agreement with Brown et al. (2000) and Meroney et al. (1996), who report that the transition to urban roughness flow regime occurs at the third canyon.

Third, to confirm that the ADV (an intrusive measuring device) does not disrupt the flow, Laser Doppler Velocimetry (LDV, a non-intrusive measuring device) measurements from the water channel experiments of Li et al. (2008) are used as a benchmark comparison. The Reynolds number, Re, is defined as Re = (Uref)H/v, where Uref is a reference velocity, H the canyon height and v the kinematic viscosity. In the literature, Uref is usually taken as the velocity at the roof level, as it is conveniently available. However, there is a major drawback: the variation of the velocity at the roof level is large due to a large velocity gradient at this elevation. On the other hand, the freestream velocity remains relatively constant. For example, the velocity 0.1H above the roof level (z/H = 1.1) differs by about 50% compared to the velocity at the roof level (z/H = 1.0) in Li et al. (2008). In contrast, the difference between the velocity at z/H = 2 and z/H = 3 is less than 2%. This trend is clearly seen in Fig. 2.13, where u/Uref increases from 0.3 to 1.0 between z/H = 1 and z/H = 2. Above z/H = 2, u/Uref remains almost constant at 1.0. In other words, the stream-wise velocity approaches the freestream velocity at about two times the canyon height, H. Kastner-Klein, Fedorovich, & Rotach (2001) and Li et al. (2008) propose taking the velocity at z/H = 2 or higher as the reference velocity, since it is less sensitive to the measurement position. We adopted their recommendation in this study by using the freestream velocity as Uref. Fig. 2.14 shows the normalized middle-line velocity profiles at canyon 4 with Re = 19000 and Re = 61800, with comparison to Re = 11000 in Li et al. (2008). The good agreement between this study (which used ADV) and Li et al. (2008) (which used LDV) verifies that the ADV in our experiments does not disturb the flow. Furthermore, the water channel in Li et al. (2008) does not have a partition, so this agreement also verifies that the converging-flat-diverging partitions in our experimental setup do not disturb the 2D nature of the flow.
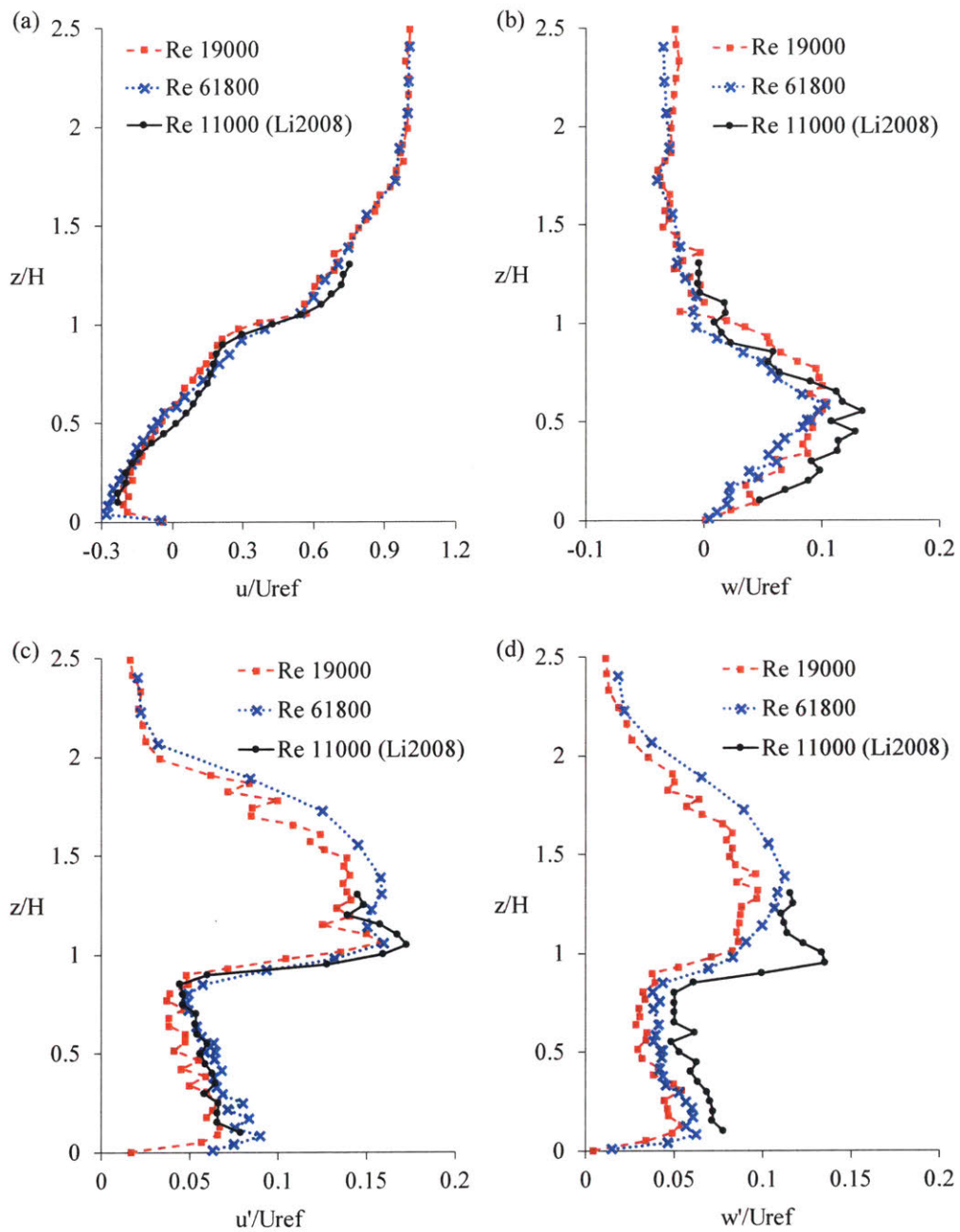
Fig. 2.14. Normalized middle-line velocity profiles at canyon 4 at different Reynolds numbers. (a) Mean stream-wise velocity, (b) mean vertical velocity, (c) stream-wise velocity fluctuation, and (d) vertical velocity fluctuation. Li2008 data is from the water channel experiments of Li et al. (2008).
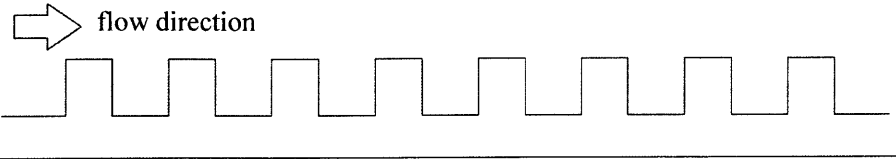
Re is very high in a real-scale built environment, on the order of 10^6 to 10^7. For example, a 20 m × 20 m real-scale canyon with a reference wind speed of 3 m/s has an Re = 3.8 × 10^6. It is usually not possible to achieve such a high Re with reduced-scale experiments, so Re similarity is often not satisfied in experiments. Instead, much lower Re (< 10^5) are adopted in wind tunnel and

water channel experiments. For instance, Re of 3400, 30000, and 59000 are reported in wind tunnel experiments by Meroney et al. (1996), Brown et al. (2000), and Kastner-Klein & Plate (1999), respectively. Water channel experiments by Baik et al. (2000) and Li et al. (2008) report Re of 10000 and 12000. Re = 10000 is widely accepted as the critical Re required to achieve Re independence (i.e. further increase in Re does not change the flow field patterns and the normalized average properties of the flow). This criterion justifies a lower Re at reduced-scale experiments, as long as Re independence is achieved. Referri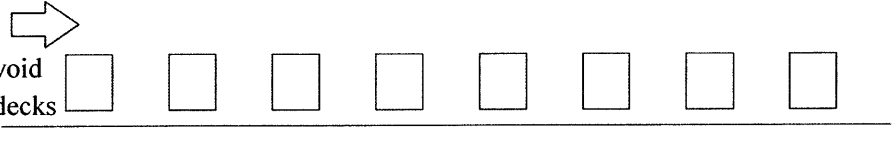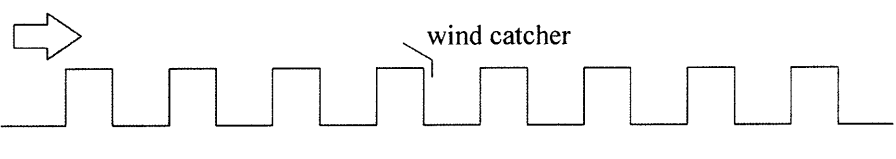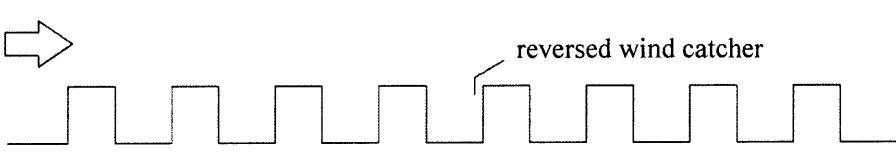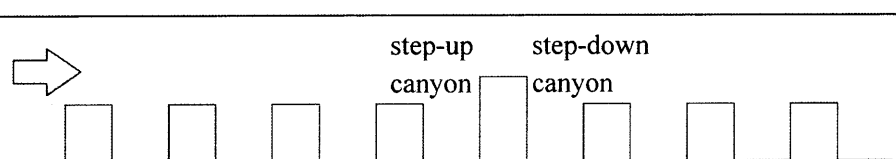ng to Fig. 2.14, the velocity profiles with Re ranging from 11000 to 61800 have a similar trend, suggesting that the flow pattern is indeed Re independent within this range of Re. Both our results and the results from Li et al. (2008) predict a single vortex in the canyon, since u/U_{ref} is negative near the ground and positive at the roof level, as shown in Fig. 2.14(a). Fig. 2.14(b) shows that w/U_{ref} up to 15% is observed inside the canyon ($z/H < 1$), but w/U_{ref} reduces to almost zero above the roof level ($z/H > 1$). Span-wise velocity, v/U_{ref} (not shown), is zero throughout, confirming the 2D nature of the flow. Fig. 2.14(c) and Fig. 2.14(d) show that both the normalized velocity fluctuations, u'/U_{ref} and w'/U_{ref}, are the highest between $z/H = 1$ and $z/H = 1.5$, and decay with increasing height above $z/H = 1.5$. This is expected, as turbulence is generated mostly at the roof level where the velocity gradient is the highest. In the canyon, both u'/U_{ref} and w'/U_{ref} are constant at about 5%, except near the ground, where they decay to zero.

We have shown that our experimental setup is able to reproduce the well-studied canyons of aspect ratio 1. Next, we introduce different types of architectural interventions to study their effects on flow velocities at the pedestrian level, or near-ground level. Table 2.1 summarizes the subsequent four sets of experiments conducted: (ii) canyons with void decks, (iii) canyons with a wind catcher, (iv) canyons with a wind catcher in a reversed flow direction (the "reversed wind catcher"), and (v) step-up and step-down canyons with a tall building amid an array of shorter buildings. All cases have seven canyons. Case (ii) has void decks below all model blocks, case (iii) has a wind catcher above canyon 4, case (iv) has a reversed wind catcher above canyon 4, and case (v) has a taller fifth building model. In all cases, the Reynolds numbers are above 10000 to ensure Reynolds number independence.

Table 2.1. Schematic of five cases studied experimentally in the water channel.

Case	Description	Experimental setup
i	Reference	flow direction
ii	Void Decks	void decks
iii	Wind catcher	wind catcher
iv	Reversed wind catcher	reversed wind catcher
v	Step-up/ step-down canyons	step-up canyon step-down canyon

2.3 Canyons with Void Decks

Void decks are open spaces at the ground floor of buildings. This section studies the effects of void decks in 2D canyons. The same model blocks in section 2.2 were used, but with all blocks lifted up by 2 cm. The effective height of the canyons is therefore 14 cm, while the width remains at 12 cm. Two L-shaped aluminum bars, fixed to the walls of the partitions, were used to support the model blocks (Fig. 2.15). The aluminum bars have a thickness of 2 mm, much smaller than the partition width of 30 cm, so they do not disrupt the flow. A torpedo level was used to ensure that the model blocks remain horizontal to the ground. The middle-line velocity profiles of canyons 3, 4, 5, and 6 were measured.
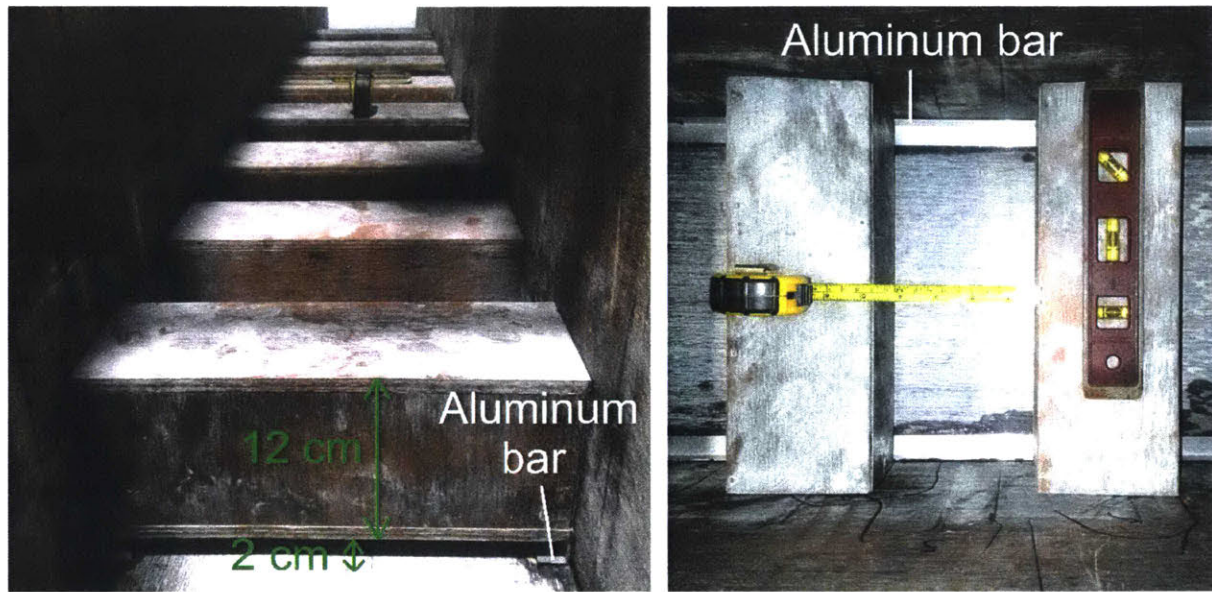
Fig. 2.15. Canyons with a 2 cm gap below the model blocks to simulate the void decks. The blocks are supported by two aluminum bars fixed to the partition walls.

Velocity profiles at the middle lines of canyons 3, 4, 5, and 6 are plotted in Fig. 2.16. The normalized stream-wise velocity profiles, u/U_{ref}, are about the same for all four canyons at $z/H >$ 0.2 (Fig. 2.16(a)). At near-ground level where $z/H < 0.2$, the difference among the canyons is significant. The largest u/U_{ref} of about 50% of the freestream velocity is recorded at the most upstream canyon 3. At canyon 4, u/U_{ref} decreases slightly to about 40%. The reduction in u/U_{ref} is consistent for the downstream canyons 5 and 6, where u/U_{ref} reduces to about 30% and 25%, respectively. Fig. 2.17 plots Fig. 2.16(a) by zooming into the region of $z/H < 0.5$ and adding the profile of the reference case (without the void decks) for comparison. For the reference case, only the profile of canyon 4 is included in Fig. 2.17, since canyons 3, 4, 5, and 6 have identical velocity profiles inside the canyons (see Fig. 2.13). Fig. 2.17 compares the near-ground flow speed, which is analogous to the pedestrian-level wind speed in a real-scale built environment. Since near-ground u/U_{ref} is negative in the reference case, the magnitude $|u|/U_{ref}$ is plotted to ease comparison. Below $z/H = 0.2$, all canyons with void decks record higher flows compared to the reference canyon without void decks. On w/U_{ref}, Fig. 2.16(b) shows that w/U_{ref} is much smaller compared to u/U_{ref}. Near the ground level, w/U_{ref} is smaller than 5% of the freestream velocity, so the void decks enhance only the horizontal (stream-wise) wind speed but not the vertical wind speed, as expected.
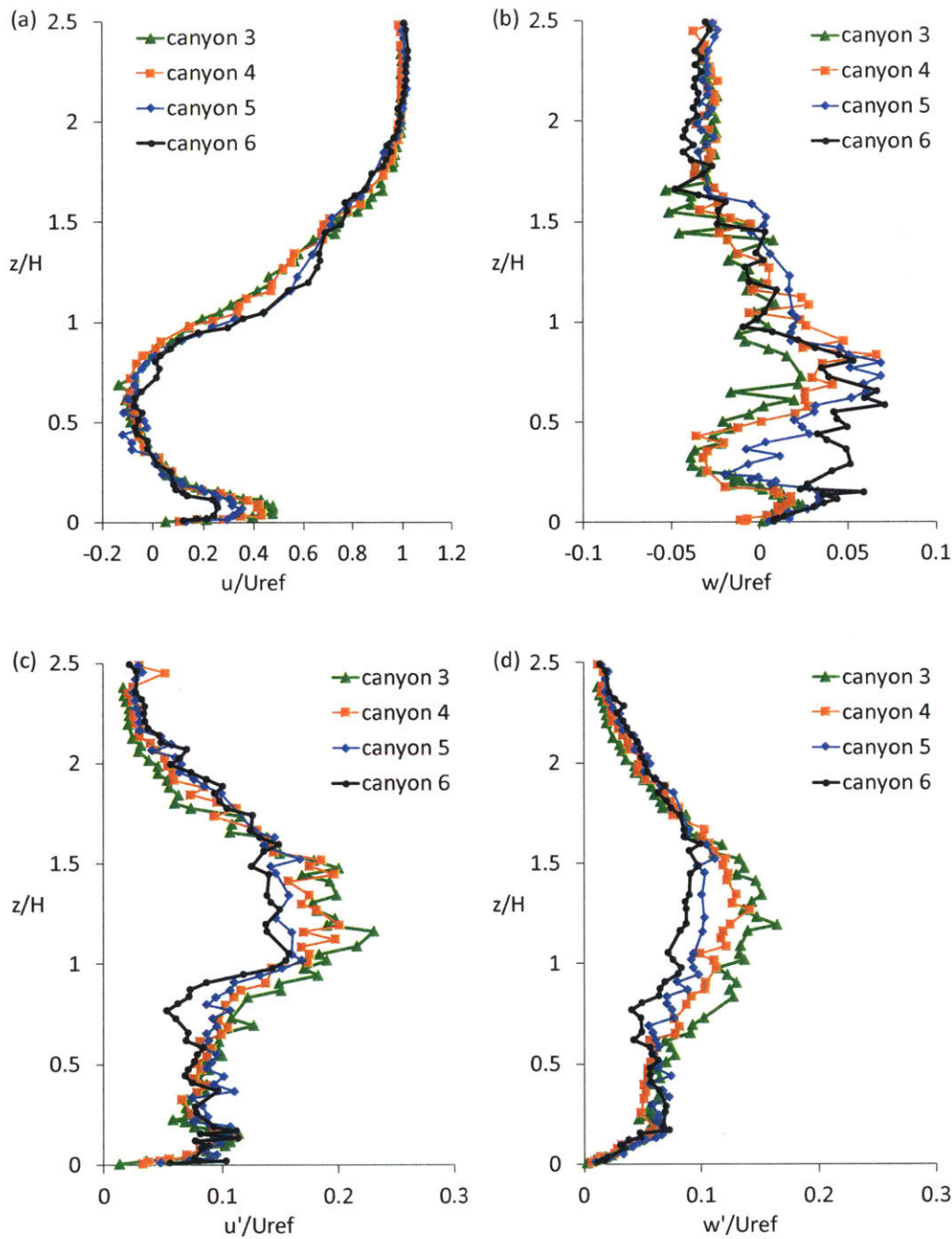
Fig. 2.16. Normalized middle-line velocity profiles at canyons 3, 4, 5, and 6 with void decks. (a) Mean stream-wise velocity, (b) mean vertical velocity, (c) stream-wise velocity fluctuation, and (d) vertical velocity fluctuation.

For turbulence, Fig. 2.16(c) and Fig. 2.16(d) show that u'/Uref is larger than w'/Uref. Inside the canyon (z/H < 1), u'/Uref is almost constant at 0.1; whereas w'/Uref increases linearly from z/H = 0 till z/H = 0.2, then stays relatively constant between z/H = 0.2 and z/H = 1.0. Both u'/Uref and w'/Uref reach a maximum between z/H = 1 and z/H = 1.5. Above z/H = 1.5, u'/Uref

28

and w'/Uref decay with increasing z/H. Another observation is that u'/Uref and w'/Uref decay downstream of the flow, with the highest u'/Uref and w'/Uref recorded above canyon 3, and the lowest u'/Uref and w'/Uref recorded above canyon 6.
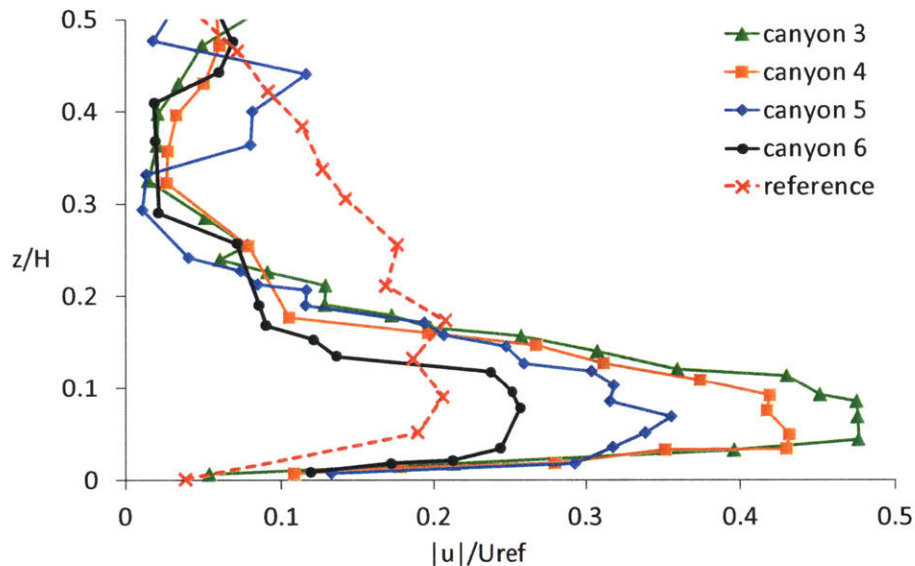
Fig. 2.17. Magnitude of stream-wise velocities at canyons 3, 4, 5, and 6 with void decks, with reference to a canyon without void deck (dashed line). At z/H below 0.2, all canyons with void decks have higher velocities compared to the reference case.

To summarize this section, the void decks proved to channel more flow into the near-ground level by allowing "jets" to flow through these openings. We quantify the flow enhancement with respect to the reference case without the void decks. The strength of these jets weakens downstream of the flow. The experiment comprised only seven canyons and measured the velocity profiles of canyons 3, 4, 5, and 6. It will be interesting to extend this study to include more canyons to locate at which canyon the jet diminishes. Due to space constrain, we could not fit additional model blocks into the experimental setup, so we use computational fluid dynamics simulation for this study, which will be discussed in section 3.3.

2.4 Canyons with a Wind Catcher

Section 2.3 discusses pedestrian-level wind speed enhancement with void decks (case (ii) in Table 2.1). Another plausible method to enhance pedestrian-level wind speed is by having a wind catcher

installed above the roof level to channel freestream flow into a canyon (case (iii) in Table 2.1). Fig. 2.18 shows a simple prototype of a wind catcher made of 1 mm thick aluminum plate. To simulate a flow across an array of canyons with a wind catcher above the target canyon 4, the wind catcher prototype that spans across the whole channel width is fixed to the sidewalls of the partitions as shown in Fig. 2.19. The sides are sealed with plasticine (the green patches in Fig. 2.19). The canyons are 12 cm × 12 cm with aspect ratio 1, similar to the canyons in section 2.2.
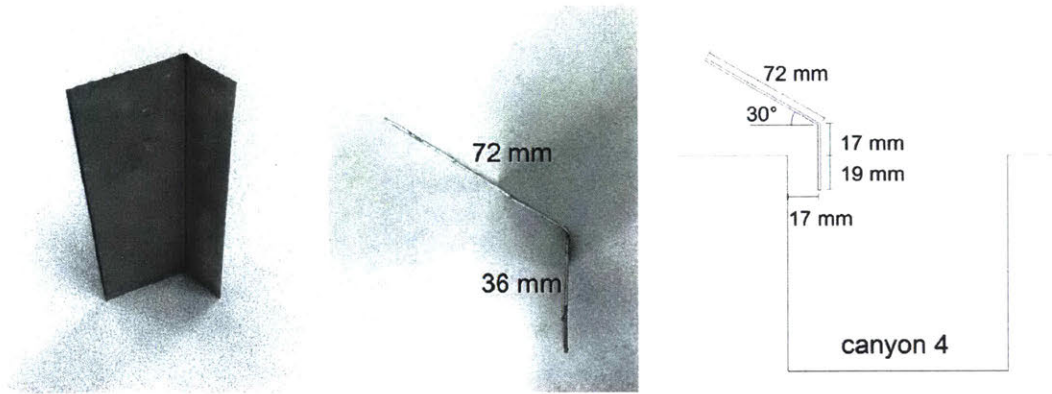

Fig. 2.18. Photos and the dimensions of the wind catcher prototype.

Fig. 2.19. A wind catcher prototype fixed to the sidewalls above the fourth model block. Left: top view where the flow direction is from the bottom to the top, right: view from the flow direction.

30

The velocity profiles at canyons 3, 4, 5, and 6 were measured and summarized in Fig. 2.20. Recall that the wind catcher is aimed at channeling flow into the target canyon 4. Fig. 2.20(a) shows that the normalized mean stream-wise velocity, u/Uref, is distinctive in canyon 4 compared to the other canyons. First, canyon 4 has a positive u/Uref below the mid-canyon height (z/H < 0.5) while the other canyons have negative u/Uref. Second, near-ground u/Uref in canyon 4 is about 2.5 times larger in magnitude compared to the other canyons. Third, u/Uref approaches zero near z/H = 0.7, and becomes negative at z/H > 0.7. This suggests a strong counter-clockwise vortex in canyon 4, with the vortex core located near z/H = 0.7. This can be explained by the protrusion of the wind catcher above the roof level, which induces additional blockage to the flow upstream. Based on the geometry in Fig. 2.18, the protrusion of the wind catcher is 5.3 cm above the roof level. The canyon height is 12 cm. The effective blockage to the flow is therefore 12 cm + 5.3 cm = 17.3 cm. The width of the canyon remains at 12 cm. If we imagine a vortex in this 17.3 cm tall by 12 cm wide canyon, the vortex becomes elongated in the vertical direction. Assuming that it is symmetrical at half the effective blockage height (17.3/2 cm = 8.65 cm), its core will be located near z = 8.65 cm above the ground level. Normalized by the canyon height H = 12 cm, we obtain z/H = 0.72, which is close to z/H = 0.7 observed in the experiment. The wake from the wind catcher is expected to affect the immediate downstream canyon 5, which records u/Uref approaching zero near z/H = 0.8. This suggests that the vortex in canyon 5 is also elongated vertically. In contrast to a counter-clockwise vortex in canyon 4, negative u/Uref below z/H = 0.5 implies that clockwise vortices form in canyons 3, 5, and 6. The normalized vertical velocity, w/Uref, remains small (< 10%) in canyons 3, 5, and 6, as shown in Fig. 2.20(b). Between z/H = 0.7 and z/H = 1.5, canyon 4 has stronger negative w/Uref of up to 10% of the freestream velocity, induced by the wake of the wind catcher. Concerning turbulence, Fig. 2.20(c) and Fig. 2.20(d) show that u'/Uref is larger than w'/Uref. Canyon 4 has the largest u'/Uref and w'/Uref, due to high shear between the freestream and the wake downstream of the wind catcher. The maximum u'/Uref and w'/Uref are recorded near z/H = 1.4, which is the protrusion height of the wind catcher. These high velocity fluctuations travel downstream so canyon 5 and canyon 6 record higher u'/Uref and w'/Uref compared to canyon 3, which is upstream of the wind catcher. Near the ground level where z/H < 0.2, u'/Uref in canyon 4 is twice as high compared to the other canyons, while w'/Uref in canyon 4 is about 50% higher compared to the other canyons.
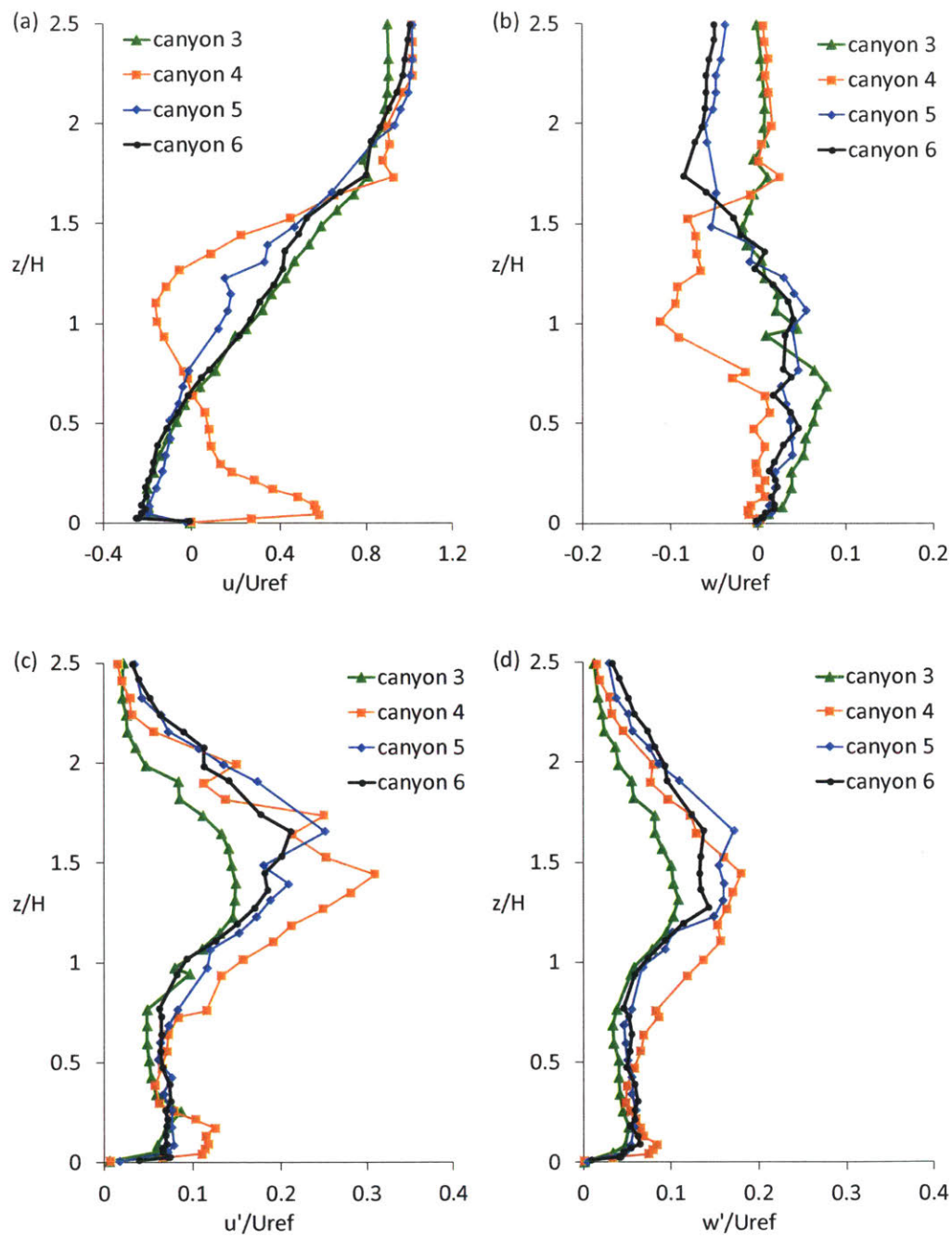
Fig. 2.20. Normalized middle-line velocity profiles at canyons 3, 4, 5, and 6 with a wind catcher. (a) Mean stream-wise velocity, (b) mean vertical velocity, (c) stream-wise velocity fluctuation, and (d) vertical velocity fluctuation.

2.5 Canyons with a Reversed Wind Catcher

In terms of pedestrian-level wind speed enhancement, the wind catcher has the highest effectiveness with its inlet oriented to the incoming wind. If the wind comes at an angle (oblique wind direction), the velocity component normal to the wind catcher can be taken as the freestream reference velocity. For example, a 1 m/s wind in a direction 45° with respect to the inlet has a freestream component of cos45° × 1 m/s = 0.7 m/s. How about a wind directed 180° to the wind catcher, i.e. a wind coming from the reversed direction? The answer is not straightforward so another experiment with a "reversed wind catcher" was conducted (case (iv) in Table 2.1). In this setup, canyon 4 is still the target canyon, as the wind catcher is nearest to canyon 4. Fig. 2.21 summarizes the middle-line velocity profiles of canyons 3, 4, 5, and 6 with a reversed wind catcher. The reversed wind catcher has little effect on the upstream canyon 3 and the target canyon 4, as the flow profiles are similar to the profiles in the reference case. At canyon 5, u/Uref drops to nearly zero throughout the whole canyon. At canyon 6, u/Uref recovers but is slightly lower compared to canyon 4. The wake from the protrusion of the wind catcher above the roof level is apparent at canyon 5, as u/Uref is negative between z/H = 1 and z/H = 1.4. Concerning turbulence, u'/Uref is larger than w'/Uref, consistent with all previous cases. In canyons 3, 4, and 6, both u'/Uref and w'/Uref are constant at about 5%, except near the ground level, where they decay to zero. In canyon 5, u'/Uref and w'/Uref are small at about 2 %. This could be due to the relatively quiescent flow in canyon 5.

The reversed wind catcher has an adverse effect in terms of flow enhancement. Wind direction, however, is usually diurnal. A wind catcher installed in the favorable wind direction during daytime becomes a reversed wind catcher at nighttime. In canyons where pedestrians are absent at nighttime, this flow reduction effect of a reversed wind catcher may not cause any impact. In canyons where nocturnal wind is important, e.g., to mitigate urban heat island intensity with night flushing (Geros et al., 2005; Pfafferott, Herkel, & Jäschke, 2003), the direction of the wind catcher inlet can be varied with a rotatable top plate. A wind catcher with a rotatable top plate can be installed at the middle of the canyon, instead of near the leeward wall.
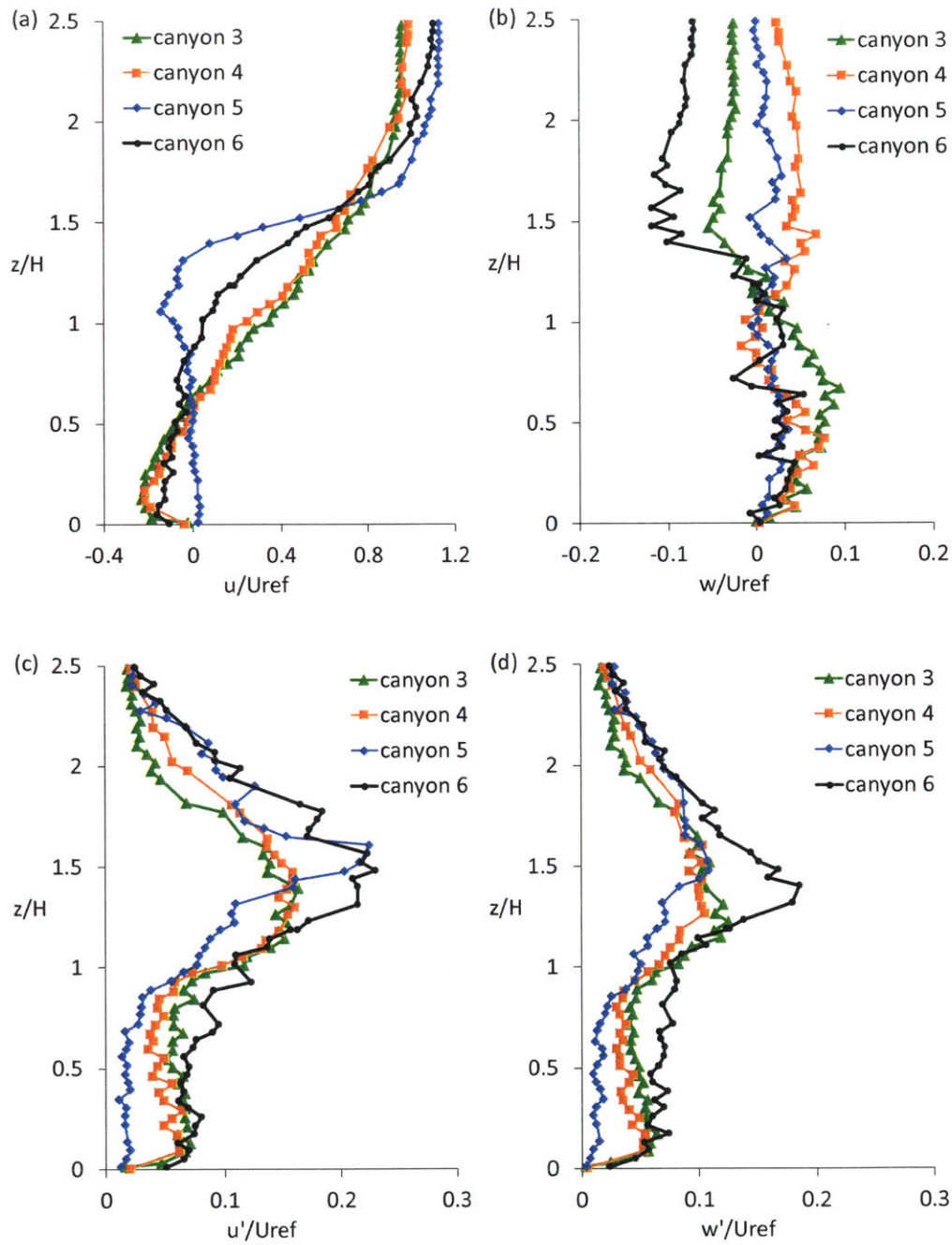
Fig. 2.21. Normalized middle-line velocity profiles at canyons 3, 4, 5, and 6 with a reversed wind catcher. (a) Mean stream-wise velocity, (b) mean vertical velocity, (c) stream-wise velocity fluctuation, and (d) vertical velocity fluctuation.

2.6 Step-up and step-down canyons

The wind catcher captures wind with an inlet protruding above the roof level, where the wind speed is higher at this elevation due to less obstruction to flow. In section 2.4, the wind catcher protrudes 5.3 cm above the roof level of a 12 cm tall canyon. Does a taller building with similar protrusion height induce similar flow enhancement effect in canyon 4? This section attempts to answer this question by studying flows across step-up and step-down canyons (case (v) in Table 2.1). A "step-up canyon" is formed between a shorter upwind building and a taller downwind building; whereas a "step-down canyon" is formed between a taller upwind building and a shorter downwind building. In this experiment, the fifth building model was 17.3 cm tall (to match the effective blockage height in case (iii)), while all other building models remained at 12 cm tall, as shown in Fig. 2.22. Canyon 4 is a step-up canyon, while canyon 5 is a step-down canyon. The velocity profiles of canyons 3, 4, 5, and 6 were measured.
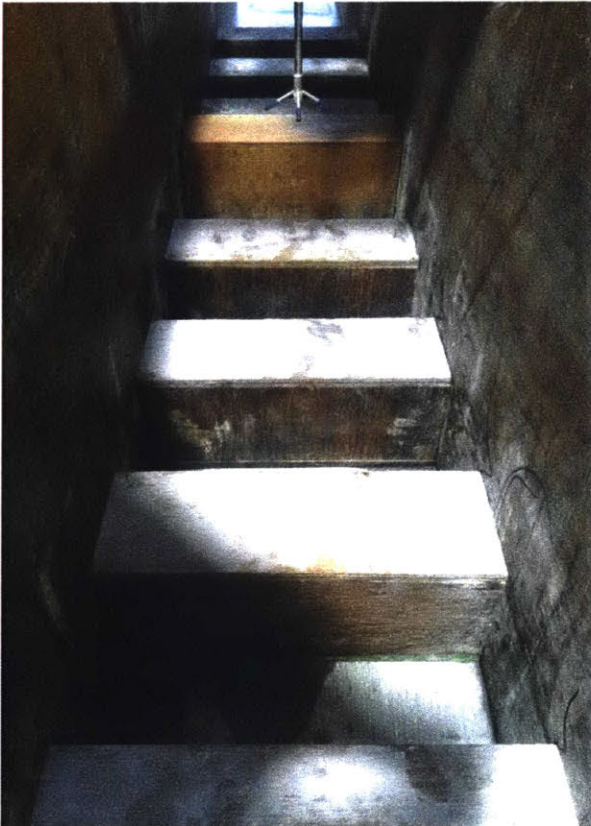
Fig. 2.22. Experimental setup with the fifth model block replaced by a taller 17.3 cm block. All other blocks are 12 cm tall. Canyon 4 is a step-up canyon, while canyon 5 is a step-down canyon.
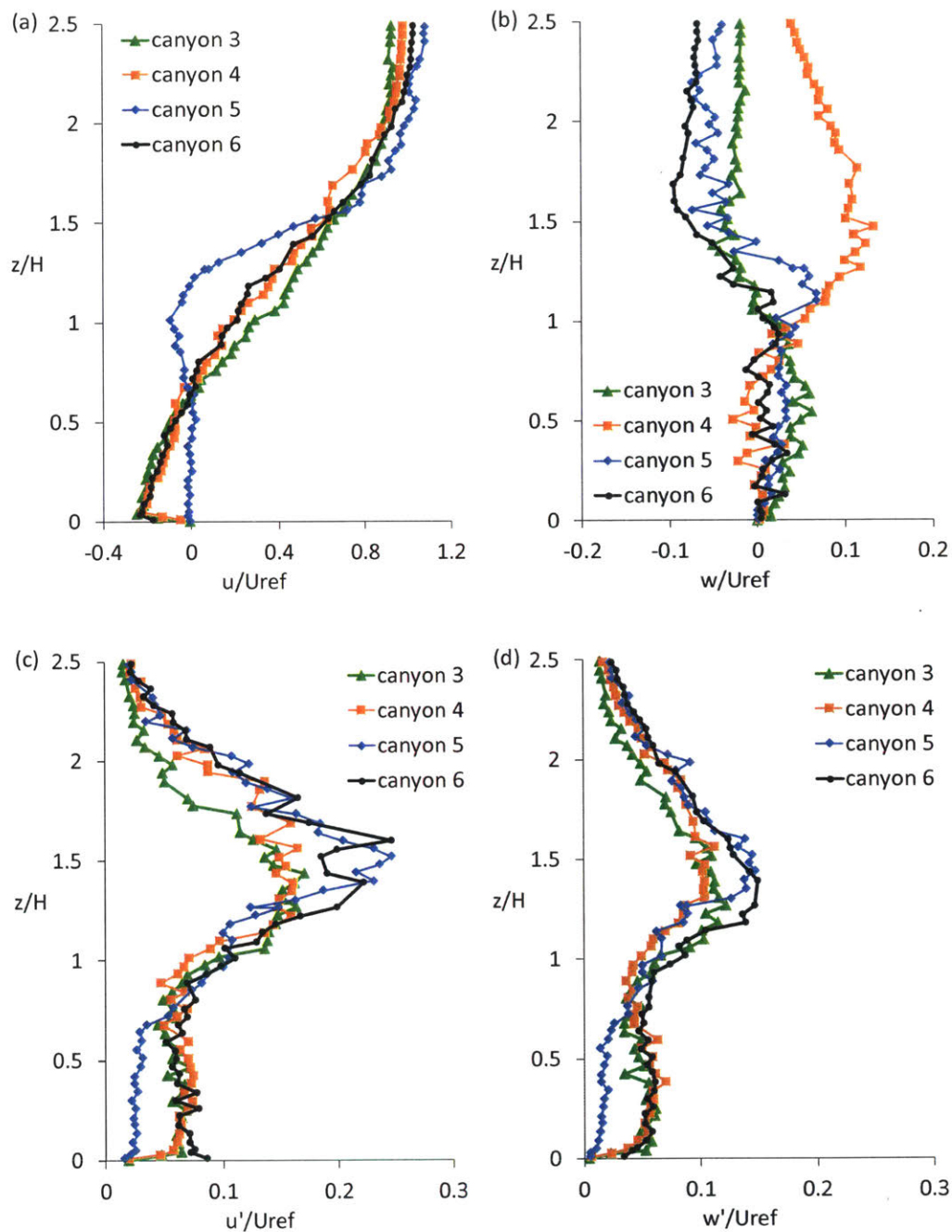
Fig. 2.23. Normalized middle-line velocity profiles at canyons 3, 4, 5, and 6 with step-up/step-down canyons. (a) Mean stream-wise velocity, (b) mean vertical velocity, (c) stream-wise velocity fluctuation, and (d) vertical velocity fluctuation.

Fig. 2.23 summarizes the experimental results for the case with step-up and step-down canyons. The profiles of u/Uref, u'/Uref and w'/Uref are similar to the profiles in the case of a reversed wind catcher (Fig. 2.21(a), (c), and (d)), where the tall building does not enhance near-

ground flow in canyon 4, and canyon 5 records almost zero flow. This means that the tall building obstructs the flow in a similar fashion as the reversed wind catcher. The profiles of w/Uref are also comparable, except above canyon 4. Compared to the reversed wind catcher in Fig. 2.21(b), Fig. 2.23(b) shows that w/Uref above canyon 4 in this case is slightly higher. This may be due to the geometry of the blockage. In the case with a reversed wind catcher, the flow above canyon 4 has a milder turn of 30° when it approaches the sloped plate of the reversed wind catcher. In the case with a tall building downwind of canyon 4, the flow approaching building 5 (the downwind building of canyon 4) has to turn 90° to align with the vertical windward wall of building 5. The abrupt turning of 90° induces a higher w/Uref compared to a milder turn of 30° in the case with a reversed wind catcher.

2.7 Comparison between Void Decks, Wind Catcher and Step-up/step-down canyons

The effects of void decks, a wind catcher, a reversed wind catcher, and step-up/step-down canyons were studied experimentally in a recirculating water channel. To compare their effects on the pedestrian-level wind speed, Fig. 2.24 plots separately the velocity profiles in canyons 3, 4, 5, and 6, comparing the four types of architectural interventions to the reference case with canyons of aspect ratio 1. Since we focus on the pedestrian-level wind speed, and considering that the vertical velocity is small near the ground level, only $|u|/Uref$ is plotted. Fig. 2.24(a) shows that in canyon 3, near-ground flow enhancement occurs only in the case with void decks. Installing a wind catcher (even in the reversed direction) or having a taller building downstream does not affect the flow in canyon 3. Fig. 2.24(b) shows that in canyon 4, the reversed wind catcher and the tall building have no effect on near-ground wind speed. The wind catcher enhances near-ground wind speed by about 2.5 times, whilst the void decks enhance near-ground wind speed by about 2 times. In canyon 5, Fig. 2.24(c) shows that the tall building and the reversed wind catcher reduce the flow to nearly zero, while the void decks enhance near-ground wind speed by about 1.5 times. The wind catcher has no effect on the flow in canyon 5. Lastly, Fig. 2.24(d) shows that in canyon 6, all cases have about the same near-ground wind speed, except the case with a reversed wind guide, which has a slightly lower flow.

37

In summary, void decks are the most effective means to enhance pedestrian-level wind speed, but this enhancement effect weakens at downstream canyons. In terms of wind speed enhancement of a single targeted canyon, the wind catcher is the most effective. The wind catcher, however, has a drawback: when the wind is coming from the opposite direction, it becomes a "reversed wind catcher." A reversed wind catcher does not enhance the flow in the target canyon and reduces the flows in the downstream canyons. A tall building does not enhance the flow in the target canyon and reduces the flow in the immediate downstream canyon. Canyons further downstream are not affected by the tall building.
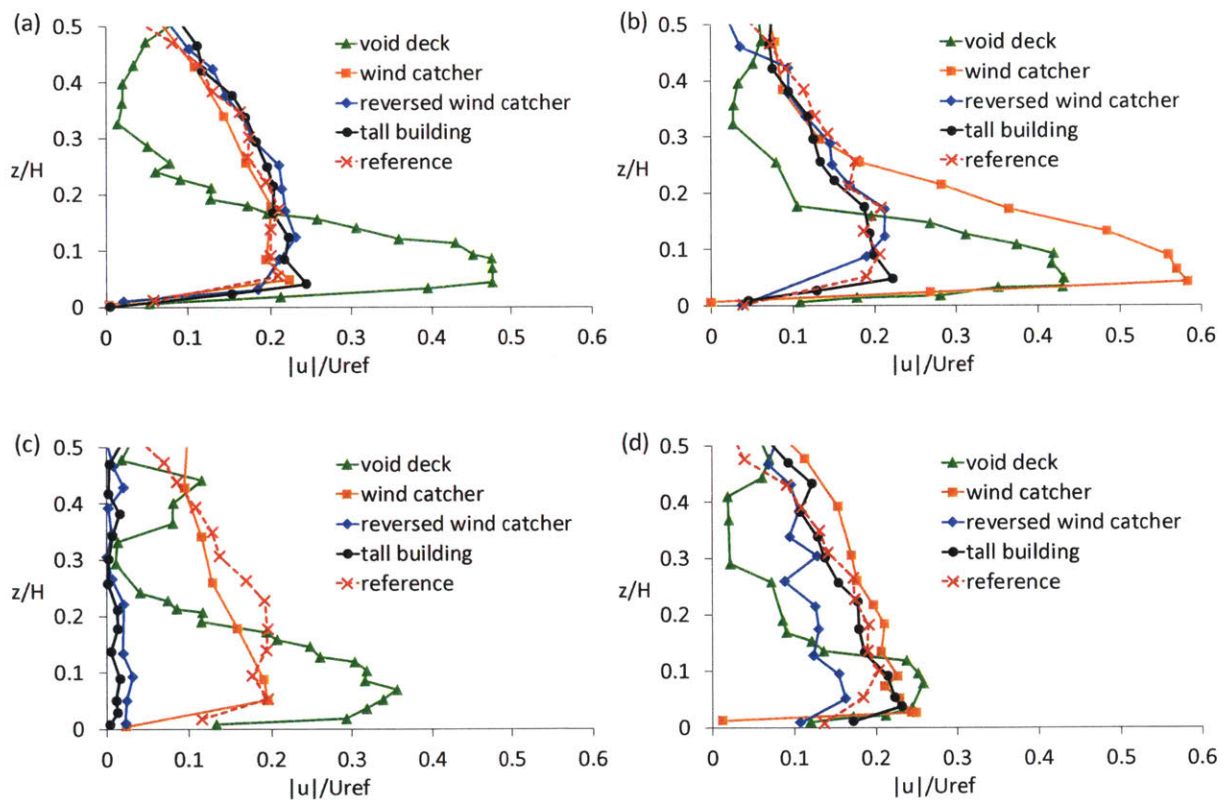
Fig. 2.24. Normalized stream-wise velocity (magnitude) comparing the cases of void decks, a wind catcher, a reversed wind catcher, and step-up/step-down canyons to the reference case with canyons of aspect ratio 1 in: (a) canyon 3, (b) canyon 4, (c) canyon 5, and (d) canyon 6.

Lastly, it must be noted that the experiments were conducted with 2D canyons where the span-wise flow is negligible. Therefore, these results are only applicable to 2D urban street canyons, i.e. canyons with small height to (span-wise) length aspect ratio. Furthermore, we only studied canyons with aspect ratio 1. The results should not be generalized to canyons with very small or very large aspect ratio, i.e. wide canyons and narrow canyons. We also note that these

experiments are "proof of concept" studies to demonstrate the feasibility of different types of architectural interventions to enhance pedestrian-level wind speed. The geometries are not varied in these experiments. There are many combinations of geometrical parametric studies. It will be interesting to study the optimization of geometrical features of these interventions, such as the height of void decks with respect to the building height; the length and angle of the wind catcher; and the shape of the wind catcher. Validated CFD models are excellent tools to study these variations, as they are more cost effective than repeating experiments to study different geometries.

Chapter 3 Numerical Simulations of 2D Canyons

In this chapter, we repeat the studies of all experimental cases with computational fluid dynamics (CFD) simulations. Both the experimental and computational approaches have their strengths and weaknesses. For example, we could not perform flow visualization with our experimental setup because the partition walls were not transparent. A validated CFD model serves as a valuable tool to complement this drawback of experiments, as the CFD model can reveal the holistic flow fields. We also need to use CFD models to study the flow across a real-scale built environment, since full-scale building models will not fit even in the largest wind tunnel and water channel. CFD simulations are usually cheaper than experiments. However, CFD models must be validated with experimental data and should not be used as a stand-alone analysis tool. Section 3.1 discusses CFD model validation, followed by simulations and results of the reference case with an array of canyons of aspect ratio 1 in section 3.2. Sections 3.3, 3.4, 3.5, and 3.6 discuss the simulations and results of the case with void decks, the case with a wind catcher, the case with a reversed wind catcher, and the case with step-up/step-down canyons, respectively.

3.1 CFD Model Validation

We use ANSYS DesignModeler for modelling and ANSYS Meshing for mesh generation (ANSYS, 2017). The open-source, finite volume solver Open Field Operation and Manipulation (OpenFOAM, 2017), was adopted for CFD simulations. Meshes generated from ANSYS Meshing can be converted to OpenFOAM-compatible format easily with built-in utilities in OpenFOAM. All simulations were run with OpenFOAM version 3.0.1 in the Linux platform (Ubuntu 15.10) in a Dell Workstation (Precision Tower 7910) with 48 processors. OpenFOAM built-in utilities also allow efficient parallelized CFD simulations based on the Message Passing Interface (MPI) methodology. Up to 46 processors were used for a single run, depending on the number of grids in the mesh. Post-processing was done with the open-source software ParaView (ParaView, 2017).

Fig. 3.1 shows the three-dimensional (3D) CFD models and the name of each boundary. The CFD model has similar geometrical dimensions as the experimental setup, except in the span-wise direction, where a periodic boundary condition was applied, so the span-wise length was reduced. In both the experiments and the CFD model, the height of the canyon was H. For canyons

40

with aspect ratio 1, the canyon width equals H. The span-wise length in the experiments was 2.5H. In the CFD model, the span-wise length was H, and a periodic boundary condition was applied in the span-wise direction. This means that the CFD model is infinitely long in the span-wise direction, which is consistent with the 2D flows of the experiments. The free surface (top) was not explicitly modeled, as the velocity profiles in the experiments show that the velocity gradient approaches zero near the free surface, which can be represented by a symmetric boundary condition. The top surface was at least 3H from the ground, corresponded to the water depth in the experiments. The inlet, located 4H from the first model block, was prescribed with the velocity profile measured in the experiments at the same location. The outlet, located 15H from the last block (Franke et al., 2004), had a zero-gradient boundary condition. All walls including the bottom had a no-slip boundary condition. The standard wall function was employed to reduce computational cost by allowing a coarser mesh (Aliabadi et al., 2017). The built-in steady Reynolds-averaged Navier-Stokes (RANS) solver, "simpleFOAM," was used with the k-ε turbulence closure scheme.
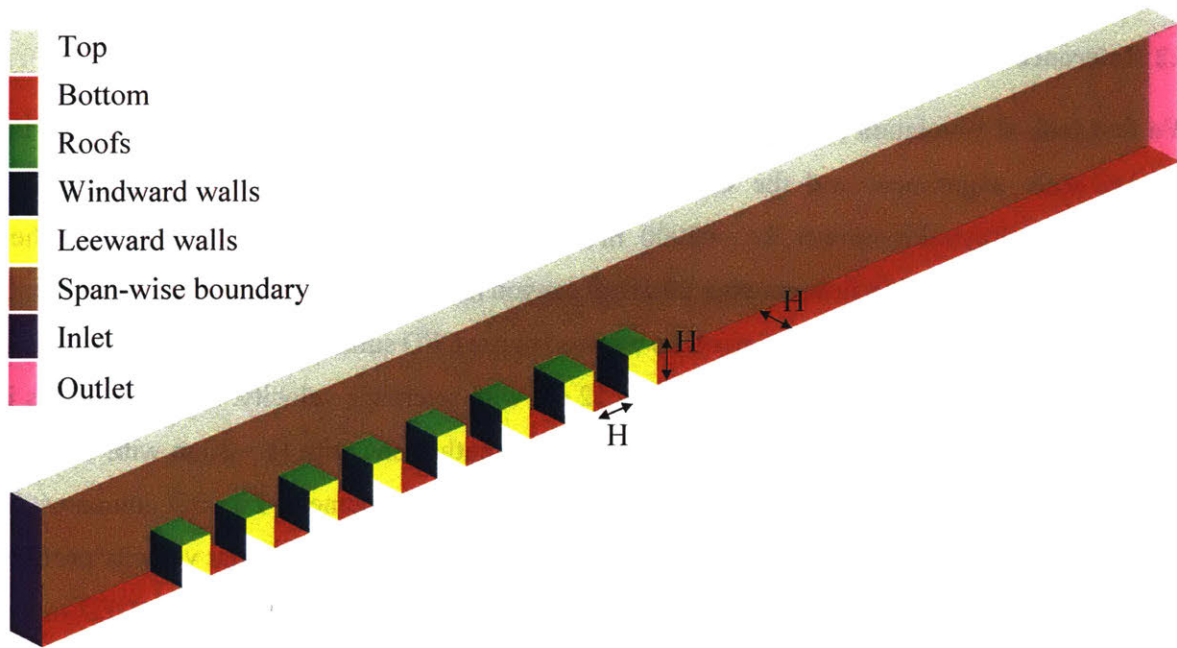

Fig. 3.1. CFD model of seven canyons with aspect ratio 1.

Fig. 3.2 shows the mesh viewed from the front (only the first four canyons are shown). The model has 2.5 million grids in total. The canyons have a fine mesh resolution with uniform square grids of grid size H/60. The same resolution is maintained above the roof level up to 1.8H. Above

1.8H, the mesh is coarsened. Similarly, the mesh is coarsened upstream of the first building and downstream of the last building (not shown) to reduce the total number of grids. The maximum mesh expansion ratio is 1.2. The span-wise direction has 25 uniform grids.
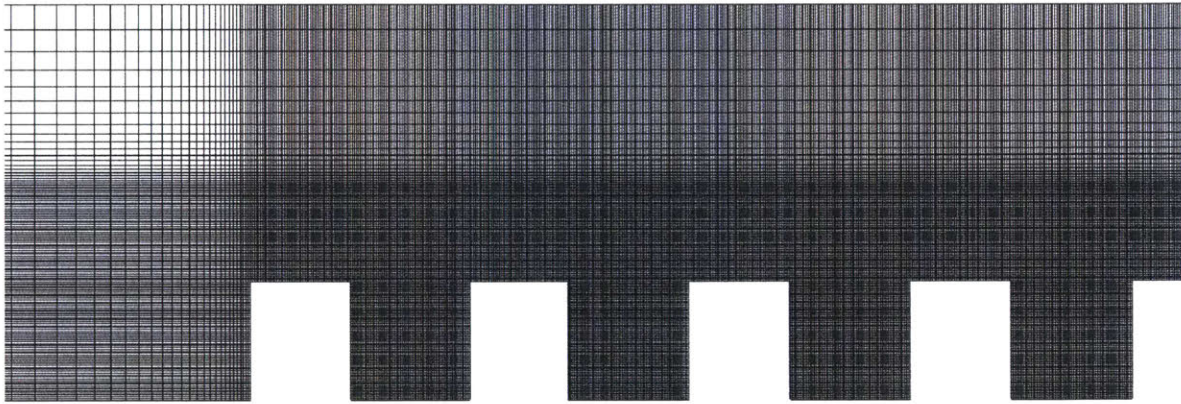

Fig. 3.2. Mesh resolution of the CFD model (only the first four canyons shown).

3.2 Reference Case with Canyons of Aspect Ratio 1

We first look at simulation results of the reference case with canyons of aspect ratio 1. Both the reduced-scale experiment and the CFD model have a canyon height, H = 12 cm, and a corresponding Reynolds number, Re = 62000. In a real-scale built environment, Re is much higher. For example, a 2 m/s wind flow across a 20 m tall canyon has Re = 3.8×10^6. Such high Re cannot be achieved in reduced-scale experiments so we need to use CFD simulations for full-scale studies. Two CFD simulations were run: one with H = 12 cm with reference velocity, Uref = 0.52 m/s in water (Re = 62000, matched to Re in the experiment); another one with H = 20 m with Uref = 2 m/s in air (Re = 3.8×10^6) to simulate the real-scale built environment. Fig. 3.3 compares the simulation results with the experiment. Since canyons 3, 4, 5, and 6 have similar velocity profiles, for brevity, only the velocity profiles at canyon 4 are plotted. Overall, the full-scale CFD model produced results similar to the reduced-scale CFD model, verifying that the reduced-scale CFD model (and the reduced-scale experiment) is representative of flows across full-scale built environments. Compared to experimental data, Fig. 3.3(a) shows that the CFD model slightly under-predicted the normalized stream-wise velocity, u/Uref, at both scales. For vertical velocity, w/Uref, Fig. 3.3(b) shows that the CFD model predicted lower w/Uref at both scales. Fig. 3.3(c) and Fig. 3.3(d) show that above the roof level (z/H > 1, where z is the vertical distance, normalized

42

by the canyon height H), the normalized stream-wise velocity fluctuation, u'/Uref, and the normalized vertical velocity fluctuation, w'/Uref, agree well with the experiment. Inside the canyon (z/H < 1), CFD models predicted lower turbulence. Also note that the k-ε turbulence closure scheme produces isotropic turbulence so u'/Uref equals w'/Uref in the CFD simulations.
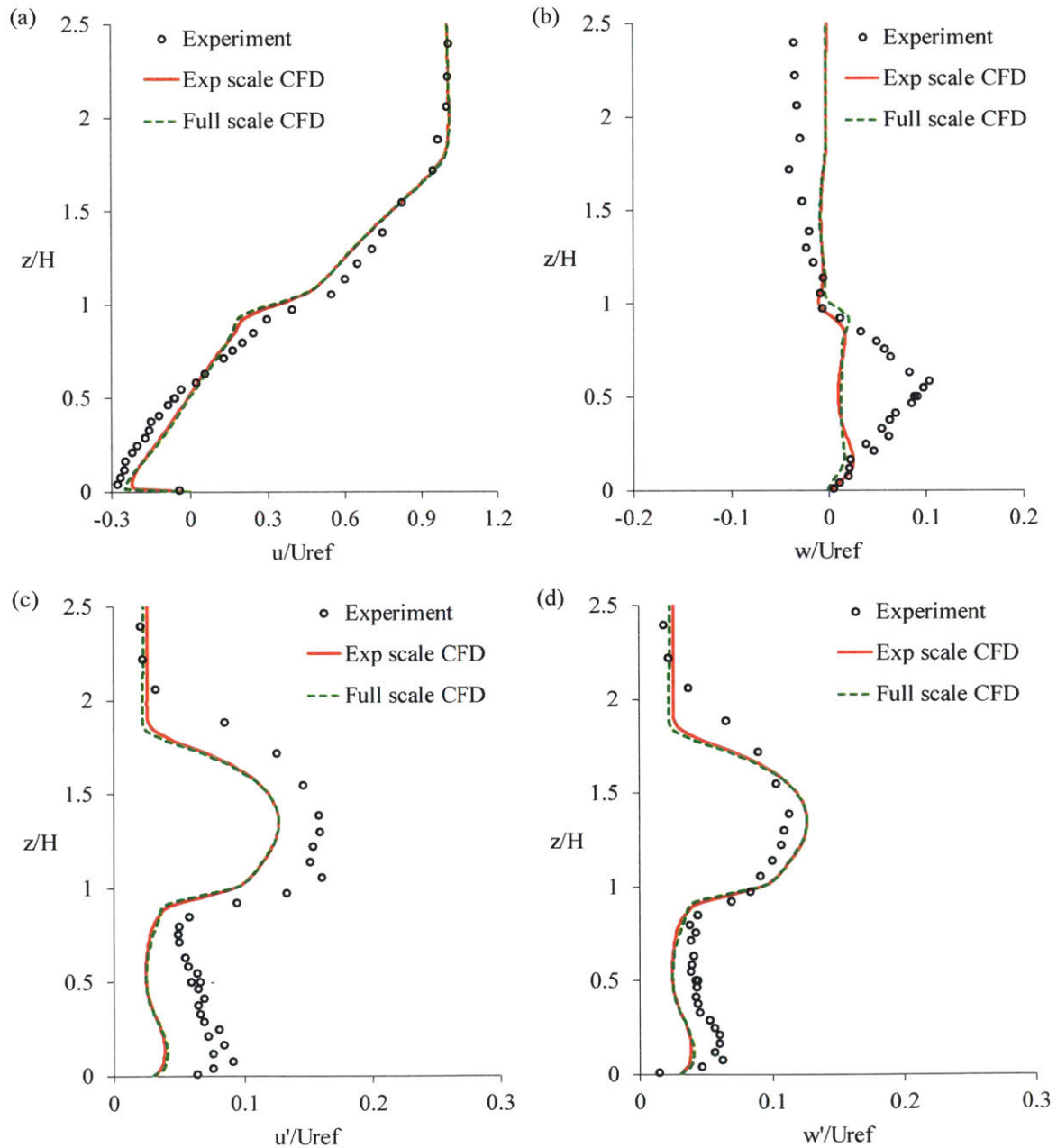

Fig. 3.3. Normalized middle-line velocity profiles at canyons 4 comparing experimental and CFD results. (a) Mean stream-wise velocity, (b) mean vertical velocity, (c) stream-wise velocity fluctuation, and (d) vertical velocity fluctuation.

43

Fig. 3.4 plots the middle-plane normalized velocity magnitude (Umag/Uref) contours and vectors of canyons 3, 4, 5, and 6. Since the flow inside a canyon is weaker than the freestream flow, the scale of Umag/Uref ranges between 0 and 0.5 (not 1.0) to highlight the flows in the canyons. Regions with Umag/Uref > 0.5 have the same color as regions with Umag/Uref = 0.5. Fig. 3.4 shows that all canyons exhibit identical flow fields with a large clockwise-rotating vortex in each canyon. Each vortex has its core near the center of the canyon. The maximum near-ground velocity is about 25% of the freestream velocity, in agreement with the velocity profile in Fig. 3.3.

Fig. 3.4. Normalized velocity magnitude contours and vectors in canyons 3, 4, 5 and 6. All canyons have identical flow field with a large clockwise-rotating vortex.

3.3 Canyons with Void Decks

This section discusses the simulation results of the CFD models with void decks. Experimental results show that void decks are effective in enhancing near-ground flows in canyons, but the enhancement effect weakens with downstream canyons. A question to ask: at which canyon does the near-ground flow become zero? This question cannot be answered with the experimental setup, as the setup comprised only seven canyons and zero flow does not occur at canyon 7. We need to add more canyons to study the flow behavior beyond canyon 7. Furthermore, we also need to examine the effects of void decks in a real-scale built environment. Therefore, three sets of simulations were run: (i) experimental scale with seven canyons (Exp scale CFD-7), (ii) experimental scale with fifteen canyons (Exp scale CFD-15), and (iii) full scale with fifteen canyons (Full scale CFD-15). Case (i) is a direct replicate of the experimental setup comprises seven canyons with Re = 62000; case (ii) has an extended domain comprises fifteen canyons with Re = 62000. Case (iii) is a full-scale model comprises fifteen canyons in a real-scale built environment with Re = 5.1×10^6.
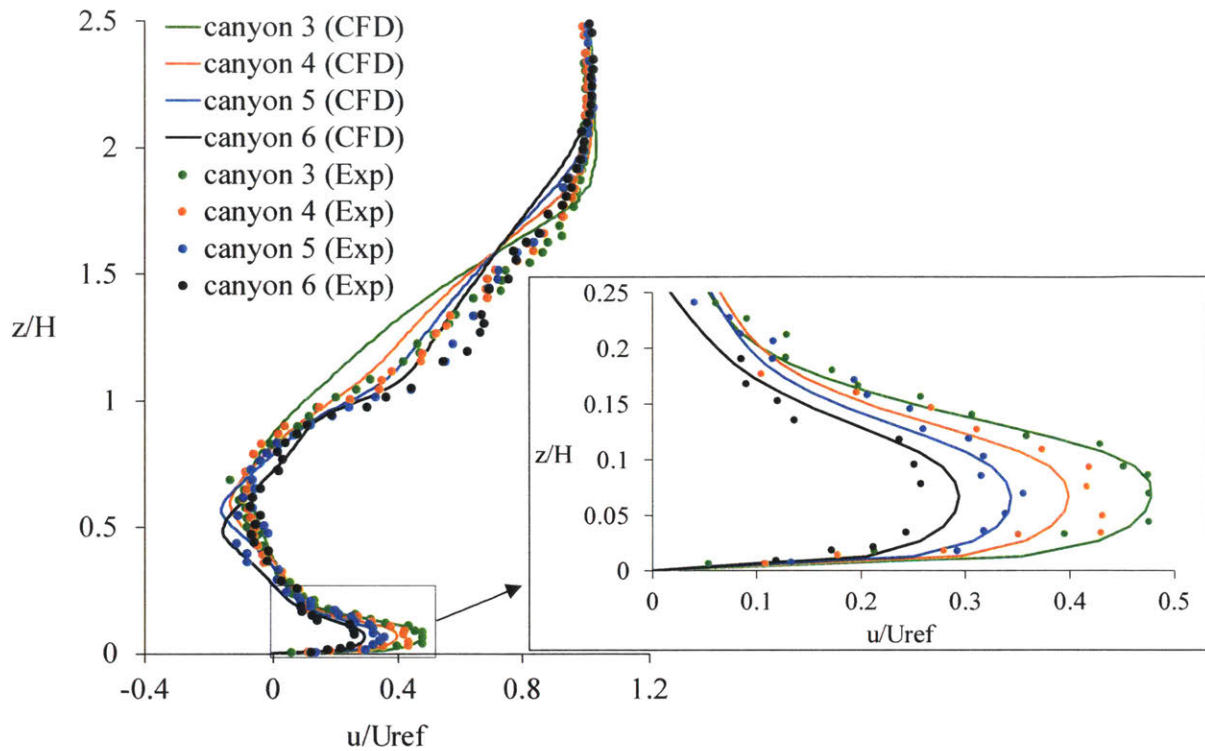
Fig. 3.5. CFD model validation with experiment for the case with void decks.

To validate the CFD models, we first compare case (i) Exp scale CFD-7 with the experimental results. Fig. 3.5 plots the experimental results as filled circles and the CFD results as solid lines. The CFD model not only predicted velocity enhancement in the canyons, it also predicted the reduction of the jet velocity when the jet travels downstream, as shown in the zoomed-in box. Having validated the CFD model in case (i), which replicates the experiment, we now compare case (i) Exp scale CFD-7 with case (ii) Exp scale CFD-15. For brevity, only the velocity profiles in canyon 4 are plotted. Fig. 3.6 shows that the red solid line (case (i) Exp scale CFD-7) and green dashed line (case (ii) Exp scale CFD-15) collapse into a single curve, confirming that extending the simulation domain to include more canyons does not affect the results. This justifies the domain extension in the CFD model to study an array with more than seven canyons. Next, we compare case (ii) Exp scale CFD-15 with case (iii) Full scale CFD-15, both have fifteen canyons but at different scales. Near the ground level, the velocity jet has a higher speed in the real-scale case compared to the experimental-scale case. This can be explained by Reynolds number. The real-scale case has a Reynolds number two orders of magnitude higher than the experimental-scale case, so viscous dissipation is much smaller in the real scale. This explains why

the velocity jet has a higher speed in the real-scale case, as its momentum loss (to the ground and to the roofs of the void decks) are smaller in the real-scale case.

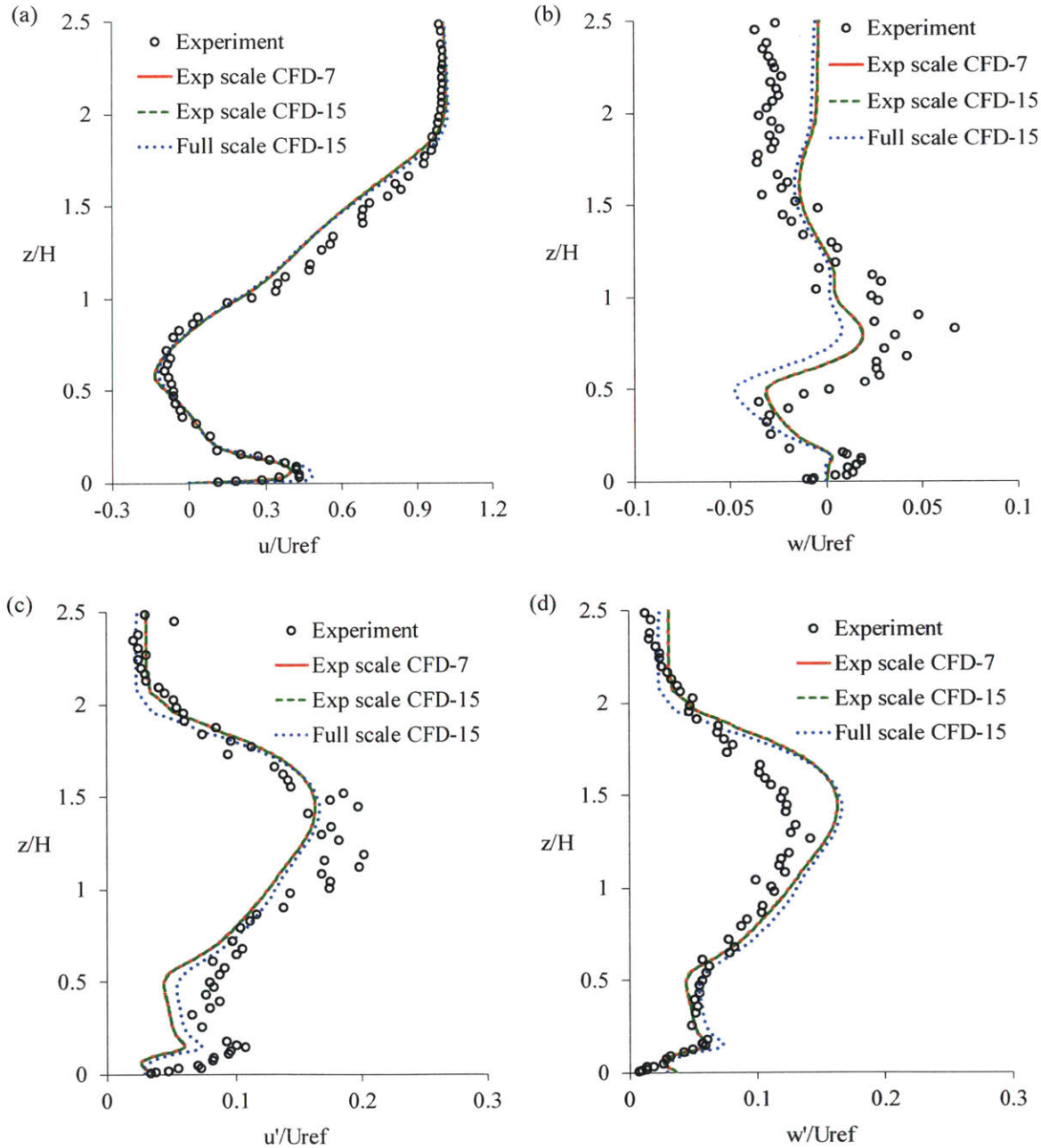Fig. 3.6. Normalized middle-line velocity profiles at canyons 4 comparing experimental and CFD results. (a) Mean stream-wise velocity, (b) mean vertical velocity, (c) stream-wise velocity fluctuation, and (d) vertical velocity fluctuation. "Exp scale" and "Full scale" are experimental scale and real scale in a built environment; "CFD-7" and "CFD-15" are CFD results with seven and fifteen canyons.

46

Next, we plot the contours of the normalized velocity magnitude of the middle plane of canyons 3 to 6 in Fig. 3.7. Since all cases (i), (ii), and (iii) have almost identical flow patterns, only case (i) Exp scale CFD-7 is plotted. It provides insight that near-ground velocity reduces in magnitude as the velocity jet travels downstream, losing momentum to the ground and to the roofs of the void decks. All four canyons have two observable vortices. The bottom vortices, which are fed by the jets exiting the void decks, shrink in downstream canyons while the top vortices grow. From the flow fields, we expect the near-ground velocity to reduce to zero and the bottom vortex to disappear further downstream of canyon 6.
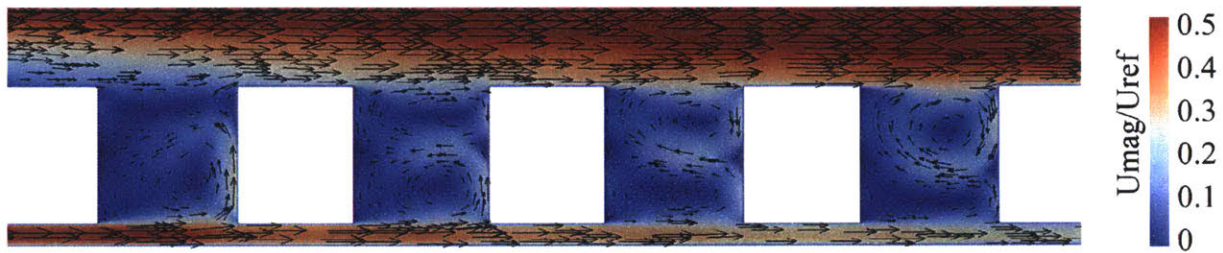

Fig. 3.7. Normalized velocity magnitude contours and vectors in canyons 3, 4, 5 and 6. Near-ground velocity reduces in magnitude traveling downstream. There are two vortices in all canyons.

In section 2.3, we observe experimentally that the near-ground flows in canyons 3, 4, 5, and 6 are 50%, 40%, 30%, and 25% of the freestream velocity, respectively. This trend suggests that further downstream canyon may have even lower or no flows. We have shown that extending the CFD simulation domain has no effect on the results. Therefore, we are now ready to use the extended CFD model with fifteen canyons in a real-scale built environment to study near-ground flows beyond canyon 6. More specifically, we want to answer the question: at which canyon does the near-ground velocity reduce to zero? Plotting the stream-wise velocity profiles of selected canyons from case (iii) Full scale CFD-15, Fig. 3.8 shows that this happens at canyon 13. Upstream of canyon 13, near-ground velocity decreases with downstream canyons. Downstream of canyon 13, near-ground velocity changes direction. The velocity profile in canyon 14 resembles the profile in the reference case without void decks (see Fig. 3.3(a)). This means that the presence of void decks has no effect on near-ground wind speed downstream of canyon 13. We then repeated the simulation by further extending the domain to 20 canyons. The model with 20 canyons also shows that this transition occurs at canyon 13, suggesting that the downstream condition does not affect the transition.
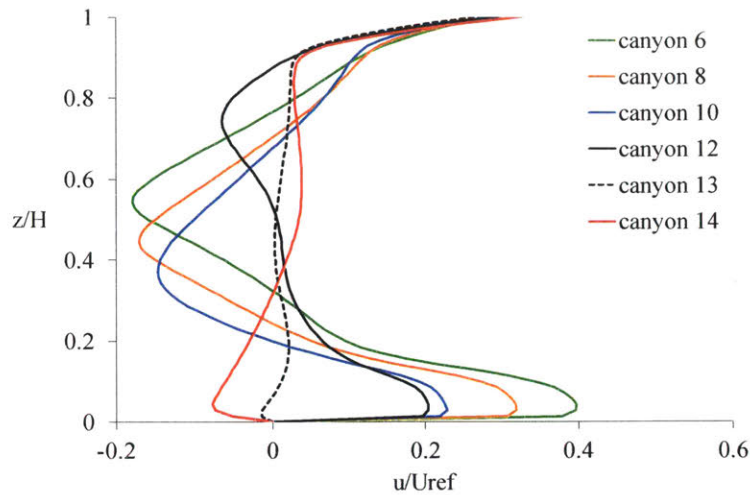
Fig. 3.8. Near-ground stream-wise velocity decreases at downstream canyons, and reduces to almost zero at canyon 13. Downstream of canyon 13, the velocity changes direction. For clarity, only profiles in selected canyons are plotted.

Fig. 3.8 shows that zero near-ground velocity is expected at canyon 13 in a real-scale built environment. To visualize this transition, the normalized velocity magnitude contours of canyons 11 to 14 are plotted in Fig. 3.9. In canyon 11, the bottom vortex has almost disappeared but there is still little flow near the ground level. In canyon 12, interestingly, the top vortex shrinks and there is little flow inside the canyon. The (weak) jet exiting the upstream void deck flows through canyon 12 and enters the downstream void deck. When this jet leaves canyon 13, it turns vertically upward to exit the canyon through the roof level. The freestream flow feeds a clockwise-rotating vortex in canyon 13. Near the ground level, this vortex drives a flow in the negative x-direction, whereas the jet that exits from the void deck is in the positive x-direction. These two countering flows result in zero near-ground velocity in the middle, which explains the velocity profile of canyon 13 in Fig. 3.8. In canyon 14, there is only one clockwise-rotating vortex, with its core shifted downstream in the canyon.
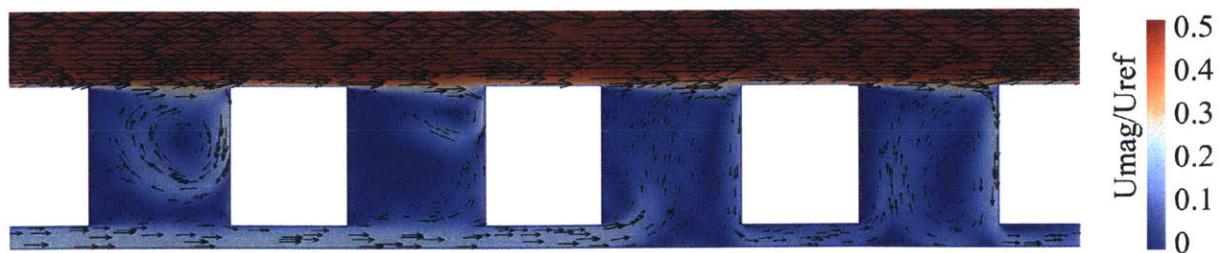

Fig. 3.9. Normalized velocity magnitude contours and vectors in canyons 11, 12, 13 and 14.

48

3.4 Canyons with a Wind Catcher

This section studies the effect of a wind catcher with CFD simulations. Fig. 3.10 shows that the CFD model reproduced the flow patterns by predicting flow enhancement in canyon 4. However, it under-predicted the near-ground velocity, especially in canyon 4. This could be due to the inherent limitation of RANS models. We repeated the simulation with large eddy simulation (LES) and recovered the high-speed velocity tip (not shown). However, despite being more accurate, LES is much more computationally expensive, which renders it unfeasible for our studies with many simulation cases. Next, we plot the profiles of u/Uref, w/Uref, u'/Uref, and w'/Uref in canyon 4. Fig. 3.11 shows that all profiles agree with experimental data. We then repeated the CFD simulation by scaling the canyon height from 12 cm to 12 m and changed the fluid from water to air to simulate a real-scale built environment. Correspondingly, Reynolds number increased from 5.5×10^4 to 2.4×10^6. Although the Reynolds numbers differ by two orders of magnitude, the normalized velocity profiles at both scales coincide with each other, justifying that our reduced-scale experiments can reproduce the flow patterns with a wind catcher in a full-scale built environment.
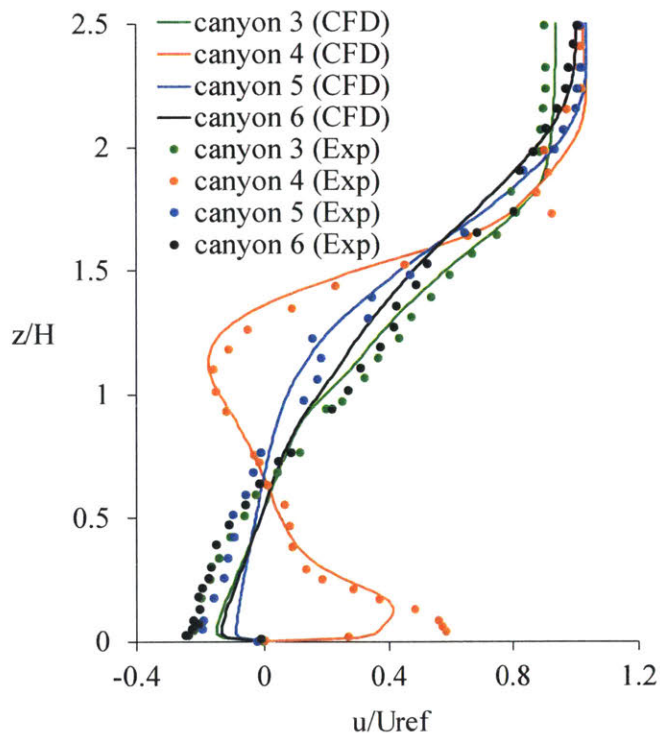
Fig. 3.10. CFD model validation with experiment for the case of a wind catcher.

49
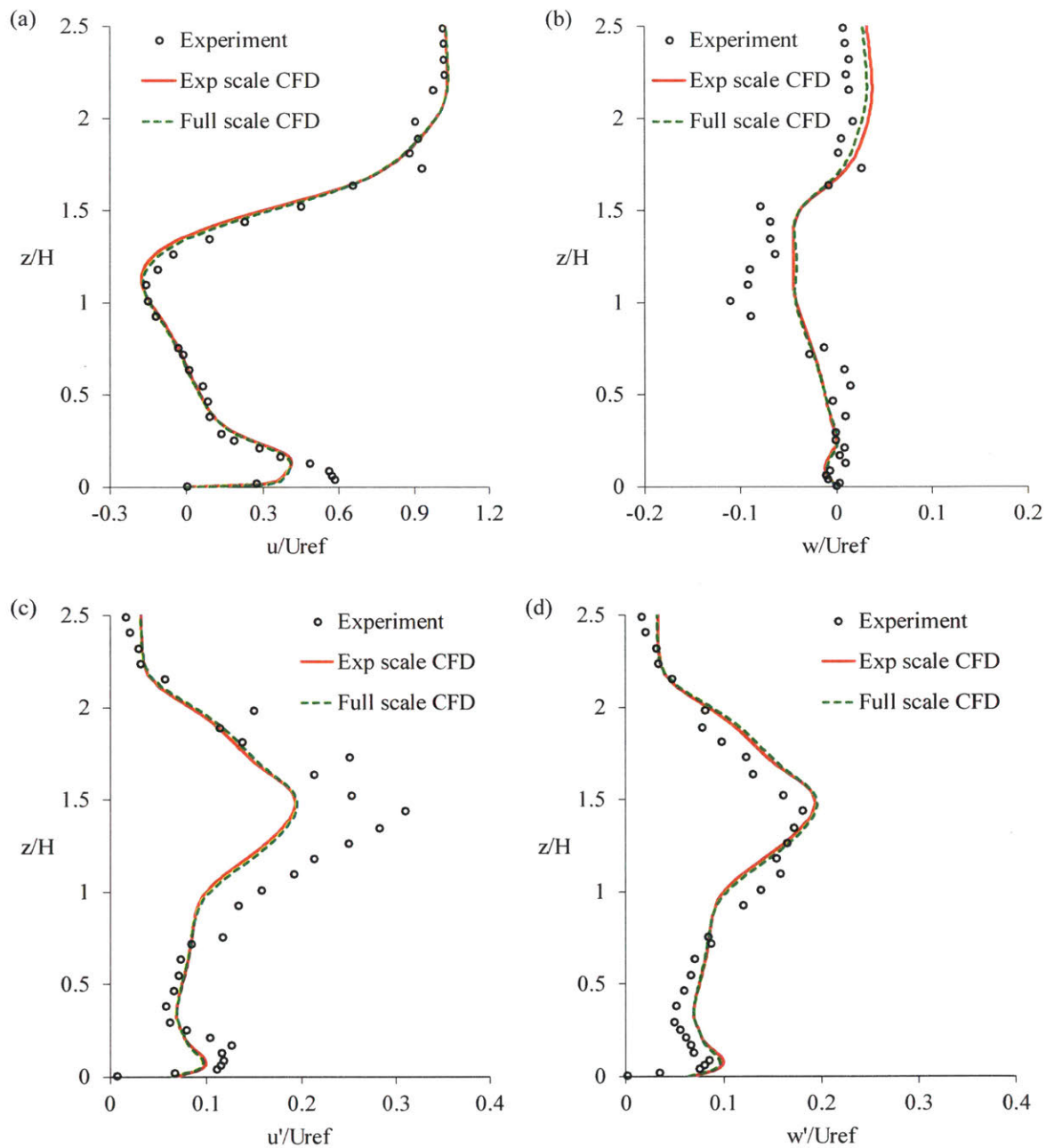
Fig. 3.11. Normalized middle-line velocity profiles at canyons 4 comparing experimental and CFD results. (a) Mean stream-wise velocity, (b) mean vertical velocity, (c) stream-wise velocity fluctuation, and (d) vertical velocity fluctuation. "Exp scale" and "Full scale" are experimental scale and real scale in a built environment.

To visualize the flow field, Fig. 3.12 plots the middle-plane normalized velocity magnitude contours and vectors of canyons 3 to 6. The velocity contours reveal how the wind catcher channels atmospheric wind into the target canyon 4. Atmospheric wind captured at the inlet increases its

50

momentum while squeezing through the narrowing channel between the roof and the top plate of the wind catcher. The high-speed jet exiting the outlet of the wind catcher travels vertically downward and turns into the stream-wise direction upon impinging the ground, boosting wind speed at the pedestrian level. This jet then turns again and moves up along the windward wall, before exiting to the atmosphere. The positive upward flow along the windward wall and the negative downward flow along the leeward wall induces a strong counter-clockwise vortex, as opposed to clockwise vortices formed in canyons 3, 5, and 6. The wake due to the protrusion of the wind catcher extends downstream above canyon 5, causing canyon 5 to have a slightly reduced flow. Canyon 3 and canyon 6 have flow patterns similar to those observed in the reference case (see Fig. 3.4). Fig. 3.12 also confirms that the cores of the vortices in canyon 4 and canyon 5 are located at around $z/H = 0.7$, as discussed in section 2.4. Flow reattachment occurs upstream of canyon 6, as the core of the vortex in canyon 6 is located near the mid canyon height (similar to canyon 3).
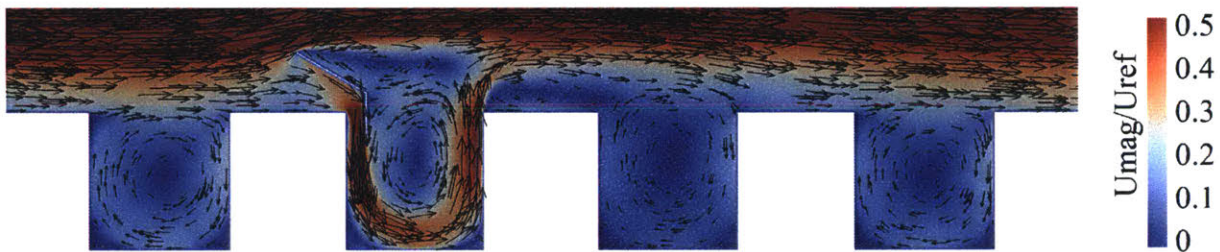
Fig. 3.12. Normalized velocity magnitude contours and vectors in canyons 3, 4, 5 and 6. The wind catcher channels atmospheric wind above the roof level into the target canyon 4, with little effects on other canyons.

3.5 Canyons with a Reversed Wind Catcher

Next, we validated the CFD model for the case with a reversed wind catcher. Fig. 3.13 shows that the CFD model predicted a flow reduction in canyon 5, as observed in the experiment. Since the flow in canyon 5 is the most distinctive in the case with a reversed wind catcher, Fig. 3.14 plots the velocity profiles in canyon 5 (instead of the target canyon 4). Similar to the previous cases, another simulation modeling a real-scale built environment was run. Fig. 3.14 shows that overall, the CFD model produced comparable results with the experiments, and the reduced-scale experiment is representative of a flow across full-scale canyons.
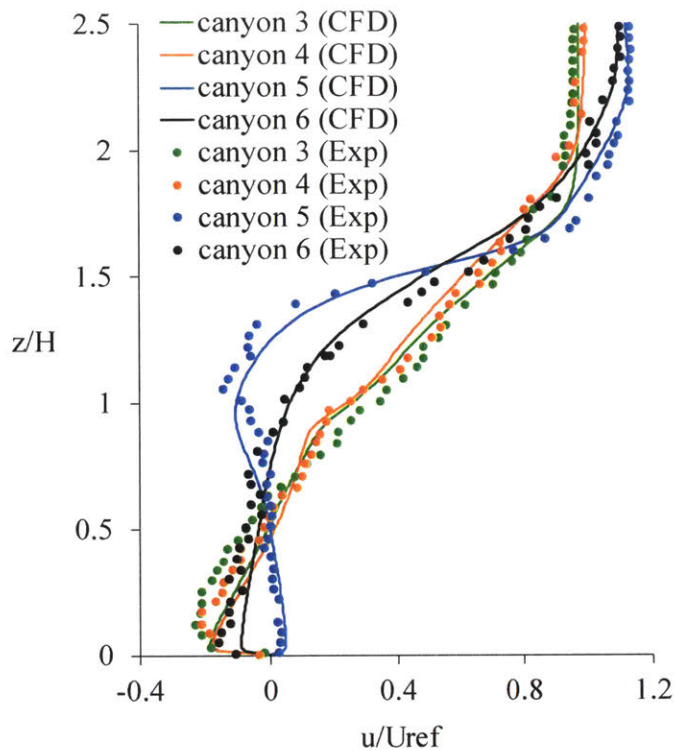
Fig. 3.13. CFD model validation with experiment for the case with a reversed wind catcher.

To visualize the flow field, Fig. 3.15 plots the middle-plane normalized velocity magnitude contours and vectors in canyons 3 to 6. The flow field in canyon 3 remains similar to the reference case, as expected. Although canyon 4 is the target canyon, the flow field in canyon 4 is not altered by the reversed wind catcher, except near the top right corner, where flow escapes through the "outlet" of the reversed wind catcher. The reversed wind catcher is installed near the windward wall so it has little effects on the velocity profiles at the middle line of the canyon. This explains the similarity between the velocity profiles of canyon 3 and canyon 4 measured in the experiment. The protrusion of the reversed wind catcher above the roof level induces a horizontally elongated separation bubble, which spans above canyon 5. This separation bubble inhibits atmospheric wind from flowing into canyon 5, causing canyon 5 to be quiescent. Further downstream at canyon 6, part of the atmospheric flow is able to enter canyon 6 but the velocity magnitude is lower compared to canyon 3.

Fig. 3.14. Normalized middle-line velocity profiles at canyons 5 comparing experimental and CFD results. (a) Mean stream-wise velocity, (b) mean vertical velocity, (c) stream-wise velocity fluctuation, and (d) vertical velocity fluctuation. "Exp scale" and "Full scale" are experimental scale and real scale in a built environment.
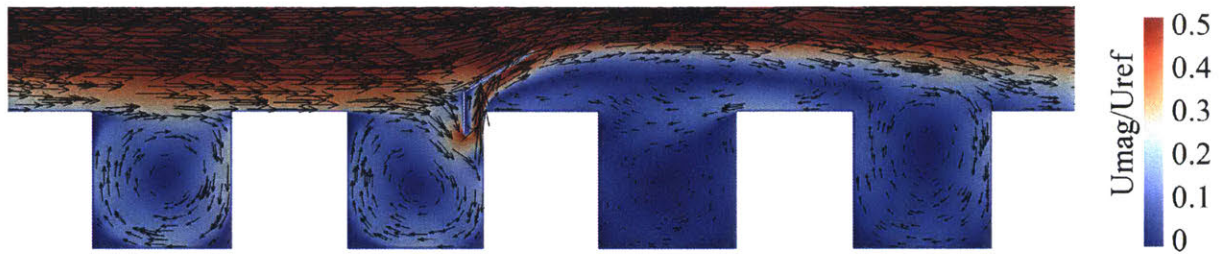
Fig. 3.15. Normalized velocity magnitude contours and vectors in canyons 3, 4, 5 and 6. The reversed wind catcher has little effect on the target canyon 4 except near the top right corner. The elongated separation bubble downstream of the reversed wind catcher inhibits flow into canyon 5.

3.6 Step-up and step-down canyons

For the case with a tall building 5, a step-up canyon 4 and a step-down canyon 5 are formed. Fig. 3.16 shows the comparison between experiment and CFD results for this case. The CFD model predicted almost zero flow in canyon 5, in good agreement with the experimental data.
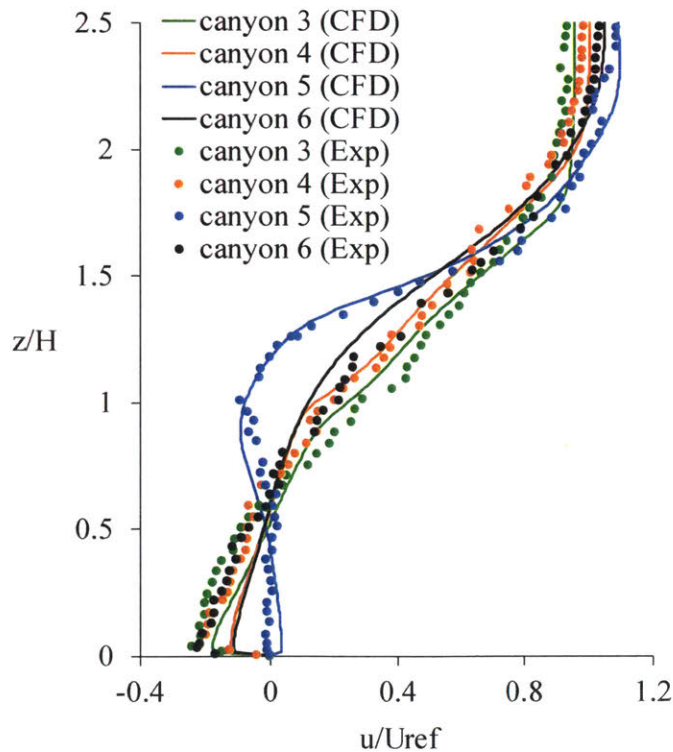
Fig. 3.16. CFD model validation with experiment for the case with step-up/step-down canyons.
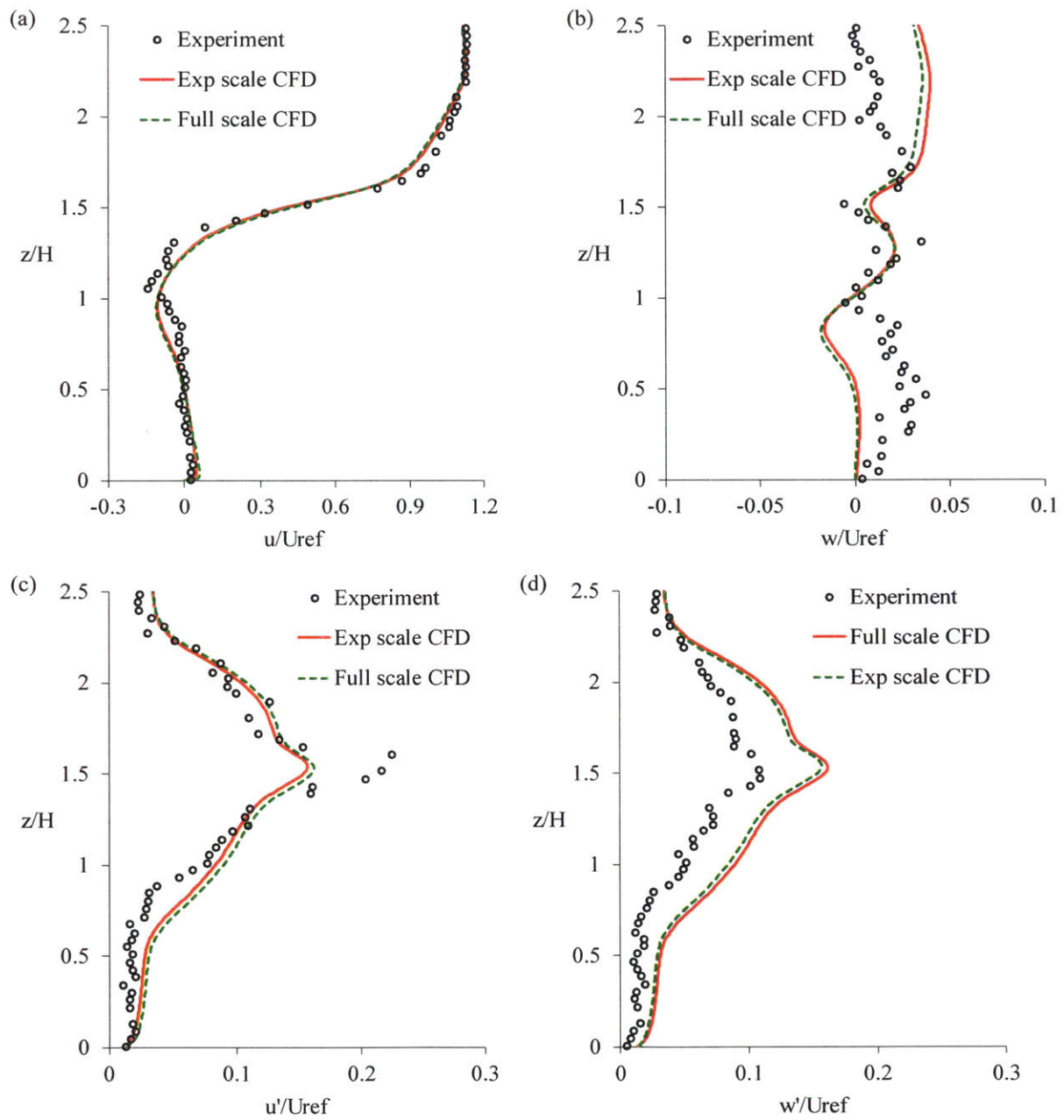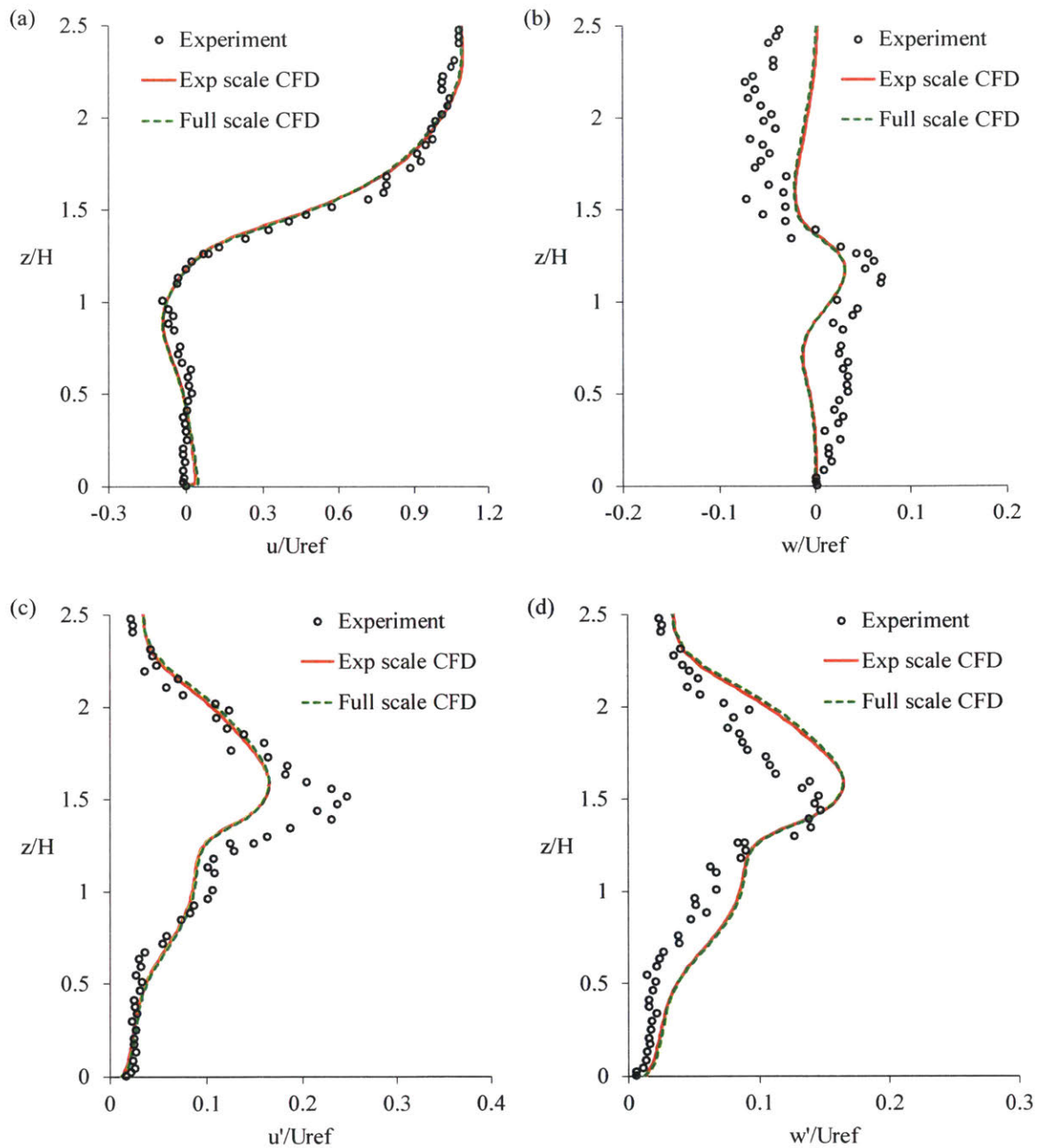
Fig. 3.17. Normalized middle-line velocity profiles at canyons 5 comparing experimental and CFD results. (a) Mean stream-wise velocity, (b) mean vertical velocity, (c) stream-wise velocity fluctuation, and (d) vertical velocity fluctuation. "Exp scale" and "Full scale" are experimental scale and real scale in a built environment.

Fig. 3.17 plots the velocity profiles in canyon 5 (not the target canyon 4). Similar to the previous cases, another simulation modelling a real-scale built environment is run. Fig. 3.17 shows that overall, the CFD model produced results comparable to the experiment, and the reduced-scale

experiment is representative of a flow across full-scale canyons in the case with step-up/step-down canyons.

To visualize the flow field, Fig. 3.18 plots the middle-plane normalized velocity magnitude contours and vectors of canyons 3 to 6. With a tall building 5, the flow fields in canyon 3, 4, and 6 remain relatively unchanged compared to the reference case (see Fig. 3.4). On the other hand, in canyon 5, which is a step-down canyon, there is almost no flow at the pedestrian level due to the blockage of upstream tall building 5. Comparing Fig. 3.18 with Fig. 3.15, a tall building exhibits blockage effects similarly to a reversed wind catcher.
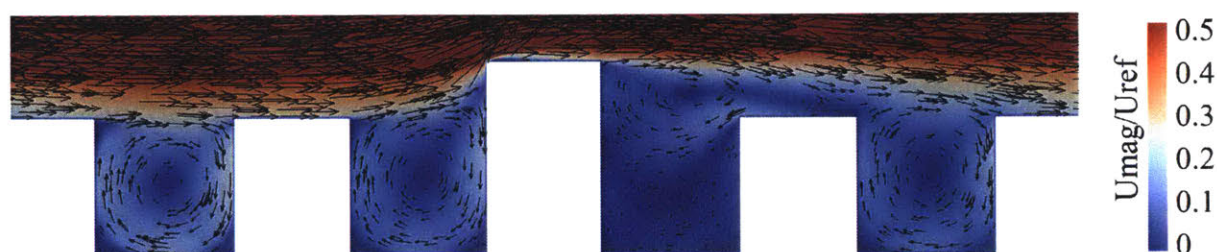
Fig. 3.18. Normalized velocity magnitude contours and vectors in canyons 3, 4, 5 and 6. The tall building reduces flow into canyon 5 but has little effects in other canyons.

To summarize this chapter, we conducted CFD simulations for all experimental cases in Table 2.1. The CFD models passed all validation tests and proved that reduced-scale experiments and reduced-scale CFD models (with Reynolds number in the orders of 10^4 to 10^5) can be used to study real-scale built environments, where the Reynolds number is much larger (in the orders of 10^6 to 10^7). Due to the limitation of probe accessibility, our experimental setup can only measure the middle-line velocity profiles. The validated CFD models complement the experiments by providing flow fields in the whole domain of interest. Furthermore, while we cannot extend the test section in the experimental setup due to space constraint, CFD domain can be extended easily. For instance, we added eight canyons in the CFD model with void decks to simulate flow across fifteen canyons. In a real-scale built environment, the extended CFD model shows that void decks have no effect on the flows in canyons located downstream of canyon 13.

Chapter 4 Numerical Simulations of 3D Canyons

In this chapter, we study urban wind flows across an idealized three-dimensional (3D) built environment. While some urban street canyons are two-dimensional (2D), many real world urban areas are 3D with finite building lengths and street intersections. For example, Fig. 4.1 shows a tall building in an atmospheric boundary layer flow exhibiting the "downwash" phenomenon, where a downward velocity is induced by the pressure difference in the vertical direction (Stathopoulos & Blocken, 2016). Section 4.1 validates the computational fluid dynamics (CFD) model with 3D canyons using wind tunnel experimental data in the literature. We then use the validated CFD model to study flows across reference 3D canyons, canyons with void decks, and canyons with a wind catcher in sections 4.2, 4.3, and 4.4, respectively. An improvised wind catcher is discussed in section 4.5, followed by results comparison of all the studied cases in section 4.6.
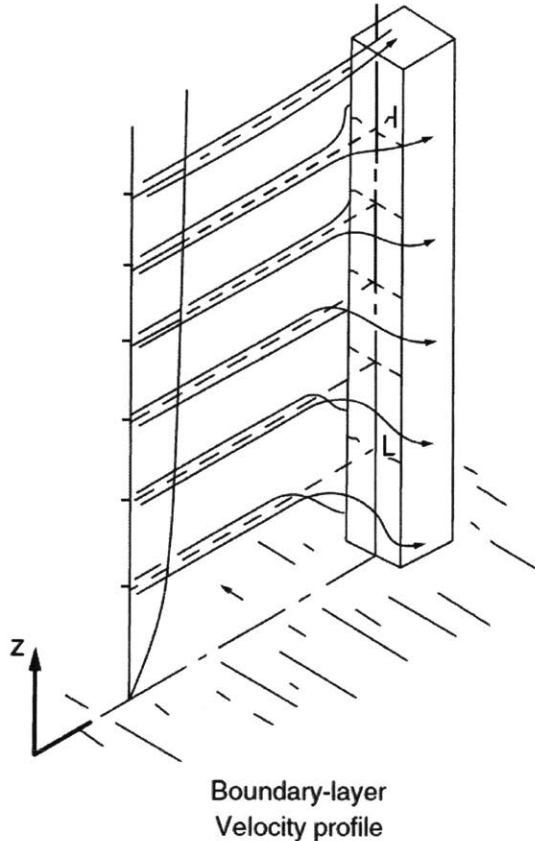

Boundary-layer
Velocity profile

Fig. 4.1. Boundary layer wind flow around a tall rectangular building, image from Stathopoulos & Blocken (2016).

57

4.1 CFD Model Validation

We first define the nomenclature convention for 3D canyons. Fig. 4.2 shows the top-view of an example space with two rows of four buildings and a street between the two rows of buildings. For a canyon, its width is defined as the distance between the two buildings forming the canyon, while its length is perpendicular to its width (in the same direction as the street width). Note that the "street width" should not be confused with the "building/canyon width." For a street, the convention is to define the length in the along-street axis (this makes sense as we walk along a street, we usually think the "street width" in terms of how wide the street is, for example, a two-lane wide street).
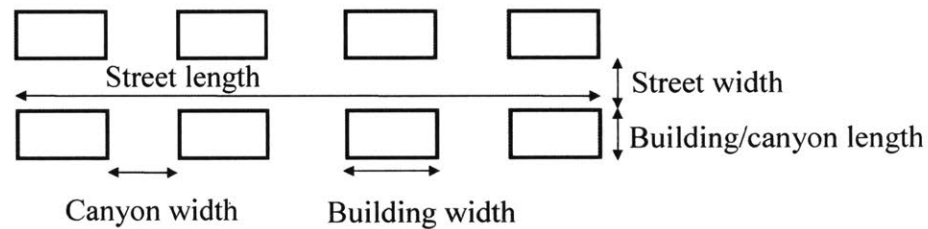
Fig. 4.2. Convention of nomenclature of 3D canyons with street intersections. The rectangular boxes represent buildings with canyons formed between the buildings and a street between the two rows of buildings.

Fig. 4.3 shows a CFD model of 3D canyons with a finite span-wise building length. The street length, the canyon width and the building width are in the stream-wise direction. The street width, the canyon length and the building length are in the span-wise direction. The along-street axis demarcates the center of the street between two arrays of buildings. Each building has a height H, where H = 12 m, width 10H/12, and length 5H/12. The canyon width is H so the canyon aspect ratio is 1. A periodic or symmetric boundary condition is applied at the span-wise boundaries. This means the array of canyons repeats itself in the span-wise direction and the street width is 5H/12. The inlet is 4H upstream of the first building with a prescribed velocity profile. The outlet 15H downstream of the last building has a zero-gradient boundary condition. The top boundary has a symmetric boundary condition. All walls including the bottom have a no-slip boundary condition. The steady solver "simpleFOAM" was used with the k-ε turbulence closure scheme for all simulations. The standard wall function was used to allow a coarser mesh.
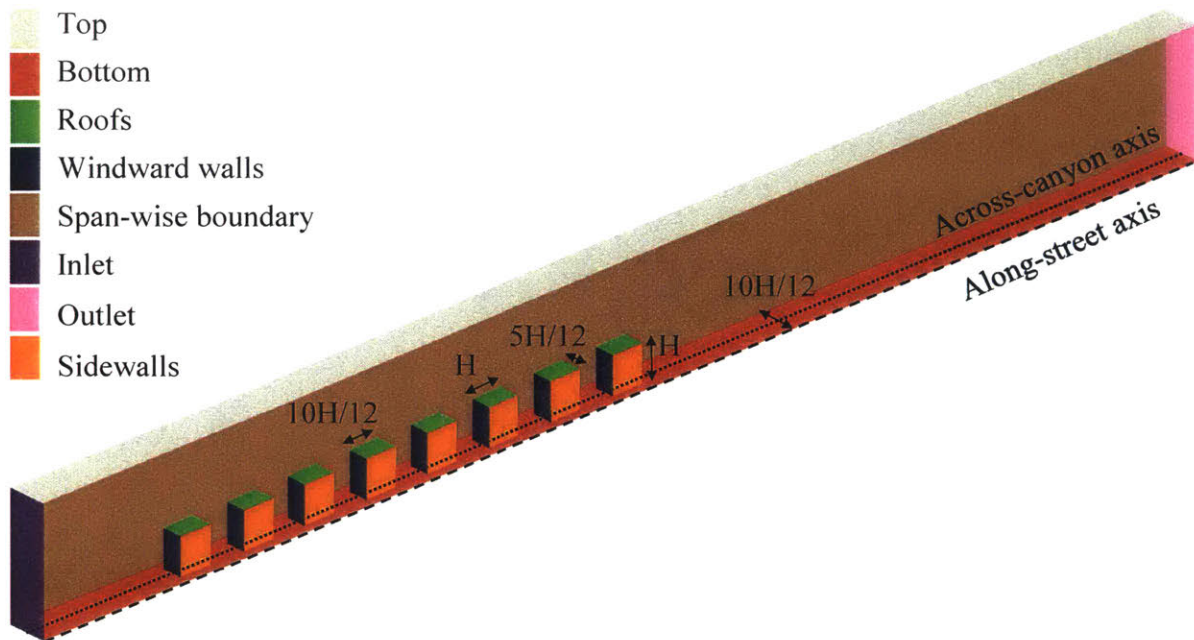
Fig. 4.3. 3D CFD model of seven canyons with aspect ratio 1. The dashed line is an axis along the street; the dotted line is an axis that cuts through the middle of all canyons.

We did not conduct experiments with 3D canyons in the water channel, so the CFD models in this chapter were validated with the wind tunnel experiment in Hang et al. (2012). The wind tunnel is 11 m long, 3 m wide and 1.5m tall. Fig. 4.4 shows the wind tunnel experimental setup with 9-row/12-column scaled-down buildings arranged perpendicular to the incoming flow. The arrangement has staggered building heights H1 and H2, alternating from H1 = 2B to H2 = 2.67B, where B = 30 mm is the building width. Both the canyon width and the canyon length equal B. In this case, since the canyons do not have a uniform height, B serves as a more suitable length scale instead of H1 or H2. The freestream velocity is 3.9 m/s. The Reynolds number in the experiment is about 16000 (based on a length scale of 2B). Velocity magnitude and turbulence kinetic energy were measured along both the horizontal (stream-wise) and vertical directions with hotwire anemometers. The vertical profiles in canyon 1 and canyon 6 (the locations indicated by V1 and V6 in Fig. 4.4(a)), as well as the horizontal profiles along the street (the x-axis in Fig. 4.4(a)) are reported in the paper.

59

a Building packing density $\lambda_p=0.25$
Street width W=Building width B

$H1=2B$ $H2=2.67B$

V8
V7
V6
V5
V4
V3
V2 $\updownarrow W=B$
V1 $W=B$ $B=30mm$

y Model description of Case [2-2.67, 9] in wind tunnel experiments
O Point O is (0,0)

b $W=B=30mm, H1=2B, H2=2.67B$ in Case [2-2.67, 9]

B B $W=B$ $H1$ $H2$ $W=B$

dH

$H_0=2.33B$

$W=B, \lambda_p=0.25, H1=2B, H2=2.67B$, standard deviation $\sigma_H=(H2-H1)/(H1+H2)=dH/H_0=14.3\%$
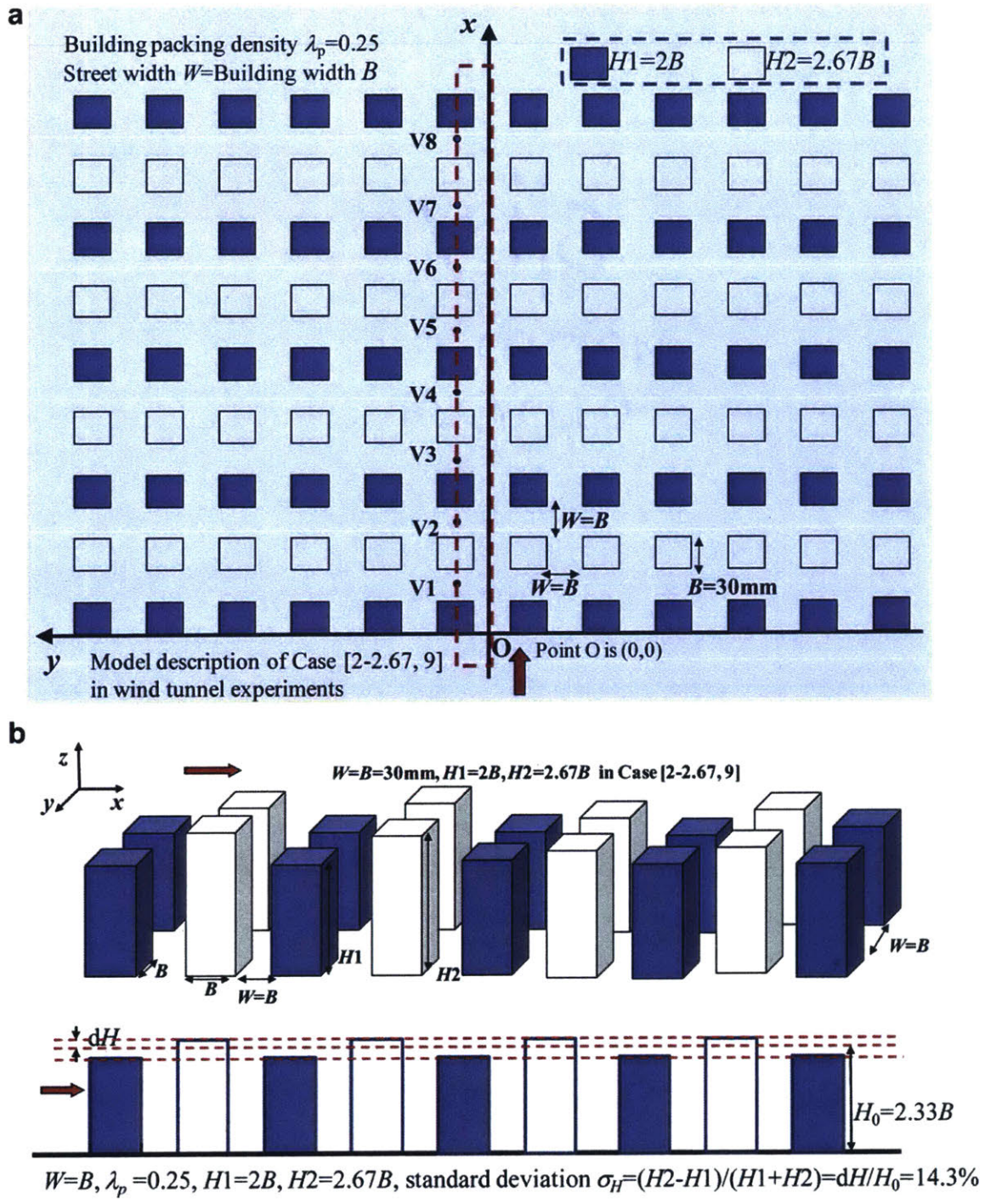
Fig. 4.4. (a) Top view of 9-row/12-column scale-down buildings arrangement in a wind tunnel experiment. (b) Isometric and side views showing two rows of buildings with staggered heights. Image from Hang et al. (2012).

We built a 3D CFD model with geometry that exactly matches the wind tunnel experiment, except we modeled only one column of buildings and applied a periodic boundary condition in the span-wise direction. In addition to the wind tunnel experiment, Hang et al. (2012) also conducted CFD simulations with the standard k-ε and the Re-Normalization Group (RNG) k-ε models. They concluded that the standard k-ε model is more accurate, in agreement with Xie, Huang, & Wang (2005). They modeled only half a column of buildings (the box in red dashed line in Fig. 4.4(a)) and applied a symmetric boundary condition in the span-wise direction. To directly compare our CFD results with theirs, we repeated our simulation with a symmetric span-wise boundary condition and obtained identical results with that of a periodic span-wise boundary condition, inferring that both the periodic and the symmetric boundary conditions are applicable in an idealized 3D canyon flow.

Fig. 4.5 shows the along-street horizontal profiles of velocity magnitude and turbulence kinetic energy at the height z/B = 1. The x-axis is normalized by the building width, B, and x/B = 0 corresponds to the first building (see Fig. 4.4(a)). Note that both the velocity magnitude (unit m/s) and turbulence kinetic energy (unit m^2/s^2) are not normalized. The wind tunnel experiment shows that along the street, the velocity magnitude increases sharply at x/B = 0. This is expected, as the upstream flow reaches the first building, it is squeezed between the first row of buildings with an increased speed. The maximum velocity is recorded near x/B = 0.5, then decreases consistently downstream along the street. At the last building (x/B = 17), the velocity is minimum. No experimental data is provided beyond the last building so it is not sure at what distance downstream the velocity magnitude recovers to the freestream value. For turbulence kinetic energy, k, upstream k is relatively constant at about 0.15 m^2/s^2 until x/B = 0. Between x/B = 0 and x/B = 3.5, k increases to about 0.3 m^2/s^2, then decreases slowly for x/B > 3.5. Comparing to the experimental results, both our CFD model and the CFD model in Hang et al. (2012) predicted the velocity magnitude profiles accurately. In terms of k, however, both models predicted the highest k near x/B = 0.5, which is the same location as the maximum velocity magnitude. Our CFD model performed better in this region by predicting a maximum k closer to the experimental value. Our model predicted a maximum k of about 0.4 m^2/s^2, while their model predicted a maximum k of about 0.7 m^2/s^2.
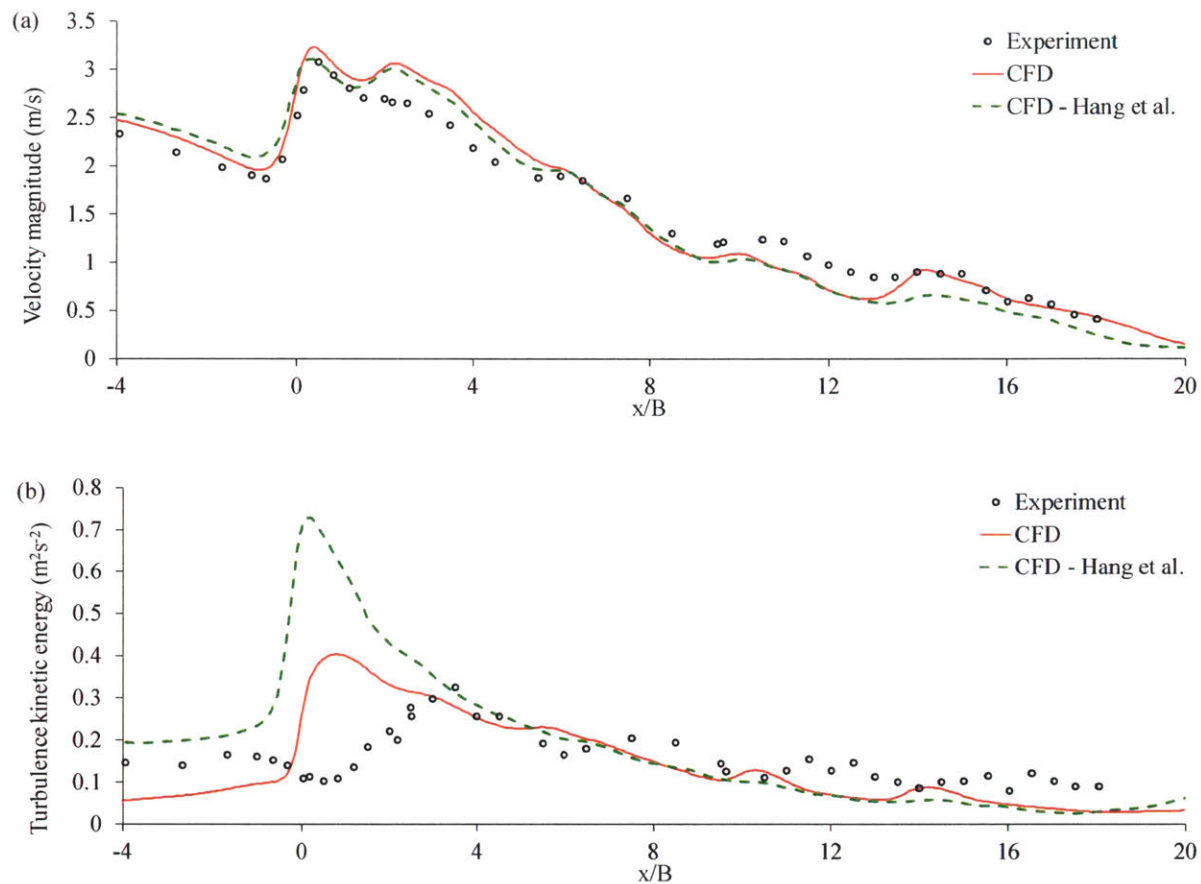
Fig. 4.5. Along-street horizontal profiles of (a) velocity magnitude and (b) turbulence kinetic energy. The x-axis is normalized by the building width, $B = 30$ mm, and $x/B = 0$ corresponds to the first building (see Fig. 4.4(a)). Solid lines are from our CFD model, both the experimental data and the dashed lines (CFD – Hang et al.) are from Hang et al. (2012).

Next, we plot in Fig. 4.6 the vertical profiles of velocity magnitude and turbulence kinetic energy at the middle lines of canyon 1 and canyon 6 (the locations indicated by V1 and V6 in Fig. 4.4(a)). In general, both our CFD model and the CFD model in Hang et al. (2012) predicted profiles matching the experimental data. Our CFD model has a slightly higher freestream velocity because we applied a different velocity profile at the inlet. In Hang et al. (2012), the inlet velocity profile is $U = 2.9 \times (z/B)^{0.1616}$ (unit m/s), whereas we used a built-in inlet boundary condition in OpenFOAM to be consistent with the inputs in our CFD models with 2D canyons in Chapter 3. This mismatch is unimportant after normalizing the whole velocity field with the freestream velocity. Both models predicted higher k in canyon 1, but our model correctly predicted the rapid decay of k to nearly zero near $z/B = 3$. Based on good agreement with experimental data in Fig. 4.5 and Fig. 4.6, our CFD model for 3D canyons is validated.

62
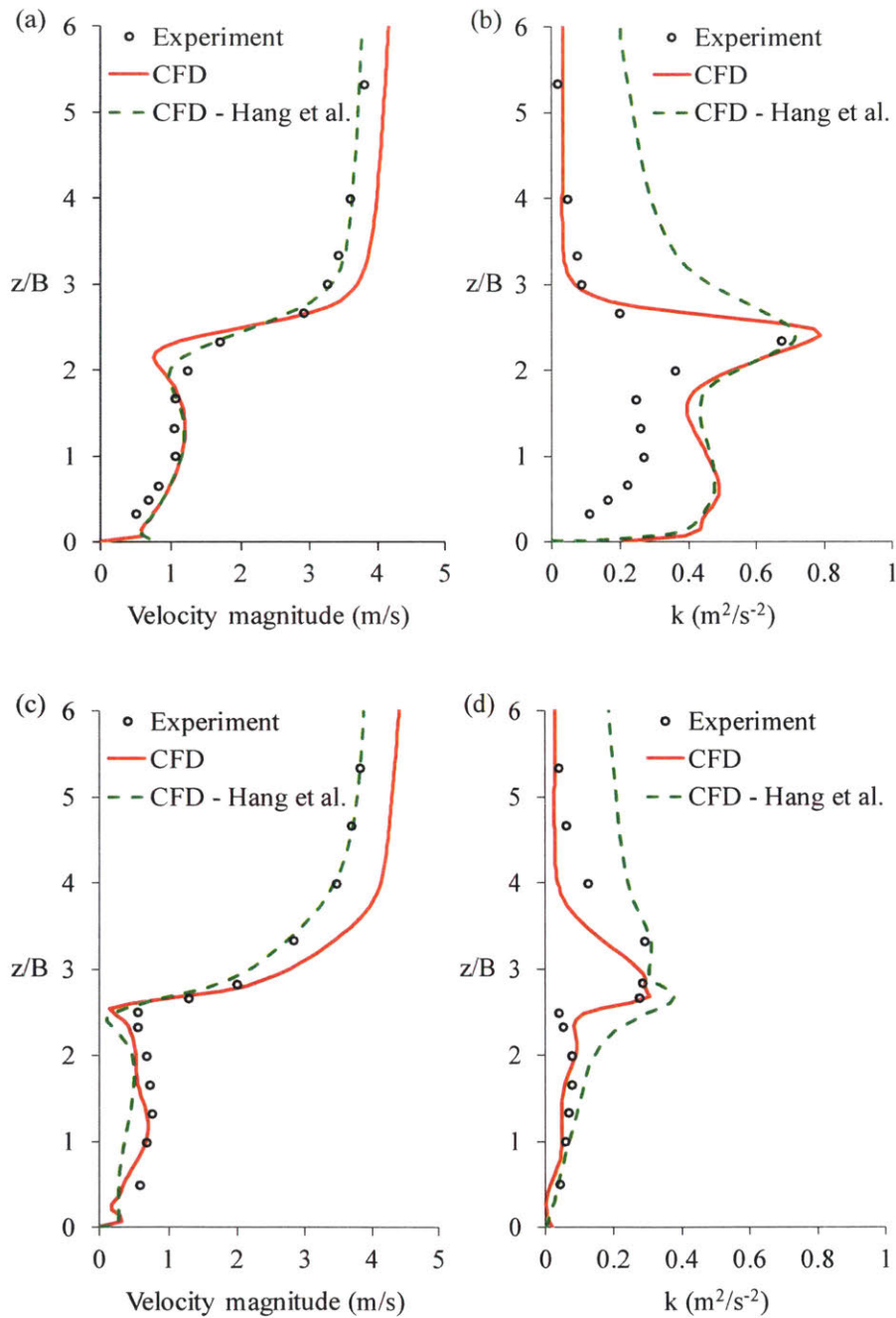
Fig. 4.6. Vertical profiles of (a) velocity magnitude at canyon 1, (b) turbulence kinetic energy at canyon 1, (c) velocity magnitude at canyon 6, and (d) turbulence kinetic energy at canyon 6. Solid lines are from our CFD model, both the experimental data and the dashed lines (CFD – Hang et al.) are from Hang et al. (2012).

We are now ready to use the validated CFD model to simulate flows across 3D canyons. Based on the extensive studies of different architectural interventions in 2D canyons, we concluded that a reversed wind catcher and a tall building are ineffective to enhance pedestrian-level wind

63

speed. Therefore, we only include the reference case, the case with void decks and the case with a wind catcher for subsequent simulations of 3D canyons. Furthermore, since we have demonstrated that CFD models at reduced-scale produce similar results to CFD models at full scale in Chapter 3, we only perform full-scale CFD simulations hereafter.

4.2 Reference Case with Canyons of Aspect Ratio 1

Since the flow fields in 3D canyons are very different from that of 2D canyons, we cannot use the reference case in section 3.2 as a benchmark for comparison. Therefore, we run a new reference case with 3D canyons of aspect ratio 1. The canyon height, $H = 12$ m, and the corresponding Reynolds number is 2.0×10^6. Fig. 4.7 shows the middle-line velocity profiles. All profiles are normalized by Uref, the freestream reference velocity. We plot the normalized turbulence kinetic energy, $k/(Uref)^2$, instead of u'/Uref and w'/Uref because we do not have experimental data to compare u'/Uref and w'/Uref as we did in the 2D cases. Although the span-wise velocity, v/Uref, may be significant especially near the sidewalls, we do not plot v/Uref, since it is zero at the middle plane due to symmetry (we apply a periodic/symmetric boundary condition in the span-wise direction). Fig. 4.7(a) shows that in all canyons, the normalized stream-wise velocity, u/Uref, is only about 10% of the freestream velocity. Unlike the velocity profiles in 2D canyons which show a varying u/Uref with z/H (see Fig. 3.3), u/Uref in a 3D canyon remains almost constant with z/H, and near-ground u/Uref is not significantly higher than other in-canyon regions. Fig. 4.7(b) shows that the vertical velocity, w/Uref, is small. At the near-ground level, maximum w/Uref is about 3% of the freestream velocity. For turbulence, Fig. 4.7(c) shows that the highest $k/(Uref)^2$ is observed at the roof level where z/H = 1. Above z/H = 1, $k/(Uref)^2$ decays linearly and approaches zero near z/H = 1.7. All canyons have about the same magnitude of maximum $k/(Uref)^2$ at the roof level. Inside the canyons (z/H < 1), $k/(Uref)^2$ decreases with downstream canyons: $k/(Uref)^2$ is the highest inside canyon 3 and the lowest inside canyon 6.

To visualize the flow field of the middle plane, Fig. 4.8 plots the normalized velocity magnitude (Umag/Uref) contours and vectors of canyons 3 to 6. Note the scale only ranges up to 0.5 (not 1.0) to highlight small velocity differences in the canyons. Regions with Umag/Uref > 0.5 have the same color as regions with Umag/Uref = 0.5. Flows inside these 3D canyons are relatively

weak, and there is no apparent circulation vortex like the reference case with 2D canyons. Higher velocity magnitude is observed near the windward walls, but this relatively high-speed downward flow does not a induce strong horizontal velocity at the near-ground level. This is because the flow can escape into the street (i.e. in the span-wise direction) upon reaching the near-ground level in a 3D canyon.
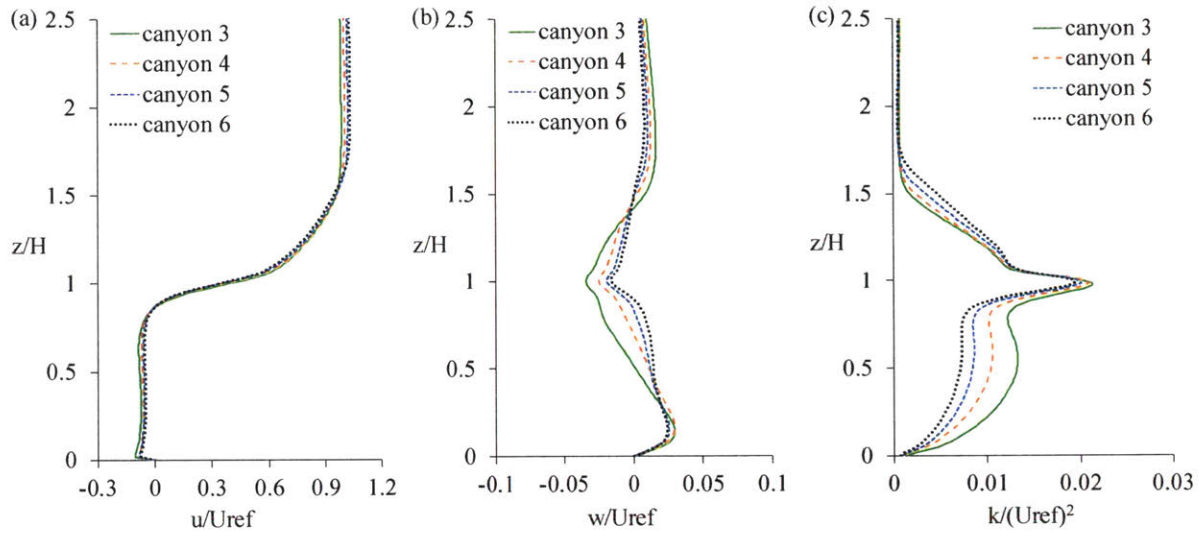
Fig. 4.7. Normalized velocity profiles in canyons 3, 4, 5, and 6. (a) Stream-wise velocity, (b) vertical velocity, and (c) turbulence kinetic energy.
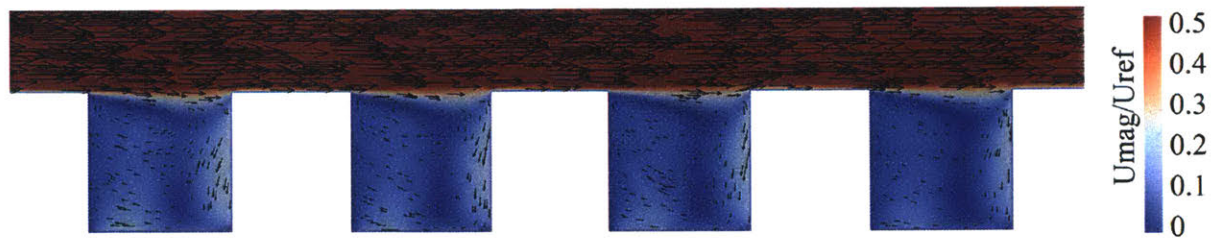
Fig. 4.8. Normalized velocity magnitude contours and vectors of canyon 3, 4, 5, and 6 for the reference case with 3D canyons.

4.3 Canyons with Void Decks

This section discusses the simulation results of 3D canyons with void decks. The geometry is the same as that of section 4.2, except all buildings have void decks of height H/6 below them. Fig. 4.9 plots the normalized profiles of u/Uref, w/Uref, and $k/(Uref)^2$. Overall, all canyons display higher near-ground velocities compared to the reference case, suggesting that the void decks

enhance near-ground wind speeds in 3D canyons. Canyon 3 has slightly higher u/Uref compared to the other canyons. Downstream canyons 4, 5, and 6 have the same magnitude of u/Uref at 20% of the freestream velocity, implying that the jets exiting the void decks maintain their momentum. Recall that in 2D canyons, the flow enhancement effect by void decks weakens with downstream canyons (see section 3.3). This weakening of the flow enhancement effect is not observed in 3D canyons with void decks. This could be due to the 3D nature of the canyons. Fig. 4.10(a) shows the middle-plane contours and vectors of the normalized velocity magnitude. Upon exiting a void deck, a jet reduces in speed, but "regenerates" some momentum before entering the next void deck. This momentum regeneration could be supplied by the high-speed flow along the street (see the along-street axis in Fig. 4.3) as shown in Fig. 4.10(b), which plots the contours of the plane that cut through the middle height of the void decks (section A-A). The along-street axis has no obstruction so the flow along the street can maintain its momentum downstream. Consistent feeding of momentum from the along-street flows explains why u/Uref in the canyons does not reduce in downstream canyons. Fig. 4.9(b) shows w/Uref remains relatively small compared to u/Uref near the ground level. For turbulence, the maximum $k/(Uref)^2$ is observed at the roof level at $z/H = 1$ as expected, and decays linearly with increasing height to zero near $z/H = 1.7$. Similar to the reference case, inside the canyons, canyon 3 has the largest $k/(Uref)^2$, while canyon 6 has the smallest $k/(Uref)^2$.

Fig. 4.9. Normalized velocity profiles in canyons 3, 4, 5, and 6 for 3D canyons with void decks. (a) Stream-wise velocity, (b) vertical velocity, and (c) turbulence kinetic energy.
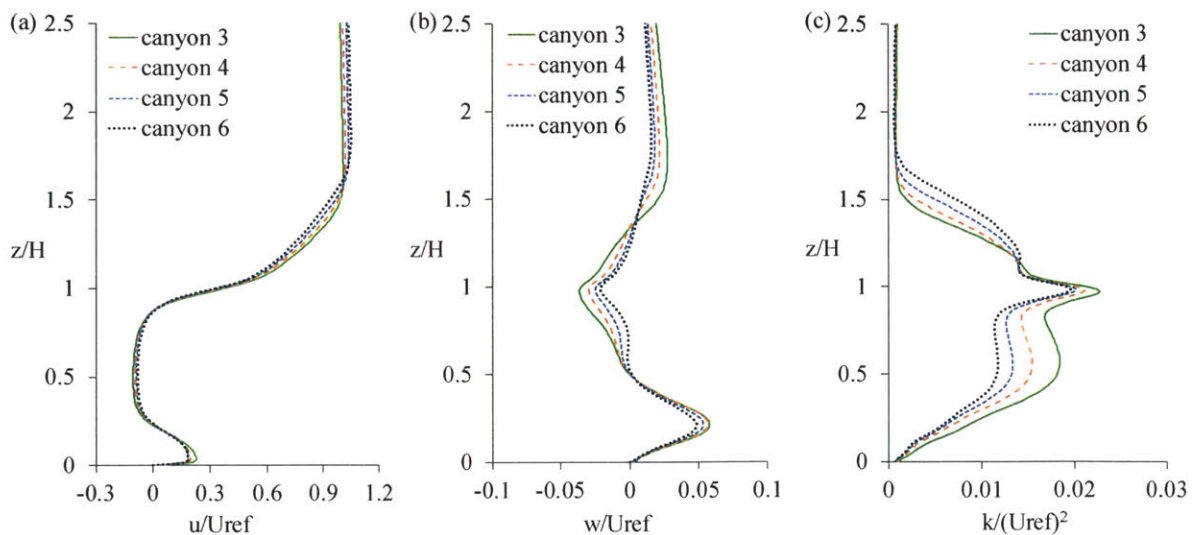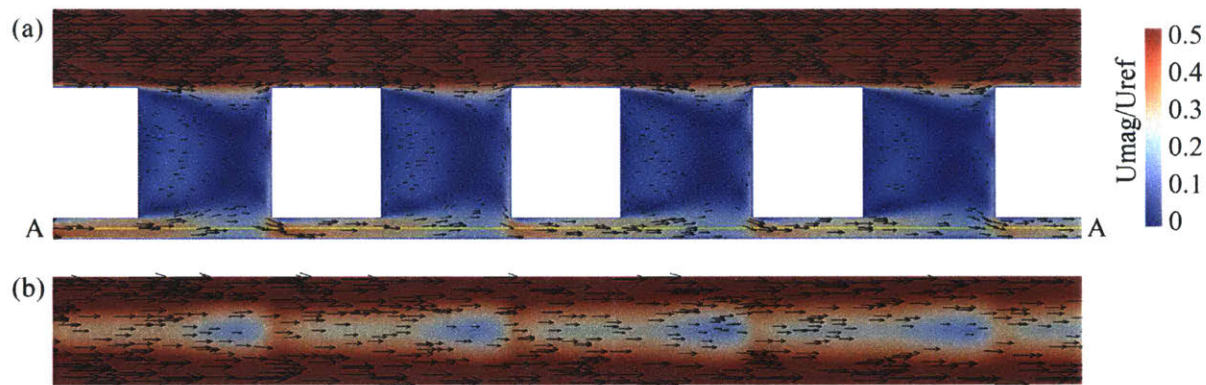
66

Fig. 4.10. Normalized velocity magnitude contours and vectors of canyon 3, 4, 5, and 6 for the case with void decks. (a) Side view of the middle plane that cuts across all canyons; (b) top view of section A-A plane that cuts through the middle height of the void decks.

4.4 Canyons with a Wind Catcher

This section discusses the simulation results of 3D canyons with a wind catcher above canyon 4. Fig. 4.11(a) shows that near the ground level, canyon 3 and canyon 5 have u/Uref about 10% of the freestream velocity, similar to the reference case. Canyon 6 has an unexpected reduction in u/Uref below $z/H = 0.6$. It is not clear what causes this reduction, but we suspect this could be due to a reduction of vertical velocity at the roof level of canyon 6. At the roof level ($z/H = 1$), canyon 5 has w/Uref about -0.06 (6% of the freestream velocity in the negative z direction), while canyon 6 has w/Uref about -0.02. Although this difference is small with respect to the freestream velocity magnitude (so small that it is not noticeable in Fig. 4.11(b)), a reduction in the downward velocity at the roof level may substantially reduce the near-ground velocity in a 3D canyon. This is observed in Fig. 4.12(a): the flow along the windward wall of canyon 6 is weaker than the flow along the windward wall of canyon 5. This means more air enters canyon 5 at the roof level than canyon 6, causing a lower wind speed at the pedestrian level in canyon 6. In canyon 4 with a wind catcher, the maximum near-ground u/Uref is about 15%, only 50% larger in magnitude than the reference case. This means that the wind catcher enhances near-ground wind speed in 3D canyons but is less effective compared to a wind catcher in 2D canyons (with 2.5 times near-ground wind speed enhancement). The profile of w/Uref in canyon 4 plotted in Fig. 4.11(b) may suggest a reason for this ineffectiveness. Below the roof level where z/H is between 0.5 and 1.0, there is a substantial w/Uref up to 0.3, larger than the magnitude of u/Uref at the same elevation. This vertical velocity

is in the positive z-direction, suggesting that upon exiting the outlet of the wind catcher, the flow turns upward at z/H near 0.75 instead of going downward to the ground level. This is observed in Fig. 4.12(a): the wind catcher captures high-speed atmospheric wind via its inlet, but the high-speed downward jet seems to lose its momentum before reaching the ground level. To understand what is happening between the leeward wall and the vertical plate of the wind catcher, we plot the velocity contours of section B-B in Fig. 4.12(b). Note that in Fig. 4.12(b), we plot the magnitude of span-wise velocity, v, and vertical velocity, w, (excluding the stream-wise velocity, u) to emphasize the span-wise flow. The magnitude of v and w are normalized with Uref. Right below the top plate of the wind catcher (the white line), part of the flow turns around the side edges of the plate. The flow near the side edges of the plate then either flows upward or turns around further to hit the top surface of the plate. This flow pattern is induced by the pressure difference across the top plate of the wind catcher. Fig. 4.12(c) plots the pressure coefficient, C_p, $= P/0.5\rho(Uref)^2$, where P is the (gauge) pressure and ρ is the fluid density. The top surface of the plate has a low pressure due to flow separation, while the bottom surface has a high pressure due to impinging high-speed flow captured at the inlet. This pressure difference drives the span-wise leakage, analogous to an induced vortex at the wingtip of an airfoil or aircraft wing. Modern aircrafts have winglets to reduce wingtip vortices. Inspired by the idea of winglets to reduce span-wise leakage, we improve the effectiveness of a wind catcher in 3D canyons in the next section.

For turbulence, Fig. 4.11(c) shows that $k/(Uref)^2$ profile of canyon 3 has a peak of about 0.02 at z/H = 1, and decays to zero near z/H = 1.7, similar to the reference case. Canyon 4 has a much higher $k/(Uref)^2$ peak of 0.07, also at z/H = 1. This is surprising, as we expected the highest turbulence at the protrusion height of the wind catcher around z/H = 1.5. The contours plot in Fig. 4.12(a) explains this by showing that the highest shear occurs at z/H = 1 where the freestream flow meets the low-speed flow in the canyon. Fig. 4.12(a) also reveals that the separation bubble induced by the wake of the wind catcher is much smaller in this case with 3D canyons than in the case with 2D canyons (see Fig. 3.12). The peak of $k/(Uref)^2$ decays rapidly to about 0.03 downstream at canyon 5. Between z/H = 1 and z/H = 1.5, $k/(Uref)^2$ remains relatively constant at the peak value and decays to zero at z/H = 1.9. Canyon 6 has a smaller peak and zero $k/(Uref)^2$ is observed above z/H = 2.
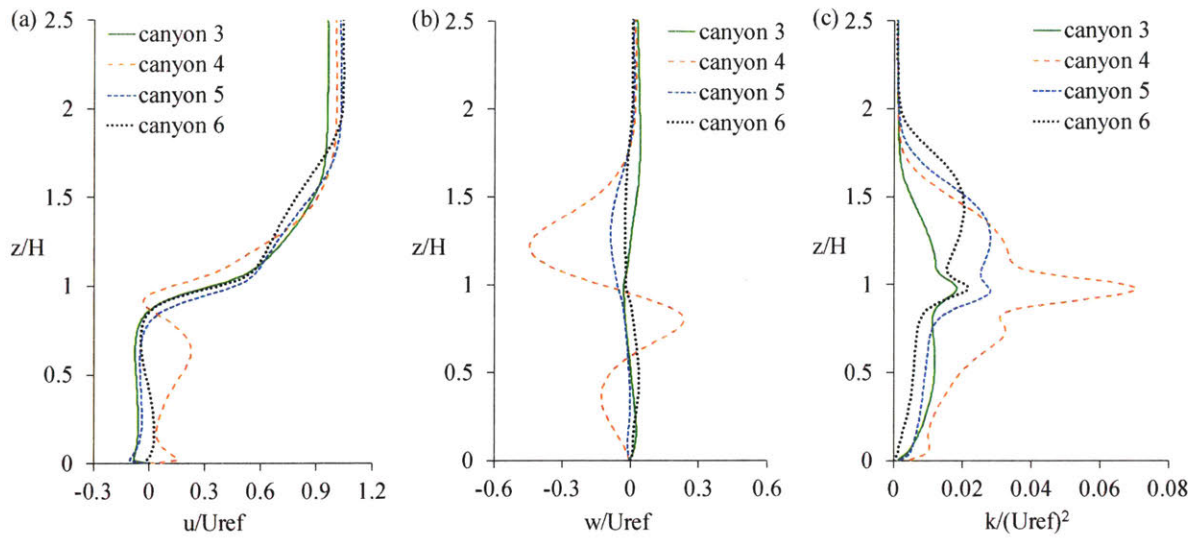
Fig. 4.11. Normalized velocity profiles in canyons 3, 4, 5, and 6 for 3D canyons with a wind catcher. (a) Stream-wise velocity, (b) vertical velocity, and (c) turbulence kinetic energy.
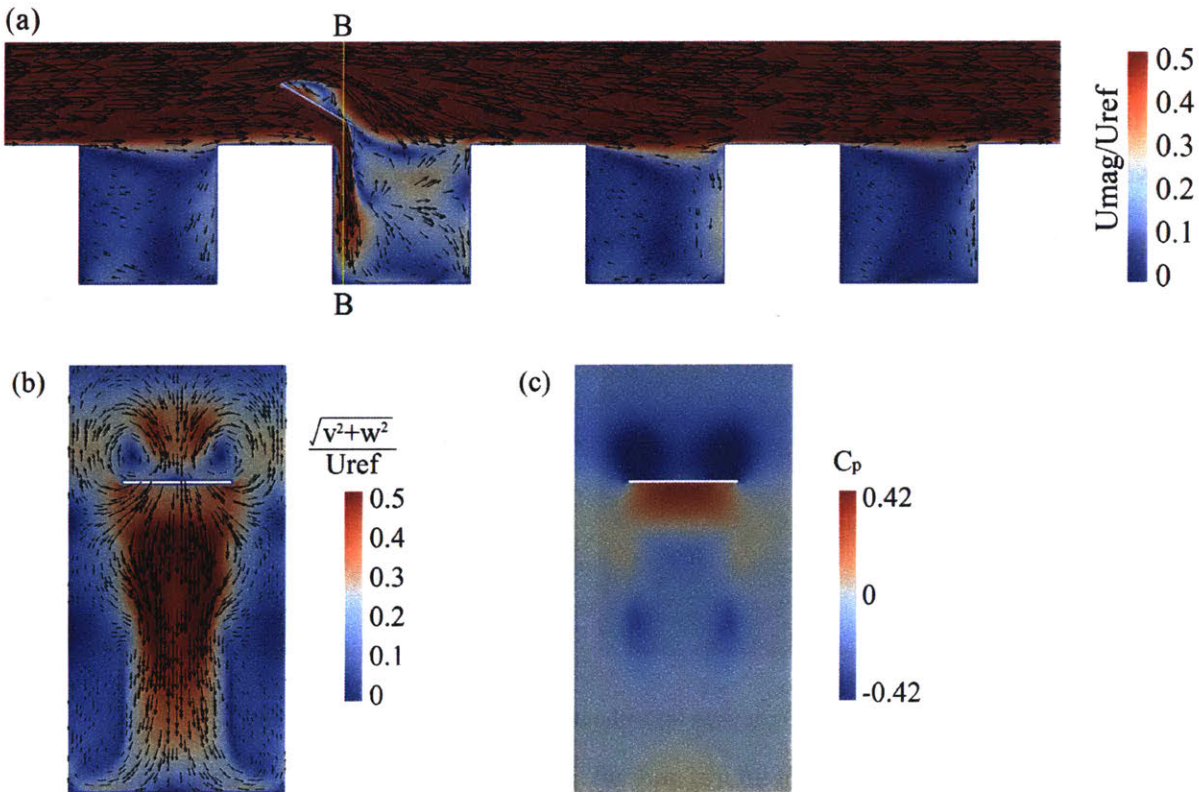
Fig. 4.12. Normalized velocity magnitude contours and vectors for the case of a wind catcher in 3D canyons. (a) Side view of the middle plane that cuts across canyons 3, 4, 5, and 6; (b) normalized span-wise and vertical velocity contours and vectors of section B-B; and (c) pressure coefficient contours of section B-B.

4.5 Wind Catcher with Sidewalls

Section 4.4 suggest that a wind catcher in 3D canyons (Fig. 4.13(a)) has a low effectiveness due to span-wise flow leakage. Inspired by how winglets weaken wingtip vortices on airfoils, we attempt to reduce span-wise leakage by adding "winglets" to our wind catcher. This section presents the simulation results of a wind catcher with sidewalls (Fig. 4.13(b)) to prevent span-wise leakage of the captured wind. Note that the sidewalls are added only above the roof level. Fig. 4.14 summarizes the profiles of $u/Uref$, $w/Uref$, and $k/(Uref)^2$. Near-ground $u/Uref$ is about 30% of the freestream flow in the target canyon 4. Recall that near-ground $u/Uref$ in the case of a wind catcher without sidewall is about 15% of the freestream velocity, so the sidewalls double the effectiveness of the wind catcher. There is still a significant $u/Uref$ at $z/H = 0.75$, meaning that a portion of the flow exiting the wind catcher leaks through the roof level before reaching the ground. The $w/Uref$ profile in canyon 4 confirms this leakage, since $w/Uref$ is large (up to 30% of the freestream velocity) at the roof level. Further improvement could be made by adding sidewalls below the roof level and placing the outlet at a lower elevation (i.e. by having a longer vertical plate). Nonetheless, both these approaches may not be feasible on a real building, as occupants of the top floors may not welcome them due to blocked views or not being aesthetically appealing.
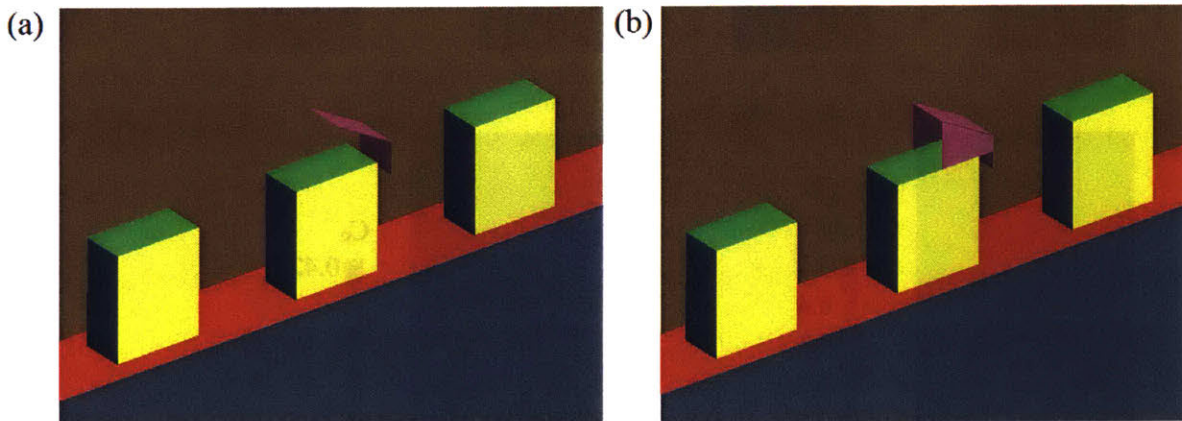
Fig. 4.13. Model of a wind catcher in 3D canyons (a) without sidewall and (b) with sidewalls.

In canyons 3, 5, and 6, both $u/Uref$ and $w/Uref$ remain small. A smaller near-ground $u/Uref$ is observed in canyon 6, possibly due to the same reason discussed in section 4.4. At the roof level, $w/Uref$ is -0.05 in canyon 5 and -0.015 in canyon 6. For $k/(Uref)^2$, canyon 3, which is upstream of the wind catcher, has the highest $k/(Uref)^2$ at the roof level. In canyon 4, the highest $k/(Uref)^2$ is

predicted at z/H about 1.5, which is the height of the protrusion of the wind catcher. Fig. 4.15(a) reveals that the highest shear occurs at this elevation. Recall that for a wind catcher without sidewalls in 3D canyons, the highest $k/(U_{ref})^2$ is predicated at z/H = 1. This means that the sidewalls also affect the size of the separation bubble induced by the wake of the wind catcher. Downstream canyon 5 and canyon 6 have the highest $k/(U_{ref})^2$ near z/H = 1.5, too.

Fig. 4.15(a) plots the normalized velocity magnitude contours and vectors of canyons 3, 4, 5, and 6 with the scale ranges from 0 to 0.5. Overall, canyon 3 and canyon 5 have almost identical flow fields, while canyon 6 has lower velocity magnitude. In canyon 4, we observe an upward flow near the roof level, supporting the inference that a portion of the flow exiting the wind catcher leaks through the roof level. To visualize the flow field between the leeward wall of canyon 4 and the wind catcher, Fig. 4.15(b) plots the normalized velocity magnitude contours and vectors of v and w (excluding u) of the vertical plane B-B. Compared to Fig. 4.12(b), the wind catcher with sidewalls prevents flow leakage in the span-wise direction, although there is a substantial pressure difference across the top plate of the wind catcher (Fig. 4.15(c)). The high-speed jet travels downward with little momentum loss to the span-wise direction until it reaches the ground. It then turns into both the span-wise and the stream-wise directions. The flow that turns into the stream-wise direction is observed as the near-ground horizontal jet in Fig. 4.15(a).
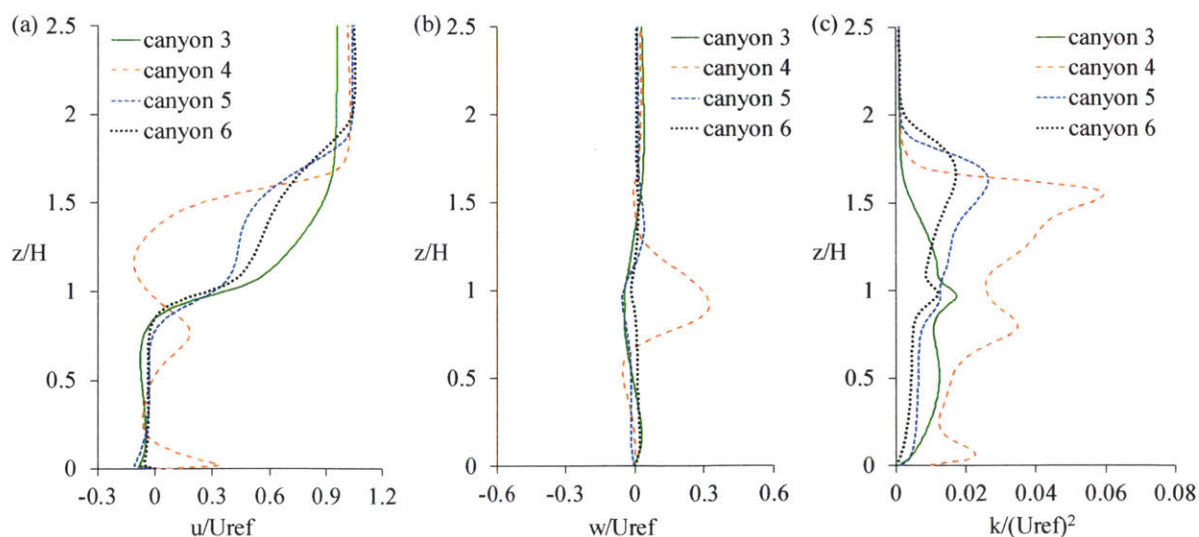

Fig. 4.14. Normalized velocity profiles in canyons 3, 4, 5, and 6 for 3D canyons with a wind catcher with sidewalls. (a) Stream-wise velocity, (b) vertical velocity, and (c) turbulence kinetic energy.

71
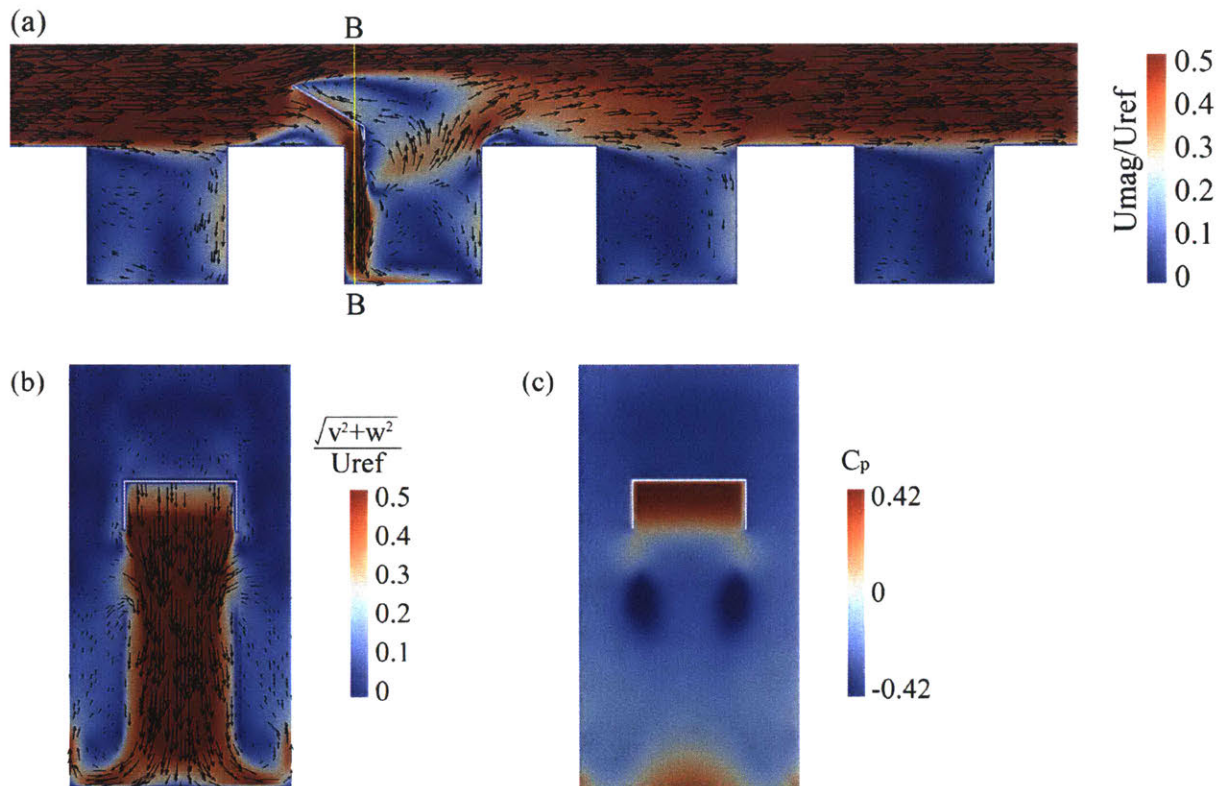
Fig. 4.15. Normalized velocity magnitude contours and vectors for the case of a wind catcher with sidewalls. (a) Side view of the middle plane that cuts across canyons 3, 4, 5, and 6; (b) normalized span-wise and vertical velocity contours and vectors of section B-B; and (c) pressure coefficient contours of section B-B.

4.6 Results Comparison for 3D Canyons

To summarize Chapter 4, we have conducted four full-scale simulations of 3D canyons: the reference case with canyons of aspect ratio 1, canyons with void decks, canyons with a wind catcher, and canyons with a wind catcher with sidewalls. Fig. 4.16 plots the normalized stream-wise velocity magnitude comparing all four cases in each canyon. In canyon 3, Fig. 4.16(a) shows that the void deck enhances near-ground flow by more than two times, while both cases of wind catcher have slightly reduced flows. In canyon 4, the wind catcher with sidewalls perform the best by tripling the near-ground flow, while the wind catcher without sidewalls enhances near-ground flow by only 50%. Flow enhancement of the void decks maintains at two times in canyons 4, 5, and 6. In canyon 5, both cases of wind catcher have little difference compared to the reference case. In canyon 6, flow reduction is observed for both cases of wind catcher. In conclusion, the

wind catcher with sidewalls is the most effective architectural intervention to enhance near-ground wind speed in a single 3D canyon, but it reduces the wind speed in downstream canyons. The void deck benefits all canyons by consistently doubling near-ground wind speeds in all canyons.
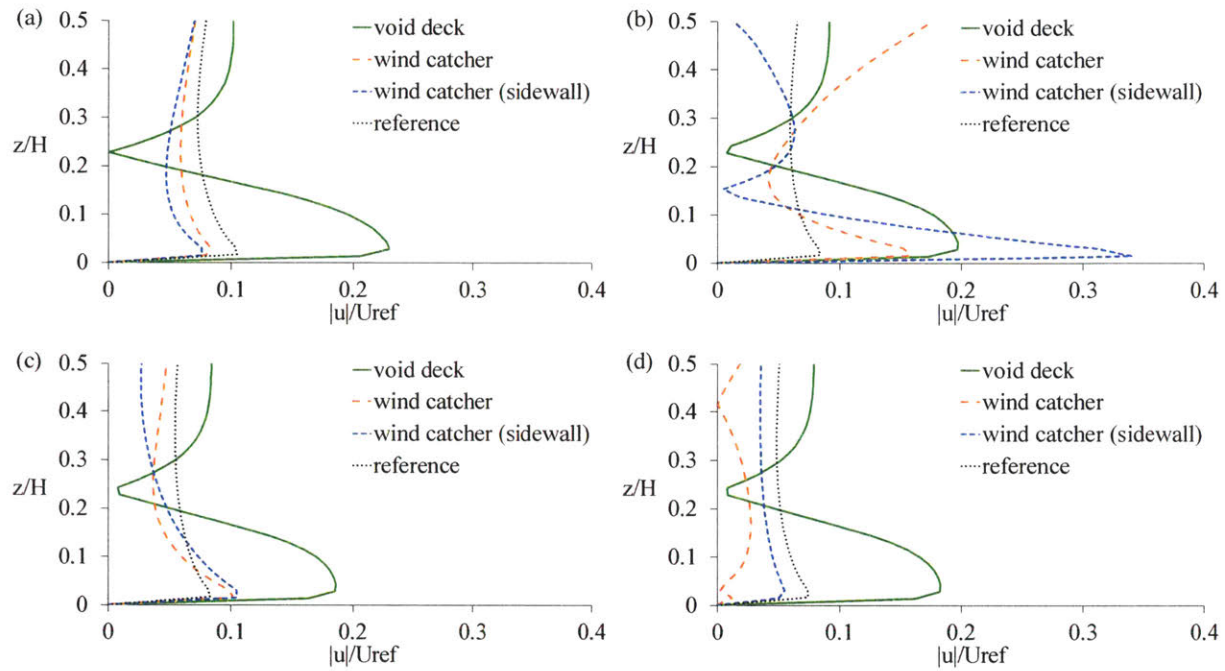

Fig. 4.16. Comparison of normalized stream-wise velocity magnitude between the reference case, the case with void decks, the case with a wind catcher, and the case with a wind catcher with sidewalls in (a) canyon 3, (b) canyon 4, (c) canyon 5, and (d) canyon 6.

Chapter 5 Conclusion and Future Work

Pedestrian-level wind flow plays an important role in outdoor thermal comfort. In an urban area with a high density of buildings, pedestrian-level wind speed is often much lower than the atmospheric wind due to the blockage effects of buildings. This thesis focuses on tropical climates where stronger winds help to improve outdoor thermal comfort by increasing the convective heat transfer from pedestrians to the surrounding air. We aim to enhance pedestrian-level wind speed in urban street canyons, while holding constant the other parameters contributing to thermal comfort (air temperature, radiant temperature, humidity, metabolic rate, and clothing insulation). Passive wind enhancement designs are favorable, as they require no energy input. We proposed four types of passive architectural interventions to enhance wind speed, namely the void decks, the wind catcher, the reversed wind catcher, and the step-up/step-down canyons. We adopted both experimental and numerical simulation approaches to evaluate the effectiveness of these architectural interventions in terms of near-ground flow speed.

For the experimental approach, we arranged an array of scaled-down models of buildings in a recirculating water channel to simulate wind flow across an array of seven 2D canyons. The velocity profiles at the middle lines of the third to sixth canyons (canyons 3, 4, 5, and 6) were measured with Acoustic Doppler Velocimetry. Five sets of readings were recorded, one for the reference case with evenly spaced canyons of aspect ratio 1, and one each for the four types of proposed architectural interventions. In the reference case, canyons 3, 4, 5, and 6 have similar velocity profiles, with near-ground flow (analogous to pedestrian-level wind speed) about 20% of the freestream velocity (analogous to the atmospheric wind speed above the roof level). By introducing the void decks, we boost near-ground flow to about 50%, 40%, 30%, and 25% of the freestream velocity in canyons 3, 4, 5, and 6, respectively. The wind catcher (above canyon 4) increases near-ground flow in canyon 4 to about 55% of the freestream velocity, while the flows in other canyons are not significantly altered. The reversed wind catcher (above canyon 4), however, reduces the near-ground flow in canyon 5 to almost zero, while the flows in other canyons are not significantly altered. A tall building downwind of canyon 4 produces about the same flow pattern as the case of a reversed wind catcher, with nearly zero flow in canyon 5. Overall, the void decks are effective in channeling stronger near-ground flow into multiple canyons, but the flow enhancement effect diminishes at downstream canyons. The wind catcher most effectively

boosts near-ground flow in a single canyon. The reversed wind catcher and the step-up/step-down canyons have adverse effects in terms of flow enhancement.

Next, we conducted numerical simulations of the five cases with computational fluid dynamics (CFD) models. The simulations results agree well with the experiments in all five cases, validating all our CFD models. The validated CFD models were used to plot the flow field contours to complement the lack of flow visualization in the experiments. These flow fields provide insights to the physics of the flow, such as the number and sizes of circulation vortices. Simulations were then repeated with wind flows across full-scale built environments. The simulation results at full scale match the simulation results at experimental scale, justifying that the reduced-scale experiments are representative of full-scale built environments (with canyons of aspect ratio 1). We also extended the domain of the CFD model with void decks, and concluded that the effect of the void decks becomes insignificant downstream of canyon 13 (at the full scale). Based on both experimental and numerical results, we recommend the void decks for pedestrian-level wind speed enhancement in an array of 2D canyons. For wind speed enhancement in a single 2D canyon, the wind catcher is the most effective architectural intervention. Nevertheless, in an unfavorable wind direction (reversed wind direction), the wind catcher reduces the flow in the immediate downstream canyon. To overcome this, we can make the top plate of the wind catcher rotatable to change the orientation of the inlet.

The flow behavior in 3D canyons is very different from that of 2D canyons. For the reference case with 3D canyons, we validated our CFD models with wind tunnel experiments published in the literature. Due to the finite widths of buildings, which allows air to be channeled in stream-wise streets, near-ground flow speed in the span-wise canyons is smaller than 10% of the freestream velocity. The void decks boost near-ground flow to about 20% of the freestream velocity in all canyons. The diminishing flow enhancement at downstream canyons observed in 2D canyons is not observed in 3D canyons. The wind catcher increases near-ground flow to about 15% of the freestream velocity. The low effectiveness of the wind catcher in 3D canyons is due to flow leakage through the sides. By closing the sides, a wind catcher with sidewalls outperforms the void decks, boosting near-ground flow to about 30% of the freestream velocity. Similar to 2D canyons, we recommend the void decks as a passive means to enhance pedestrian-level wind speed

in an array of 3D canyons, whereas for a single 3D canyon, we recommend installing the wind catcher with sidewalls.

Our work shows that the void decks and the wind catchers are the two types of passive architectural interventions that are effective to enhance pedestrian-level wind speed. We recognize opportunities to optimize both interventions that are not within the scope of this thesis. For future work, parametric studies of the geometry of the void decks and the wind catchers can be conducted. For example, the shape of the wind catcher induces a sudden change of flow direction from the stream-wise direction to the vertical direction. A rounded corner or internal guide vanes may reduce pressure loss due to sudden turning. Another suggestion for future work is to combine the strengths of both: using wind catchers to reenergize near-ground flow when the flow weakens in the downstream canyons with the void decks. Our studies reveal that the flow enhancement effect of the void decks diminishes at canyon 6 in an array of 2D canyons. A wind catcher can be installed above canyon 6 to channel atmospheric flow into it. The high-speed jet induced by the wind catcher will travel downstream through the void decks, enhancing near-ground flow in the downstream canyons. In addition, this thesis looks only at the aspect of wind speed. For future work, the models can be extended to solve for the energy equation and the passive scalar transport equation to study the temperature fields and pollutant dispersion with these proposed architectural interventions.

References

Aliabadi, A. A., Krayenhoff, E. S., Nazarian, N., Chew, L. W., Armstrong, P. R., Afshari, A., & Norford, L. K. (2017). Effects of Roof-Edge Roughness on Air Temperature and Pollutant Concentration in Urban Canyons. *Boundary-Layer Meteorology*, 1–31.

ANSYS. (2017). ANSYS, Inc. Retrieved from http://www.ansys.com/

Assimakopoulos, V., ApSimon, H., & Moussiopoulos, N. (2003). A numerical study of atmospheric pollutant dispersion in different two-dimensional street canyon configurations. *Atmospheric Environment*, *37*(29), 4037–4049.

Baik, J.-J., & Kim, J.-J. (1999). A numerical study of flow and pollutant dispersion characteristics in urban street canyons. *Journal of Applied Meteorology*, *38*(11), 1576–1589.

Baik, J.-J., Park, R.-S., Chun, H.-Y., & Kim, J.-J. (2000). A laboratory model of urban street-canyon flows. *Journal of Applied Meteorology*, *39*(9), 1592–1600.

Brown, M. J., Lawson, R. E., DeCroix, D. S., & Lee, R. L. (2000). Mean flow and turbulence measurements around a 2-D array of buildings in a wind tunnel. In *11th joint AMS/AWMA conference on the applications of air pollution meteorology. Long Beach, CA*.

Brown, M. J., Lawson, R. E., DeCroix, D. S., & Lee, R. L. (2001). Comparison of centerline velocity measurements obtained around 2D and 3D building arrays in a wind tunnel. *Int. Soc. Environ. Hydraulics, Tempe, AZ*.

Cairns, S., Jacobs, J. M., Yingying, J., Padawangi, R., Siddique, S., & Tan, E. (2014). Singapore's Void Decks.

de Dear, R., & Kim, J. (2016). Thermal Comfort Inside and Outside Buildings. In *Advanced Environmental Wind Engineering* (pp. 89–99). Springer.

de Dear, R., & Spagnolo, J. (2005). Thermal comfort in outdoor and semi-outdoor environments. *Elsevier Ergonomics Book Series*, *3*, 269–276.

Djongyang, N., Tchinda, R., & Njomo, D. (2010). Thermal comfort: A review paper. *Renewable and Sustainable Energy Reviews*, *14*(9), 2626–2640.

Esfeh, M. K., Dehghan, A., Manshadi, M. D., & Mohagheghian, S. (2012). Visualized flow structure around and inside of one-sided wind-catchers. *Energy and Buildings*, *55*, 545–552.

Franke, J., Hirsch, C., Jensen, A., Krüs, H., Schatzmann, M., Westbury, P., ... Wright, N. (2004). Recommendations on the use of CFD in wind engineering. In *Cost action C* (Vol. 14, p. C1).

Geros, V., Santamouris, M., Karatasou, S., Tsangrassoulis, A., & Papanikolaou, N. (2005). On the cooling potential of night ventilation techniques in the urban environment. *Energy and Buildings*, *37*(3), 243–257.

Hang, J., Li, Y., & Sandberg, M. (2011). Experimental and numerical studies of flows through and within high-rise building arrays and their link to ventilation strategy. *Journal of Wind Engineering and Industrial Aerodynamics*, *99*(10), 1036–1055.

Hang, J., Li, Y., Sandberg, M., Buccolieri, R., & Di Sabatino, S. (2012). The influence of building height variability on pollutant dispersion and pedestrian ventilation in idealized high-rise urban areas. *Building and Environment*, *56*, 346–360.

Huang, Y., Hu, X., & Zeng, N. (2009). Impact of wedge-shaped roofs on airflow and pollutant dispersion inside urban street canyons. *Building and Environment*, *44*(12), 2335–2347.

Hwang, R.-L., & Lin, T.-P. (2007). Thermal comfort requirements for occupants of semi-outdoor and outdoor environments in hot-humid regions. *Architectural Science Review*, *50*(4), 357–364.

Jeong, S. J., & Andrews, M. J. (2002). Application of the k–ε turbulence model to the high Reynolds number skimming flow field of an urban street canyon. *Atmospheric Environment*, *36*(7), 1137–1145.

Kastner-Klein, P., Berkowicz, R., & Britter, R. (2004). The influence of street architecture on flow and dispersion in street canyons. *Meteorology and Atmospheric Physics*, *87*(1), 121–131.

Kastner-Klein, P., Fedorovich, E., & Rotach, M. (2001). A wind tunnel study of organised and turbulent air motions in urban street canyons. *Journal of Wind Engineering and Industrial Aerodynamics*, *89*(9), 849–861.

Kastner-Klein, P., & Plate, E. (1999). Wind-tunnel study of concentration fields in street canyons. *Atmospheric Environment*, *33*(24), 3973–3979.

Kataoka, K., Matsumoto, F., Ichinose, T., & Taniguchi, M. (2009). Urban warming trends in several large Asian cities over the last 100 years. *Science of the Total Environment*, *407*(9), 3112–3119.

Koh, J. (2015). Void deck. National Library Board Singapore. Retrieved from http://eresources.nlb.gov.sg/infopedia/articles/SIP_2015-01-27_191959.html

Lau, W. K., & Kim, K.-M. (2012). The 2010 Pakistan flood and Russian heat wave: Teleconnection of hydrometeorological extremes. *Journal of Hydrometeorology*, *13*(1), 392–403.

Li, X.-X., Leung, D. Y., Liu, C.-H., & Lam, K. (2008). Physical modeling of flow field inside urban street canyons. *Journal of Applied Meteorology and Climatology*, *47*(7), 2058–2067.

Li, X.-X., Liu, C.-H., & Leung, D. Y. (2005). Development of a k–ε model for the determination of air exchange rates for street canyons. *Atmospheric Environment*, *39*(38), 7285–7296.

Li, X.-X., Liu, C.-H., & Leung, D. Y. (2008). Large-eddy simulation of flow and pollutant dispersion in high-aspect-ratio urban street canyons with wall model. *Boundary-Layer Meteorology*, *129*(2), 249–268.

Li, X.-X., Liu, C.-H., Leung, D. Y., & Lam, K. (2006). Recent progress in CFD modelling of wind field and pollutant transport in street canyons. *Atmospheric Environment*, *40*(29), 5640–5658.

Memon, R. A., Leung, D. Y. C., & Liu, C. (2008). A review on the generation, determination and mitigation of Urban Heat Island. *Journal of Environmental Sciences*, *20*(1), 120–128.

Meroney, R. N., Pavageau, M., Rafailidis, S., & Schatzmann, M. (1996). Study of line source characteristics for 2-D physical modelling of pollutant dispersion in street canyons. *Journal of Wind Engineering and Industrial Aerodynamics*, *62*(1), 37–56.

Mirzaei, P. A., & Haghighat, F. (2010). Approaches to study urban heat island–abilities and limitations. *Building and Environment*, *45*(10), 2192–2201.

Montazeri, H., & Azizian, R. (2008). Experimental study on natural ventilation performance of one-sided wind catcher. *Building and Environment*, *43*(12), 2193–2202.

NASA scientists react to 400 ppm carbon milestone. (2013, May 21). Retrieved from https://climate.nasa.gov/400ppmquotes/

Oke, T. (1987). *Boundary layer climates* (2nd edition). London and New York: Methuen.

OpenFOAM. (2017). The OpenFOAM Foundation Ltd. Retrieved from https://openfoam.org/

ParaView. (2017). Sandia Corporation, Kitware Inc. Retrieved from http://www.paraview.org/

Pfafferott, J., Herkel, S., & Jäschke, M. (2003). Design of passive cooling by night ventilation: evaluation of a parametric model and building simulation with measurements. *Energy and Buildings*, *35*(11), 1129–1143.

Rockström, J., Steffen, W., Noone, K., Persson, \AAsa, Chapin, F. S., Lambin, E. F., ... others. (2009). A safe operating space for humanity. *Nature*, *461*(7263), 472–475.

Rotach, M. (1995). Profiles of turbulence statistics in and above an urban street canyon. *Atmospheric Environment*, *29*(13), 1473–1486.

Roth, M., & Chow, W. T. (2012). A historical review and assessment of urban heat island research in Singapore. *Singapore Journal of Tropical Geography*, *33*(3), 381–397.

Saadatian, O., Haw, L. C., Sopian, K., & Sulaiman, M. Y. (2012). Review of windcatcher technologies. *Renewable and Sustainable Energy Reviews*, *16*(3), 1477–1495.

Salim, S. M., Buccolieri, R., Chan, A., & Di Sabatino, S. (2011). Numerical simulation of atmospheric pollutant dispersion in an urban street canyon: comparison between RANS and LES. *Journal of Wind Engineering and Industrial Aerodynamics*, *99*(2), 103–113.

Sini, J.-F., Anquetin, S., & Mestayer, P. G. (1996). Pollutant dispersion and thermal effects in urban street canyons. *Atmospheric Environment*, *30*(15), 2659–2677.

Spagnolo, J., & de Dear, R. (2003). A field study of thermal comfort in outdoor and semi-outdoor environments in subtropical Sydney Australia. *Building and Environment*, *38*(5), 721–738.

Stathopoulos, T., & Blocken, B. (2016). Pedestrian wind environment around tall buildings. In *Advanced Environmental Wind Engineering* (pp. 101–127). Springer.

Stewart, I. D., & Oke, T. R. (2012). Local climate zones for urban temperature studies. *Bulletin of the American Meteorological Society*, *93*(12), 1879–1900.

Tominaga, Y., & Stathopoulos, T. (2011). CFD modeling of pollution dispersion in a street canyon: Comparison between LES and RANS. *Journal of Wind Engineering and Industrial Aerodynamics*, *99*(4), 340–348.

Xiaomin, X., Zhen, H., & Jiasong, W. (2006). The impact of urban street layout on local atmospheric environment. *Building and Environment*, *41*(10), 1352–1363.

Xie, X., Huang, Z., & Wang, J. (2005). Impact of building configuration on air quality in street canyon. *Atmospheric Environment*, *39*(25), 4519–4530.

Yang, W., Wong, N. H., & Jusuf, S. K. (2013). Thermal comfort in outdoor urban spaces in Singapore. *Building and Environment*, *59*, 426–435.

Yuan, C., Ng, E., & Norford, L. K. (2014). Improving air quality in high-density cities by understanding the relationship between air pollutant dispersion and urban morphologies. *Building and Environment*, *71*, 245–258.

Yuen, B. (2011). Liveability of tall residential buildings. In *High-rise living in Asian cities* (pp. 129–147). Springer.